EXPERIMENTAL AND NUMERICAL STUDIES ON A METALLIC PULSED CAPILLARY DISCHARGE AS AN EXTREME ULTRA-VIOLET (EUV) SOURCE

CHAN LI SAN

FACULTY OF SCIENCE
UNIVERSITY OF MALAYA
KUALA LUMPUR

2016

EXPERIMENTAL AND NUMERICAL STUDIES ON A METALLIC PULSED CAPILLARY DISCHARGE AS AN EXTREME ULTRA-VIOLET (EUV) SOURCE

CHAN LI SAN

THESIS SUBMITTED IN FULFILMENT OF THE REQUIREMENTS FOR THE DEGREE OF DOCTOR OF PHILOSOPHY

FACULTY OF SCIENCE
UNIVERSITY OF MALAYA
KUALA LUMPUR

2016

ABSTRACT

A system for the generation of metallic capillary discharge plasma has been developed and studied. The quartz capillary is initially evacuated to a low pressure of 10^{-5} mbar. The transient hollow cathode discharge (THCD) generated high energy electron beam is employed to initiate the discharge by vaporizing the tip of the stainless steel anode. Due to pressure gradient, the stainless steel vapour (predominantly iron, Fe) is injected into the capillary and heated by the discharge to form the capillary plasma. This is evidenced from the time-integrated visible spectrum of the plasma which consists of mainly Fe emission lines. The stainless steel capillary plasma emits predominantly in the Extreme Ultraviolet (EUV) and Visible regions. The emissions produced by the capillary discharge at various stages of plasma formation in the capillary have been studied by varying the experimental parameters including the discharge voltage and the operating pressure. At the initiation of the discharge, X-ray is observed to be emitted prior to the start of the main discharge due to the bombardment of THCD generated electron beam on the anode and it is found that the X-ray intensity decreases with the increase of operating pressure and increases with the increase of discharge voltage. EUV is emitted mostly by the stainless steel plasma in the first half cycle of the main discharge. The EUV energy produced by the stainless steel plasma is 3.28×10^{-2} J at discharge voltage of 2.6×10^{4} V and pressure of 10^{-5} mbar. The conversion efficiency (CE) achieved is 0.45%. The effect of the ambient gas on the EUV emission of the capillary discharge has been investigated. In this case, argon gas is used and it is observed that the stainless steel plasma emits higher EUV energy at lower argon pressure. In another series of experiments, copper anode is used, and thus producing a copper capillary plasma. The EUV energy produced by the copper plasma is 3.8×10^{-2} mJ at discharge voltage of 2.7×10^{4} V and pressure of 10^{-5} mbar with CE of 0.48%. The electron temperature of the stainless steel (Fe predominant) and copper plasma are simulated by using the LCR circuit equation. The plasma electron temperature achieved for stainless steel (Fe predominant) and copper plasma are 12.6 eV and 13.8 eV respectively. The EUV spectra of both plasmas are simulated by using the FLYCHK suite of codes. It is evidenced that the Copper (Cu) plasma emit with higher intensity compared to iron (Fe) plasma at 13.5 nm. In further enhancing the EUV emission of our metallic capillary discharge, capacitors of higher capacitance with total capacitance of 1.2 μF is used to power the system. The EUV energy that can be produced with this system is 8.36 x 10^{-2} J at discharge voltage of 8 x 10^{3} V and pressure of 10^{-5} mbar with CE of only 0.22%. The plasma of this higher input energy system (total capacitance of 1.2 μF) emits with a small increase of intensity compared to the lower energy system (total capacitance of 21.6 nF) at 13.5 nm.

ABSTRAK

Dalam kajian ini, satu sistem untuk penjanaan logam kapilari nyahcas plasma telah dibangunkan dan dikaji. Kapilari kuarza pada mulanya divakumkan ke tekanan yang rendah 10-5 mbar. Fana berongga katod nyahcas (THCD) menjana elektron rasuk yang bertenaga tinggi digunakan untuk memulakan myahcas dengan mengewapkan hujung keluli tahan karat anod. Oleh kerana perbezaan tekanan, wap keluli tahan karat, yang mengandungi atau mempunyai besi (Fe), disuntik ke dalam rerambut dan dipanaskan untuk membentuk plasma rerambut. Ini terbukti daripada spektrum plasma yang diperolehi yang terdiri daripada komponen-komponen Fe. Keluli tahan karat plasma kapilari memancarkan cahaya Ultraviolet lampau (EUV) dan cahaya nampak. Pancaran yang dihasilkan oleh nyahcas kapilari di pelbagai peringkat pembentukan plasma dalam rerambut telah dikaji dengan mengubah parameter eksperimen termasuk voltan nyahcas dan tekanan operasi. Pada permulaan pelepasan, sinar-X diperhatikan akan dikeluarkan sebaik sahaja sebelum permulaan nyahcas manandakan penghentaman elektron rasuk THCD pada anod dan didapati bahawa keamatan sinar-X berkurangan dengan peningkatan tekanan operasi dan meningkat dengan peningkatan voltan nyahcas. EUV dipancarkan kebanyakannya oleh keluli tahan karat plasma dalam separuh pertama kitaran pertama nyahcas. Ia didapati bahawa tenaga EUV yang dihasilkan oleh keluli tahan karat plasma adalah 32.8 mJ pada voltan nyahcas sebanyak 26 kV dan tekanan operasi 10^{-5} mbar. Kecekapan penukaran (CE) dicapai dianggarkan 0.45%. Kesan gas ambien terhadap pancaran EUV yang dihasilkan daripada nyahcas kapilari rerambut telah disiasat. Dalam kes ini gas argon digunakan dan ia diperhatikan bahawa plasma keluli tahan karat mengeluarkan tenaga EUV lebih tinggi pada tekanan argon lebih rendah. Dalam satu lagi siri eksperimen, anod tembaga digunakan, dan dengan itu menghasilkan plasma kapilari tembaga. Tenaga EUV dihasilkan oleh plasma kapilari tembaga ialah 38 mJ pada voltan 27 kV dan tekanan operasi 10-5 mbar dengan nilai CE sebanyak 0.48%. Suhu elektron untuk plasma keluli tahan karat (Fe utama) dan plasma tembaga disimulasi dengan menggunakan persamaan LCR. Spektrum EUV keluli tahan karat (Fe utama) dan plasma tembaga disimulasi dengan menggunakan kod-kod FLYCHK. Spektrum EUV untuk Fe dan Cu diplot dan dianalisis. Ia terbukti bahawa Tembaga (Cu) plasma memancarkan dengan intensiti yang lebih tinggi berbanding dengan besi (Fe) plasma pada 13.5 nm. Dalam usaha untuk meningkatkan lagi pancaran EUV logam kapilari kami, kapasitor kemuatan yang lebih tinggi dengan jumlah kemuatan 1.2 μF digunakan untuk kuasa sistem kapilari untuk membekalkan tenaga input yang lebih tinggi untuk meningkatkan tenaga pancaran EUV. Tenaga EUV yang boleh dihasilkan dengan sistem ini adalah 83.6 mJ pada voltan pelepasan 8 kV dan operasi tekanan 10-5 dengan CE yang hanya bernilai 0.22%.

ACKNOWLEDGEMENTS

I would like to express my deepest gratitude to my supervisor, Professor Dr. Wong Chiow San for his valuable guidance, suggestions, patience, effort and assistance throughout the entire course of the project. This PhD degree will not be completed without his consistent assistance and guidance.

I would like to thank Dr. Yap Seong Ling for her advice and suggestions throughout the entire project.

I would like to acknowledge Mr. Jasbir Singh for his technical expertise, without his technical assistance, the experimental work will not be able to be carried out smoothly. I am also thankful to the workers of the workshop in Physics Department for machining some of the parts of the pulsed capillary discharge. I would like to thank Associate. Prof. Dr. Chin for her advice during my candidature.

Appreciation also goes to Daryl Tan who is my co-worker on the same system for the fruitful time of discussion, working together as well as brainstorming of ideas. Special thanks to the members of the Plasma Research Group, Siew Kien, Lian Kuang, Ming Chuan, Boon Kiat, Hun Seng, Kanesh and Yen Theng for lending their helping hand along the way. I am also grateful to all my other lecturers and friends in the Physics Department for their advices and friendship.

I would like to express my greatest appreciation to all my family members especially my mother for their love, encouragement and financial support. Finally, I want to thank my Lord Jesus, for He is the greatest Provider in my life.

TABLE OF CONTENTS

CHAPTER 1: INTRODUCTION

Pulsed capillary discharge is a compact plasma device that is capable of producing moderately hot and dense plasma. The discharge is initiated between two electrodes through a narrow capillary. The pulsed capillary discharge can be powered by capacitor discharge. The high current produced by the capacitor discharge will flow through the narrow capillary and heats up the gas particles inside the capillary to form a plasma.

There are three types of capillary discharge systems, namely ablative capillary discharge, gas-filled capillary discharge and metallic capillary discharge. In the ablative capillary discharge, the plasma is formed by heating the material ablated from the wall of the capillary, while in the gas-filled capillary discharge, the plasma is formed by heating a gas that is filled into the capillary channel. On the other hand, in the metallic capillary discharge, metallic vapor of the anode is injected into the capillary channel by focusing either a pulsed laser beam or pulsed electron beam onto the tip of the anode just before the initiation of the discharge. In this case, a plasma of the metallic material will be formed.

The moderately hot capillary plasma is capable of emitting in the soft X-ray to visible region. The emission of the capillary plasma is studied and enhanced for different purposes (Moreno *et al*., 1999; Klosner *et al*., 2001; Nevrkla, 2009; Niimi *et al*., 2001; Yap *et al*., 2006; Tan *et al*., 2007). One region of the capillary plasma emission that is widely studied is Extreme Ultraviolet (EUV), which is the possible light source that will be used to perform the Next Generation Lithography (NGL) (Klosner *et al*., 2001; Yap *et al*., 2006).

CHAPTER 2: LITERATURE REVIEW

In this chapter, some of the research that have been carried out on the ablative capillary discharge, gas-filled capillary discharge and metallic capillary discharge will be reviewed.

2.1 Pulsed Capillary Discharge based On Extreme Ultraviolet Source

Lithography is a process of transferring pattern from a mask to a photoresist deposited on a substrate. The process of transferring pattern is accomplished by using a set of exposure tool which consists of light source, mask, photoresist, and substrate. Photoresist is a radiation-sensitive compound while the substrate is referred to the silicon wafer.

Extreme Ultraviolet Lithography (EUVL) is listed on the international technology road map for semiconductors (ITRS) (Tanaka *et al*., 2004). EUVL is one of the leading candidates of the next generation lithography that is able to extend the minimum line width to 30 nm without throughput loss. EUV source of wavelength range from 10 nm to 14 nm will be used as the light source in EUVL. Plasma based EUV sources produce highly ionised atoms that emit EUV radiation. It can be based on either the laser produced plasma (LPP) or the discharge produced plasma (DPP) (Segers *et al*., 2002; Krüken *et al*, 2004; Banine *et al*., 2004; Jonkers, 2005; Wu *et al*., 2013; Wagenaars *et al,* 2008).

Several discharge light sources based of the pulsed capillary discharge with emission in the spectral band 13.5 ± 0.5 nm have been studied and reported by various research groups (Mohanty *et al*., 2003; Zhang *et al*., 2005; Borisov *et al*., 2010). The

EUV radiation generated by DPP in tin plasma with emission power of 1000 W/(2π sr) had been achieved.

Capillary discharge was initially known as sliding or guided sparks. Two decades ago, amplified spontaneous emission at soft X-ray wavelength was observed (Matthews *et al*., 1985; Suckewer *et al*., 1985). Both papers reported on the production of soft X-ray lasers by using laser produced plasma (LPP). However, this method was found to be costly and complex due to the large laser facility that was used.

Later, in 1994, large soft X-ray amplification was observed in a gas discharge produced plasma (GDP) (Rocca *et al*., 1994). In this paper, it was reported that fast electrical discharge concept was used to excite plasma columns up to 12 cm long and 4 mm diameter and produced soft X-ray laser. The plasma that was formed in this narrow channel was hot, dense and highly ionized.

The GDP concept led to the advantage of having a low cost, simple and compact system (Zhang *et al*., 2005; Mohanty *et al*., 2003). Three main types of capillary discharge namely ablative capillary discharge, gas-filled capillary discharge (Klosner *et al*., 2001) and metallic capillary discharge (Marconi *et al*., 1989; Klosner *et al*., 2000; Wyndham *et al*., 2002; Borisov *et al*., 2004 Wyndham *et al*., 2006; Shuker *et al*., 2006) are being studied. As for metallic capillary discharge, various operation techniques are developed (Marconi *et al*., 1989; Klosner *et al*, 2000; Wyndham *et al*., 2002; Wyndham *et al*., 2006; Shuker *et al*., 2006). Due to its simplicity and cost effectiveness, capillary discharge is used to generate EUV radiation which has been used as Extreme Ultraviolet lithography (EUVL) light source since about a decade ago.

Much effort has been put on the capillary discharge system in order to enhance the quality of the soft X-ray and EUV production. These include of using capillary of different materials for ablative capillary discharge (Rocca *et al*., 1993; Tomasel *et al*., 1993; Götze *et al*., 2002; Dussart *et al*., 2000; Tomasel *et al*., 1996; Andreić *et al*., 2003), filling the capillary channel with various gases for gas-filled capillary discharge (Villagran *et al*., 1990; Rocca *et al*., 1993; Niimi *et al*., 2001, Mohanty *et al*., 2003; Song *et al*., 2006; Valenzuela *et al*., 2015), and using different types of metallic vapor to fill the capillary channel for metallic capillary discharge (Rocca *et al*., 1993; Klosner *et al*., 1997; Wyndham *et al*., 2002; Janulewicz *et al*., 2003; Rahman *et al*., 2003).

2.1.1 Ablative Capillary Discharge (ablation of non-metallic material as plasma source)

Initially, the investigations of capillary discharge were done using the evacuated or ablative discharge. In the year 2000, an investigation of a micro capillary discharge was reported (Marconi *et al*., 2000). In this work, plasma was produced from material ablated from the capillary wall by the fast current pulse. The dynamics of the plasma that was generated in a 380 μm diameter and 8 mm long evacuated polyacetal micro capillary was studied by using time-resolved imaging technique. Dense regions of ablated material were observed at the capillary wall at the initial stage of the discharge. As the current increased, the ablated material was heated to form plasma and was compressed towards the axis of the evacuated channel. The electron density of the plasma formed was estimated to be of the order of 10^{19} cm^{-3} and the electron temperature achieved was 15 to 20 eV.

Another polyacetal capillary discharge was also reported later (Götze *et al*., 2002). The emission lines of the plasma was observed using time-resolved spectroscopic technique. The electron temperature achieved during the discharge was estimated to be as high as 60 eV during pinching or compression phase. The maximum electron density reached was of the order of 5×10^{19} cm^{-3}.

The research on ablative capillary discharge continues to progress. The length of the capillary were manipulated in order to observe the effect of capillary length on the time evolution of the plasma. Dussart *et al*. reported on the time-resolved imaging of the plasma column using capillaries of different lengths. Comparison between the time evolution of the plasma diameter that was formed in a 10 mm long capillary and a 16 mm long capillary was made. It was noticed that circular sheath was formed around the centre of the 10 mm long capillary. However, this feature could not be observed with the 16 mm long capillary (Dussart *et al*, 2000).

Capillaries made of different materials such as polyacetal (Marconi *et al*., 2000), polyethylene (Dussart *et al*., 2000) and PVC (Andreić *et al*., 2003; Andreić *et al*., 2005) were used in order to produce different species in the plasma so that radiation from the bands of interest can be optimized. Elements that are found in the plasma are ablated from the wall of the capillary when high current flowed through the capillary. Plasmas that were formed in the polyacetal and polyethylene capillaries had a high composition of carbon. As for PVC capillary, it depended on the additives of the PVC. PVC with Sn-based additives produced plasma with large amount of Sn while PVC with Zn-based additives produced plasma column with large amount of Zn. Besides that, the PVC with Zn-based additives was more sensitive to discharge voltage compared to the PVC with Sn-based additives. The intensity of the wavelength in the EUV region for capillary discharge with PVC with Zn-based capillary changed drastically when the discharge voltage was varied just by a few kilovolts. It was found that plasma formed using PVC capillary with Sn-based additives was able to produce a single and high intensity peak at 13.5 nm. The plasma temperature of this PVC capillary was rather cold which was around 8 to 10 eV. The electron density was in the order of 10^{18} to 10^{19} cm^{-3}.

2.1.2 Gas-filled Capillary Discharge

In 1990, Villagran *et al*. reported on a highly ionized helium capillary discharge. Emission spectroscopy was employed to study the temporal evolution of plasma density of the highly ionized helium plasma generated in a 1 mm diameter capillary at pressure of 1-3 torr. As a result, a 1.2 kA discharge current pulse created a nearly completely ionized helium capillary plasma with a density of 8×10^{16} cm^{-3} in 1 torr of helium (Villagran *et al*., 1990).

Rocca et al. reported on an argon-filled capillary discharge as soft-x-ray amplifiers in year 1993. A hot plasma column ($T_e > 150$ eV) with diameter of 20 μm was produced by a fast pulsed discharge. Soft X-ray spectra were obtained from argon plasma at the discharge current of less than 60 kA. Highly ionized plasma column was obtained due to the rapid compression (Rocca *et al*., 1993).

In the following year, the first large soft X-ray amplification with gain-length (*gl*) of 7.2 in a discharge created plasma was reported (Rocca *et al*., 1994). A 40 kA current pulse was used to excite the plasma in an argon filled capillary with dimension of 12 cm in length and 4 mm in inner diameter. The dynamics of the argon plasma column was obtained (Rocca *et al*., 1996). It was reported that the soft X-ray emitting region was rapidly compressed in 10 ns to form a column of 200-300 μm. At the time of lasing, the electron density was estimated to be about 0.3-1 x 10^{19} cm^{-3} with electron temperature of 60-90 eV. The gain-length of the laser was improved to approximately 14 cm with a plasma column length of 15 cm. (Rocca *et al*., 1995)

This was followed by the study where an external axial magnetic field was applied to the discharge created plasma (Tomasel *et al*., 1996). It was reported that the uniformity and divergence of the 46.9 nm discharge-pumped Ne-like Ar soft X-ray amplifier beam was improved by decreasing the plasma density at the time of lasing. The laser beam intensity was increased at the optimum applied magnetic field of 0.15 T. However, at higher applied magnetic field, Zeeman effect occurred thus causing the laser output to decrease.

Investigations were carried out in order to obtain intense EUV and soft X-ray radiation by several other groups. (Villagran *et al*., 1990; Rocca *et al*., 1993; Spence *et al*., 2000; Niimi *et al*., 2001; Gonzalez *et al*., 2002; Mohanty *et al*., 2003; Yap *et al*., 2006) Different gases including Ar, He and Xe were used to fill the capillary in order to enhance the radiation production. Time-integrated and time-resolved spectroscopic measurements were obtained in order to investigate the EUV radiation emanating from the xenon-filled alumina capillary. A EUV pinhole camera was employed in order to observe the dynamics of the plasma. Time-integrated spectra showed that the source was able to produce intense flux of photons at 13.5 ± 0.13 nm. The conversion efficiency achieved was 0.6%. Time-resolved measurements indicated that all broad band radiation including 13.5 nm appeared only in the first half cycle of the discharge current. There was no emission from impurities in the first half cycle of the discharge. Time-resolved pinhole images indicated that the plasma was pinched by the self-generated electromagnetic force to form a high intensity and high temperature needle-shaped plasma column (Mohanty *et al*., 2003).

The dimensions of the capillaries such as capillary length and diameter were varied in order to maximize the energy of radiation at 13.5 nm. Experiments were conducted by varying the capillary length from 10 mm to 30 mm and capillary diameter from 0.8 mm to 2 mm. The EUV emission was measured by using a AXUV-12 photodiode (IRD Inc) in combination with 1700 Å thick Zr filter with Ni mesh support at end-on position. It was determined that the capillary with 10 mm long and 1.2 mm diameter gave the strongest EUV emission (Mohanty *et al*., 2003).

A recent research on the dynamics and EUV emission of a sub-joule capillary discharge as a potential high repetitive rate radiation source was reported. It was observed that the EUV emission started from a compressed plasma on axis during the second quarter period of the current and continued until the fifth quarter period. Ionization of Ar VII to X were obtained. At the onset of the emission (~7 ns), the plasma was found to be well fitted with a single Maxwellian electron distribution function with $T_e \sim 12$ eV and $n_e \sim 10^{17}$ cm^{-3} in comparison of the EUV emission spectra with the synthetic spectra. At about the peak emission, plasma temperature increased to 20 eV and $n_e \sim 10^{20}$ cm^{-3} (Valenzuela *et al*., 2015).

2.1.3 Metallic Capillary Discharge

In a metallic capillary discharge, metallic vapor will be generated as plasma source. In the year 1989, a time-resolved EUV emission from a highly ionized lithium capillary discharge was reported (Marconi *et al*., 1989). In this research, a fast discharge current pulsed was used to produce a highly ionized plasma in a 500 µm diameter lithium hydride capillary with a length of 3.8 cm. In this system, lithium hydride (which is electrically non-conducting) was used as a capillary and lithium was ablated from the capillary wall to form the capillary plasma. The temperature achieved is estimated to be about 27 eV and the electron density is estimated to be about 10^{18} cm^{-3}. In the following year, the effect of an externally applied axial magnetic field with amplitude of 70-100 kG to the temporal evolution of the extreme ultraviolet emission was studied (Marconi *et al*., 1990). The experiment was carried out using a 500 µm diameter lithium hydride capillary with a length of 76 mm. It was reported that the external magnetic field reduced the intensity of the recombination lines by decreasing the rate of the plasma cooling due to electron heat conduction to the capillary wall. In the absence of external magnetic confinement, strong emission from ionic transitions excited by collisional recombination was observed at the end of the current pulse. However, the self-generated magnetic field of the discharge seemed to encourage the generation of the initial hot plasma, and permitted the rapid cooling due to conduction of heat to the capillary wall.

In another independent study using lithium-based capillary discharge (Klosner *et al*., 2000), an oven was used to heat the solid lithium within the anode, adjacent to the capillary. The oven also heating the capillary region and the cathode. At 185°C, the lithium melted, and the lithium liquid wetted a stainless steel mesh wick that covered the inner wall of the anode. After the wick had been wetted, a cylindrical surface of molten lithium is established in the anode region, adjacent to the capillary. The molten surface supplies lithium atoms that diffuse into the capillary region and were excited by the discharge current pulse. The EUV energy produced was 0.2 mJ /2π sr/pulse at the wavelength of 13.5 nm. The plasma electron density was below 3 x 10^{19} cm^{-3}.

In another work, a small pulsed power generator, 150 kA and 120 ns, was used to produce a titanium or aluminium plasma in a 5 mm diameter alumina ceramic capillary tube (Wyndham *et al*., 2002). In this research, a hollow cathode geometry was used and a pre-ionised plasma was formed in an initial vacuum background by focusing a pulsed Nd:YAG laser onto a metallic target (titanium or aluminium rod) in the hollow cathode region. The evolution of the pre-ionising plasma and its expansion into the main discharge volume was assisted by applying a current of the order of several amperes at a variable time before the main discharge current. Intense electron beams were observed both during the pre-ionised stage and during the start of the main current. Further work on increasing the metallic (titanium) plasma density was subsequently reported by the same group of researchers (Wyndham *et al*., 2006). In this experiment, a titanium metal ring was used to promote the formation of a titanium plasma through preferential ablation. Initially, a titanium seed plasma was formed in the hollow cathode (HC) region by a low energy laser. This pre-ionised plasma was assisted in its expansion into the main discharge region by the electron beams generated by the transient hollow cathode effect. Further intense e-beam was produced on applying the main current to the capillary electrodes before the discharge impedance dropped abruptly to give rise to an ensuing high current z-pinch. The segmented titanium ring structure within the capillary enhanced metal ablation. When the discharge occured in the ceramic capillary tube, the titanium ring was ablated to provide substantial titanium vapour in capillary plasma formation. The electron density obtained was approximately 8.2 x 10^{18} cm^{-3}.

Investigation of titanium capillary discharge plasma source for extreme ultraviolet laser had also been reported (Shuker *et al*., 2006). In this work, a technique to generate jets of pure Titanium plasma was developed. The scheme of a secondary capillary was adopted in this research. A titanium (Ti) wire was exploded in the secondary alumina capillary at 1 atm pressure to produce Ti plasma of high purity. This titanium plasma jet was injected into the main capillary to be the plasma source for capillary discharge EUV laser experiment. The electron density was calculated to be $(4\pm1.5) \times 10^{17}$ cm^{-3}.

A Cadmium (Cd) capillary discharge had also been reported (Rahman *et al*., 2003; Rahman *et al*., 2004). Cd vapour was injected into the capillary through the hollow anode electrode of the capillary discharge. The Cd vapour was produced by a metal vapor gun designed to generate Cd vapour in a room temperature environment by rapidly heating a cadmium electrode with capacitive discharge. Following its injection into the capillary channel, the Cd vapour was pre-ionised with a low current pulse preceding the fast high current pulse.

2.2 Research Objectives

In the previous section, we have seen that in the case of metallic capillary discharge, the injection of metal vapour into the capillary can be done by using a metal vapour gun (Rahman *et al*., 2003; Rahman *et al*., 2004), or by focusing a laser beam onto a metallic target in the hollow cathode region (Wyndham *et al*., 2002; Wyndham *et al*., 2006). The concept of exploding wire in a secondary capillary to form the metallic vapor to be injected into the main capillary was also introduced.

In the present research, we introduce a simple (compared to the previous reported techniques) and different technique of operating the metallic capillary discharge. A SCR triggering unit is used to create a spark in the hollow cathode region (HCR). This spark causes a tiny plasma to be formed in the HCR. The electric field produced by the high voltage pulse applied across the electrodes will extract the electrons from the HCR plasma and accelerate them to form electron beam flowing through the capillary channel and eventually bombard at the tip of the anode. The bombardment of the electron beam on the anode evaporates the anode material and this phenomenon is signified by the emission of X-ray at the initiation of the discharge. Due to pressure gradient, the anode vapour is injected into the capillary as plasma fuel. The capacitors will then discharge through the capillary and thus heat up the metallic vapour to form plasma.

The metallic plasma formed in the capillary discharge emits in the EUV and visible region. In this case, we study the EUV and visible emission of a stainless steel (Fe dominant) capillary plasma at the discharge voltage of 10 to 27 kV and operating pressure of 10^{-3} to 10^{-5} mbar. The effect of using argon ambient instead of air ambient on the EUV emission of the metallic capillary discharge will be investigated. The discharge voltage and the operating pressure are varied in order to obtain the condition for optimum EUV emission. Copper anode will also be tested to see its effect on the EUV emission characteristics of the capillary discharge.

2.3 Outline of this Thesis

This thesis is organized in the following manner:

Chapter one reviews some aspects of the research work on the capillary discharge carried out by researchers in various laboratories. It provides an overview of the research work that have been done for three types of capillary discharge, namely the ablative capillary discharge (ablation of non-metallic material as plasma source), gas-filled capillary discharge and metallic capillary discharge.

Chapter two describes the experimental setup of the capillary discharge system in detail. In this chapter, the schematic diagram of the capillary discharge is also presented. The sub-systems such as the vacuum system and the charging system are also described in detail.

In the next chapter (Chapter Three), the diagnostics techniques used for the experiments such as discharge current measurement, plasma emission characterization are described and explained. The plasma temperature estimation based on current simulation is also explained in this chapter. The code used for spectra simulation, FLYCHK is also introduced in this chapter.

In the following chapter (Chapter Four), the experimental and simulated results obtained are presented and discussed.

The final chapter which is Chapter Five gives a summary of the thesis.

CHAPTER 3: EXPERIMENTAL SETUP

3.1 An Overview of the Pulsed Capillary Discharge System (UMCD)

In a capillary discharge, plasma is formed in the narrow channel of the capillary tube that is placed between the electrodes. The pulsed capillary discharge system currently being studied at the Plasma Technology Research Centre (UMCD) is as shown in Figure 3.1.

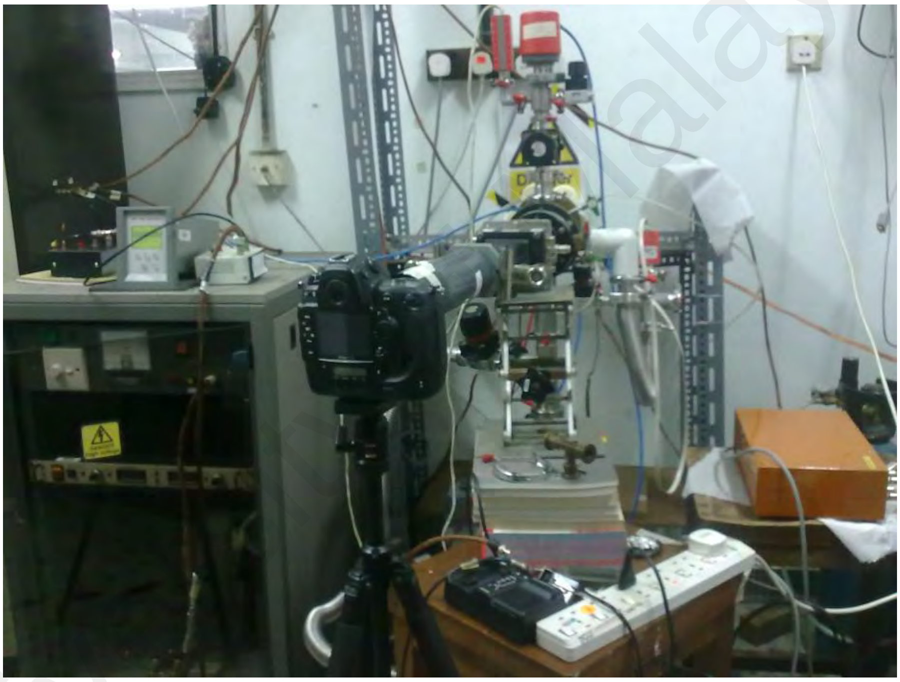

Figure 3.1: The pulsed capillary discharge system at the Plasma Technology Research Centre, University Malaya (UMCD)

The UMCD consists of several sub-systems, which are the discharge system including the capillary tube, the electrodes, the spark gap and the vacuum chamber; the vacuum and gas handling system; the capacitor charging system, the SCR triggering unit and the diagnostic tools. A schematic of the UMCD system is presented in block diagram as shown in Figure 3.2.

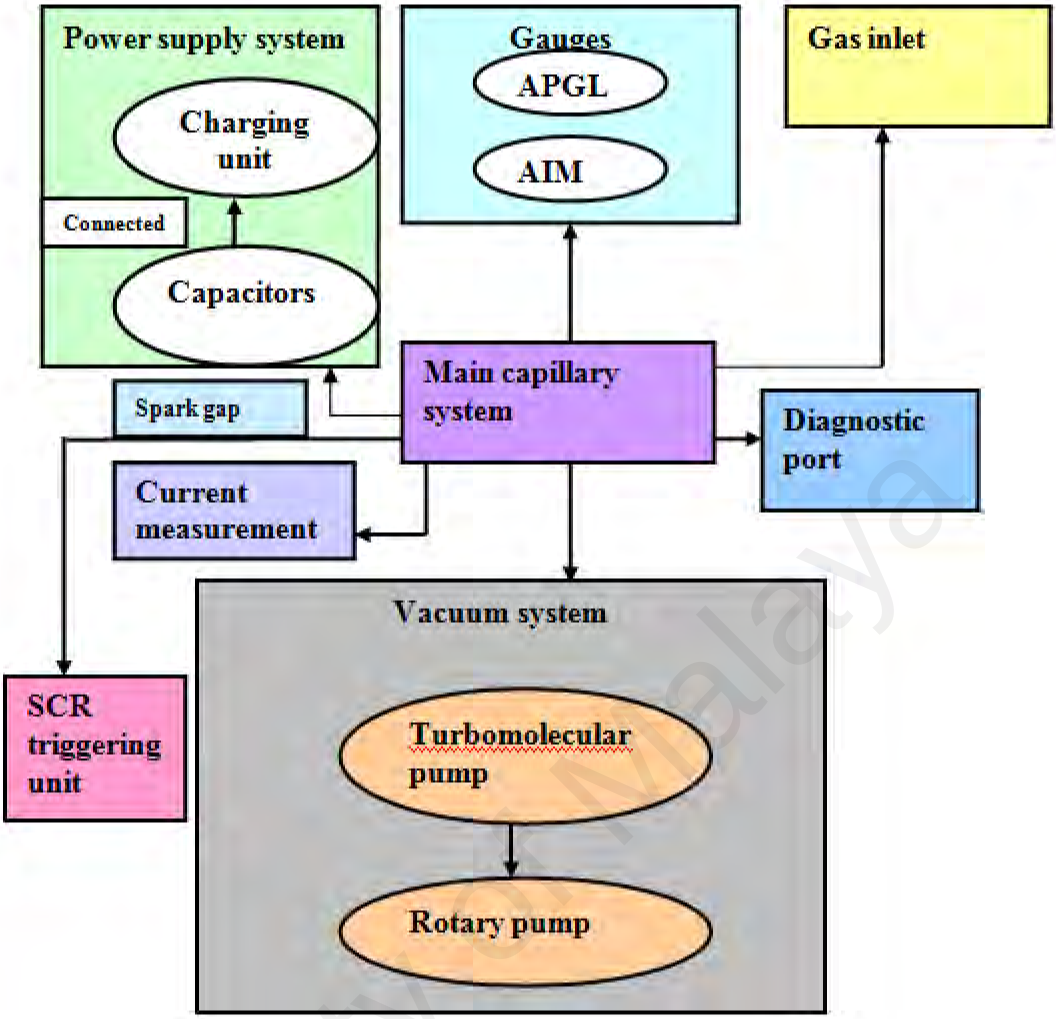

Figure 3.2: The pulsed capillary discharge system presented in block diagram

3.2 The Capacitor Charging System

The capacitor charging system of the UMCD consists of a Glassman high voltage charger and a set of doorknob capacitors. The high voltage charger is able to provide a maximum voltage of 40 kV and it is used to charge the six doorknob capacitors connected in parallel. The total capacitance of the capacitor bank is 21.6 nF.

Figure 3.3: High voltage charger

3.3 The Triggering Unit

The triggering unit consists of a silicone-controlled rectifiers (SCR) based pulse generator. The SCR functions as a switch to switch the capacitance-resistance (CR) circuit to generate the voltage pulse to initiate the discharge of the main capacitor bank. When the triggering button is pressed, a voltage is applied across the gate and cathode of the SCR. A gate current is generated and the SCR becomes conductive. In order to achieve high voltage that is needed to initiate the discharge, a high voltage transformer is used to multiply the voltage to give a negative output voltage with amplitude of 40 kV. This voltage pulse is applied to a trigger pin of the capillary discharge system.

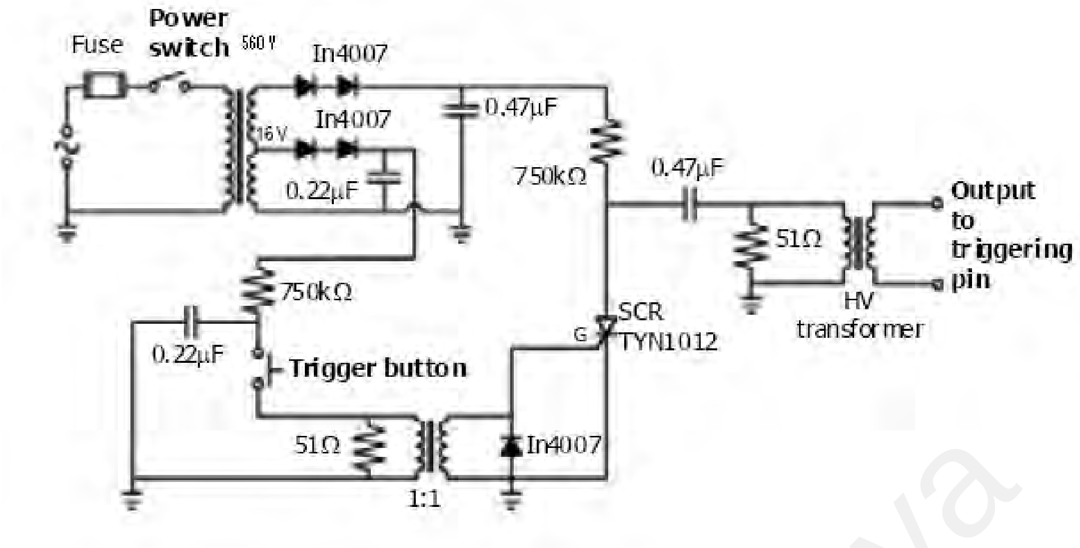

Figure 3.4: Schematic circuit of the triggering unit

3.4 The Vacuum System

The pulsed capillary discharge chamber is evacuated to a pressure of 10^{-5} mbar by a turbomolecular pump backed by a rotary pump. The pumping rate of the system is controlled by adjusting the valve so that the desired working pressure can be achieved.

A Pirani gauge and an Inverted Magnetron gauge are used to measure the pressure in the pulsed capillary discharge system. The working pressure range of the Pirani gauge is 10^{-3} mbar to 10^{3} mbar. When the pressure of the pulsed capillary discharge chamber reaches a pressure lower than 10^{-3} mbar, the Inverted Magnetron gauge will be used to measure the pressure. The Inverted Magnetron gauge can be used to measure pressure range of 10^{-8} mbar to 10^{-2} mbar.

3.5 The Gas Inlet

Argon gas is flown from the gas tank into the capillary through a gas regulator. The flow rate of the argon gas from the gas regulator into the system is controlled by a mass flow controller (model: GFC-2104) and the flow rate is displayed on the LCD readout.

The mass flow controller is switched on to warm-up for duration of 15 minutes before use. After warm-up, the reading on the LCD display is checked and it should be about zero. If not, the ZERO potentiometer is adjusted. After that, the valve off control button is switched on. Then, the flow system is purged by switching on the purge button. The reading on the LCD readout will keep on fluctuating when the purge button remains on. The purge button is switched off when the LCD readout becomes zero again. Then, the operating gas is flown through the mass flow controller into the system. The desired flow rate is obtained by adjusting the local set point potentiometer.

3.6 The Spark Gap

In the present system, the capacitors are connected to the anode through a spark gap. The spark gap is operated at atmospheric pressure. The gap of this air-filled spark gap is adjustable. The spark gap is used to hold the voltage of the capacitors before the pulsed capillary discharge system is triggered.

3.7 The Main Capillary System

3.7.1 The Anode

The capillary system consists of a bullet-shaped anode with rounded head. The anode has a length of 18 mm. The diameter of the threaded end of the anode is 10 mm. The rounded end of the anode has a hemispherical shape with radius of 5 mm. The material of the anode can be changed according to the type of plasma desired to be formed in the capillary. The flat end of the anode is threaded and is screwed into a brass holder. The rounded end is facing one end of the capillary.

3.7.2 The Capillary

The capillary used is made of a hollow quartz tube. It has an inner diameter of 1 mm and a length of 10 mm. The capillary is mounted onto the axis of a cylindrical Teflon holder by using silicon glue. The Teflon holder is used to hold the capillary when it is sandwiched in between the anode and cathode. The capillary is either evacuated in order to produce metallic plasma of the anode material or filled with gas in order to produce gas plasma.

3.7.3 The Hollow Cathode

The hollow cathode is a stainless steel circular disc with a circular aperture at the middle of the disc. A triggering pin that is used to initiate the discharge is attached to the hollow cathode and is located at the edge of the aperture. The stainless steel circular disc has a thickness of 11 mm and the diameter of the aperture is 5 mm. The aperture allows the penetration of the electric field from the high voltage anode into the hollow cathode region (HCR). This field configuration will extract electrons from the hollow cathode region to form electron beam which will be accelerated to flow through the capillary channel and will subsequently bombard at the anode tip.

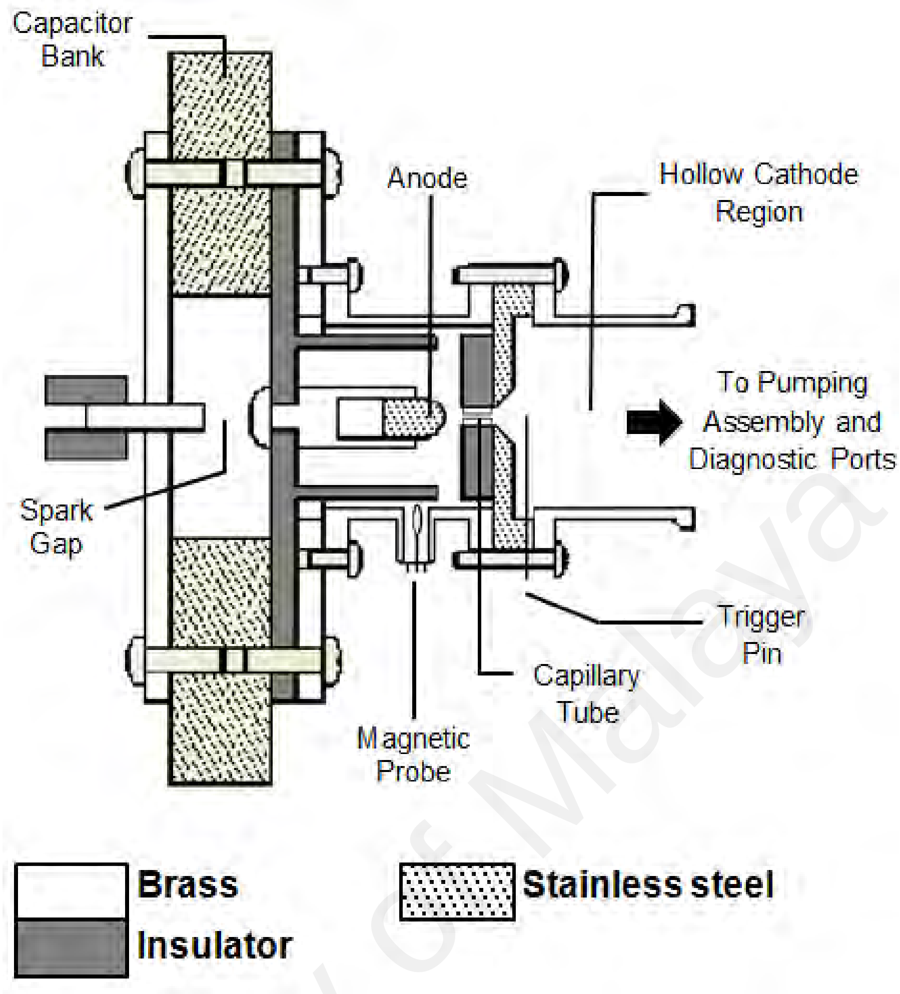

Figure 3.5: Schematic diagram of the pulsed capillary discharge.

3.8 Operation Procedure of the Pulsed Capillary Discharge

The pulsed capillary discharge system used in this project can be operated in either the metallic discharge mode or the hybrid metallic gas-filled discharge mode as described in the following sections.

3.8.1 Metallic Capillary Discharge

As the voltage is sent to the triggering pin, a low energy spark is generated between the triggering pin and the hollow cathode. This spark will result in the formation of hollow cathode region (HCR) plasma prior to the main discharge. The capacitors are charged up to the desired voltage (maximum 26 kV) and applied across the electrodes upon trigger, giving rise to a high electric field that will penetrate through the aperture of the cathode into the hollow cathode region. This electric field will extract the electrons from the HCR. The extracted electrons will be accelerated along the capillary channel and eventually bombard at the tip of the floating anode and causes the capacitors to start to discharge through the capillary channel. The anode tip is evaporated due to the electron beam bombardment and the vapor of the anode material will be injected into the capillary due to diffusion process (as the vacuum pump is located at the other side of the capillary tube) and fill up the capillary channel. The material of the anode will be heated by the high discharge current to form the capillary plasma.

3.8.2 Hybrid Metallic Gas-filled Capillary Discharge

In this case the capillary discharge system is evacuated to 10^{-5} mbar by using the turbomolecular pump backed up by the rotary pump. Argon gas is flown into the system continuously throughout the experiment in order to study an argon capillary discharge plasma. The desired operating pressure is achieved by adjusting the pumping rate. This is done by adjusting the valve that is placed between the main capillary system and the turbomolecular pump. The charging unit and triggering unit are switched on. The six capacitors that are used to power the system are charged up to the desired operating voltage. The SCR triggering unit is used to initiate the discharge. Once the triggering button is pressed, the process of transient hollow cathode electron beam will occur, similar to the case of metallic plasma discharge described in Section 3.8.1. The injection of the metallic vapor of the anode material into the capillary channel gives rise to an ambient of gas and metallic vapor mixture so the subsequent plasma formed consists of both the gaseous specie and the metallic specie.

CHAPTER 4: DIAGNOSTIC TECHNIQUES

In this research, various diagnostic techniques are being used to study the capillary plasma that is formed during the capillary discharge. A magnetic probe is used to measure the discharge current carried by the plasma. A X-ray PIN diode is used to detect the X-ray emitted by the anode tip due to the bombardment of the transient hollow cathode electron beam prior to the initiation of the discharge. A EUV photodiode is used to detect the EUV emission of the plasma during the first half cycle of the discharge. An optical spectrometer is used to obtain the visible spectrum of the plasma in order to identify and confirm the ionic species present in the plasma formed. The plasma electron temperature is estimated by a simulation of the discharge current waveform based on the resistive LCR circuit model and finally, the EUV spectrum of the plasma is predicted based on numerical simulation using the FLYCHK codes (Chung *et al*., 2005).

4.1 The Magnetic Probe

A simple magnetic probe can be constructed by making several turns of copper wire loops to act as a magnetic pickup coil. The discharge current, $I(t)$ that flows through the plasma induces a magnetic field, $B(t)$ that will be picked up by the magnetic probe. The magnetic field will cut through the cross sectional area, A, of the magnetic probe perpendicularly and induces a voltage across the coil's terminals. The magnetic probe is connected to a BNC connector in order to measure the voltage across the magnetic probe. According to Faraday's law, the voltage induced across the magnetic probe is proportional to the rate of change of the magnetic flux treading the coil.

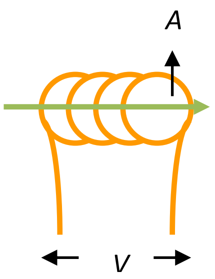

Figure 4.1: Schematic diagram of the magnetic pick-up coil.

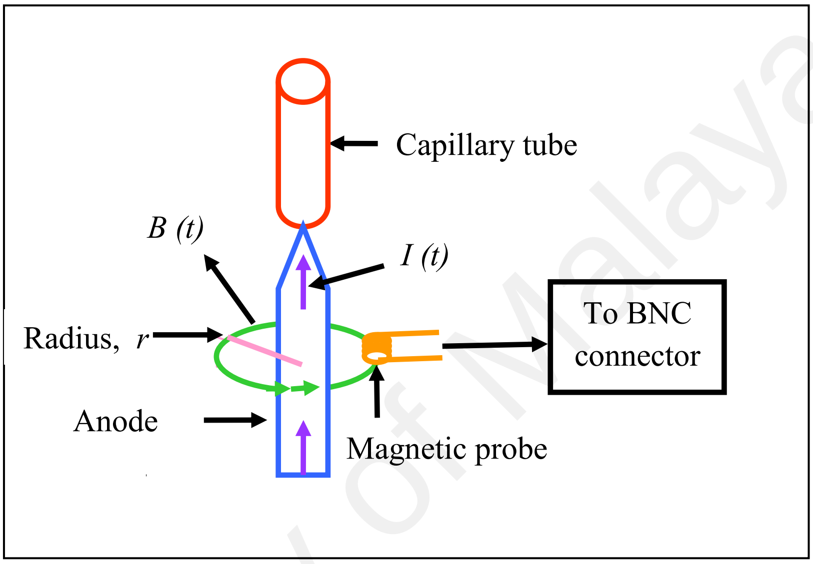

Figure 4.2: Location of magnetic probe in the capillary discharge system.

The Faraday's law can be expressed in mathematical form as:

$$V = d\phi/dt = d(\int B.ds)/dt$$

Based on Ampere's law, $B = \mu_o nI/(2\pi r)$

Thus, the output voltage of the magnetic probe is:

$$V_o = [\mu_o nA/(2\pi r)][dI/dt],$$

which is proportional to the rate of change of the discharge current.

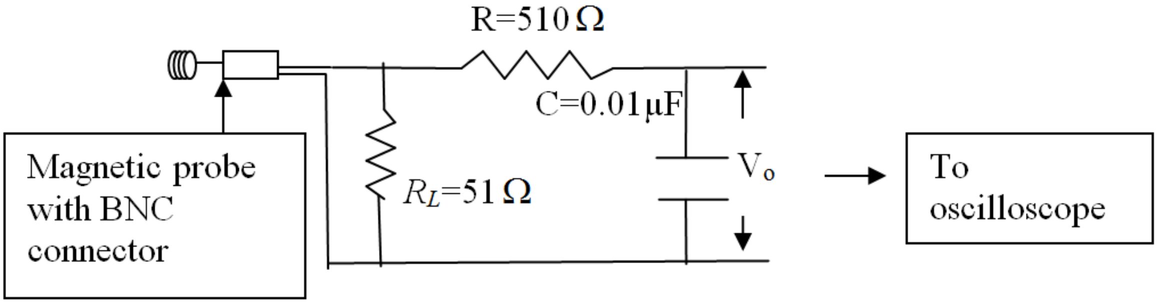

Figure 4.3: Schematic diagram of the magnetic probe circuit.

A *RC* integrator is connected between the magnetic probe and oscilloscope via a coaxial cable in order to obtain the current signal instead of the rate of change of current. The resistor, R_L is used to terminate the coaxial cable that connects the magnetic probe to the *RC* integrator. The equivalent circuit of the magnetic probe coupled to the *RC* integrator is shown schematically in Figure 4.3.

The circuit equation can be written as:

$$V = iR + L\,di/dt + \left(\int_0^{\tau} i\,dt\right)(1/C),$$

where τ is the characteristic of the circuit. τ can be taken to be of the same order of the periodic time of the discharge current which is 227 ns in this case.

For $R >> \omega L$ and $RC >> \tau$,

$$i \approx \mu_o nA[dI(t)/dt]/(2\pi rR).$$

The output voltage, V_o is hence given by

$$V_o = \left(\int_0^{\tau} i\,dt\right)(1/\mathrm{C}) = \mu_o nAI(t)/(2\pi RC) ,$$

where i = current flows through the magnetic probe,

n = number of turns of the magnetic probe.

Hence the voltage across the capacitor, V_o is proportional to the discharge current, $I(t)$.

4.1.1 Calibration of Magnetic Probe

The geometrical parameters of the magnetic probe are needed in order to calculate the discharge current based on the output voltage V_o obtained. However, it is difficult to measure these parameters of the magnetic probe accurately. Thus, the magnetic probe is calibrated and a calibration factor, K is obtained by using the in-situ method.

In order to calibrate the magnetic probe for discharge current measurement, the capillary discharge was operated at a high pressure, where the plasma is expected to have fixed resistance and inductance. Thus the discharge current waveform obtained will resemble that of a fixed LCR discharge.

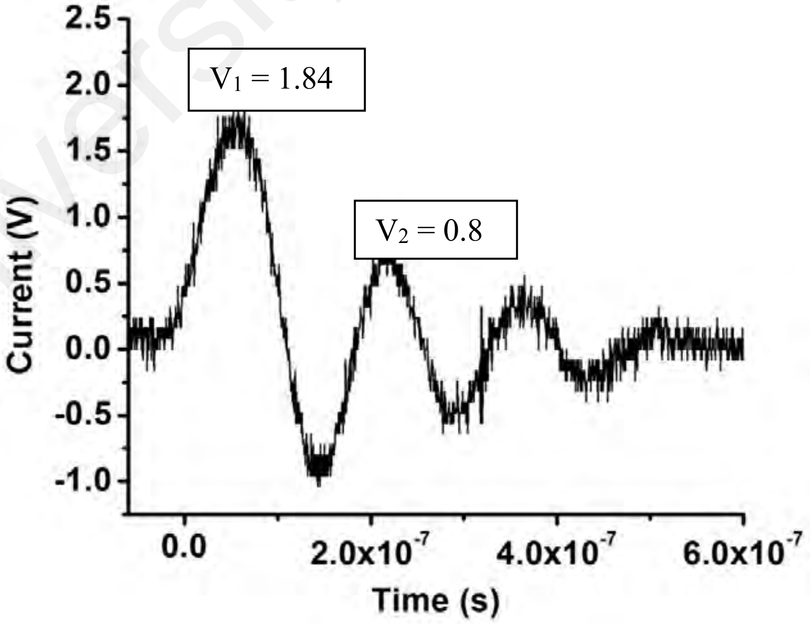

Figure 4.4: Typical current signal at the discharge voltage of 8 kV and operating pressure of 10^{-3} mbar.

Figure 4.4 shows an under-damped current waveform obtained for the purpose of obtaining the calibration factor, K.

The equation for an under-damped sinusoidal current waveform can be written as:

$$I_n = I_o e^{-\alpha t} \sin \omega t$$

where t = time of the discharge current, $I_o = V_o C_o \omega$ is the short circuit peak current delivered by discharging a capacitor C_o at discharge voltage V_o, while

$$\omega = 2\pi/T$$

where T = period of the discharge current.

Considering the first current peak at $t = T/4$ and the second peak at $t = 5T/4$

$$I_1 = I_o\, e^{-T/4}$$

$$I_2 = I_o\, e^{-5T/4}$$

Thus,

$$\alpha = -ln(V_n/V_{n+1})\ (1/T)$$

The calibration factor, K

$$K = [2\pi V_o C_o/(TV_1)]\,(V_2/V_1)^{1/4}$$

$$K = I_n/V_n$$

For the present setup, the calibration of the magnetic probe, K is calculated to be 2.396 x 10^3 A/V. The stray inductance is computed to be 46.9 nH.

3.2 PIN Diode as X-ray Detector

The X-ray detector used in this experiment consists of a silicon PIN diode (Quantrad model 100-PIN-250) coupled with 24 µm aluminized Mylar. The silicon PIN diode used in this project is made up of a silicon layer sandwiched between a layer of n type and a layer of p type silicon semiconductor. The n-layer which is also known as the dead layer is grounded and is utilized as the entrance window of the diode. The p-layer is biased at a negative potential of -300 V by using a biasing circuit as portrayed in Figure 4.5. The diode is reversed biased so that the intrinsic layer becomes completely depleted. The X-ray detector has response wavelength range of 0.03 nm to 3 nm and is placed at the end on diagnostic port of the capillary to detect the X-ray emission that occurs due to electron beam bombardment at the tip of the anode.

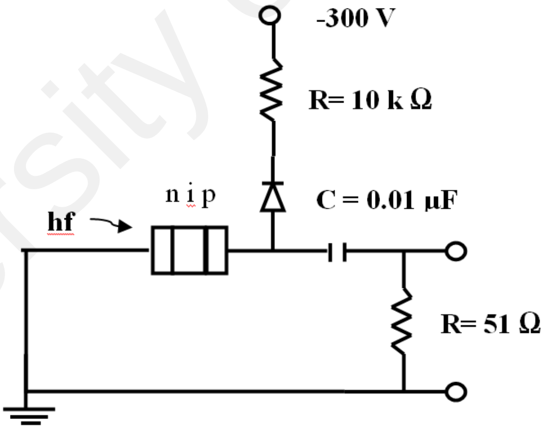

Figure 4.5: The negative biasing circuit for PIN diode.

When X-ray photons penetrate the dead layer of the PIN diode and are absorbed by the intrinsic level, electrons are liberated. At room temperature, the work function of the intrinsic layer of the PIN diode is w = 3.55 eV, thus 0.282 coulombs of electronic charge is expected to be generated for every joule of X-ray energy absorbed in the intrinsic layer (Hayward 1965).

Table 4.1: The Quantrad model 100-PIN-250 silicon PIN diode specifications

Thickness of Si entrance Window	0.8 µm
Depletion depth of intrinsic layer	250 µm at reverse biased voltage of -300 V
Effective area of detection	100 mm^2
Saturation output current	2 A
Rise time	2 ns (factory tested)

The sensitivity of the X-ray detector can be calculated using the two thickness model which is represented by the equation (Corallo et al, 1982):

$$S(\lambda) = 0.282\, e^{-x1}\, [1-e^{-\mu\, x2}] \quad \mathrm{A/W}$$

where µ is the mass absorption coefficient of silicon which is a function of X-ray photon energy, *x1* is the mass thickness of the n-type entrance window and *x2* is the effective depletion region of the intrinsic layer. Figure 4.6 shows the calculated sensitivity curve for 100-PIN-250 silicon PIN diode (Wong 1982). The K-absorption edge of silicon is shown by the singularity at about 6.7Å.

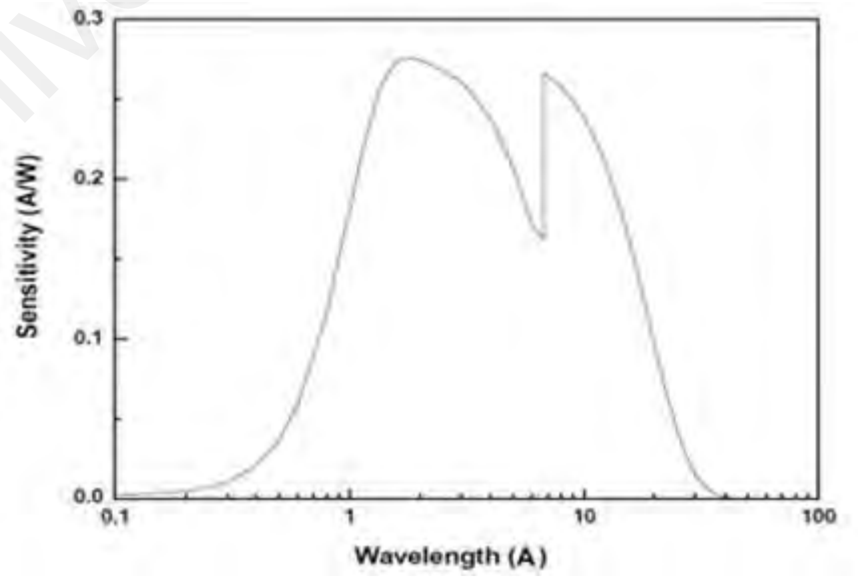

Figure 4.6: The calculated sensitivity of the PIN diode

The 24 μm aluminized Mylar acts as the filter to eliminate the ultraviolet (UV) and visible light that emit simultaneously with the X-ray. The foil consists of very thin layer of aluminium coated on thin mylar sheet The aluminium coating is used to cut off the UV and visible light. The aluminium coating is very thin (100 nm) compared to the mylar sheet and thus, the thickness of the aluminium coating is negligible in determining the mass absorption coefficient of aluminized Mylar. The mass absorption coefficient of Mylar is shown in Figure 4.7

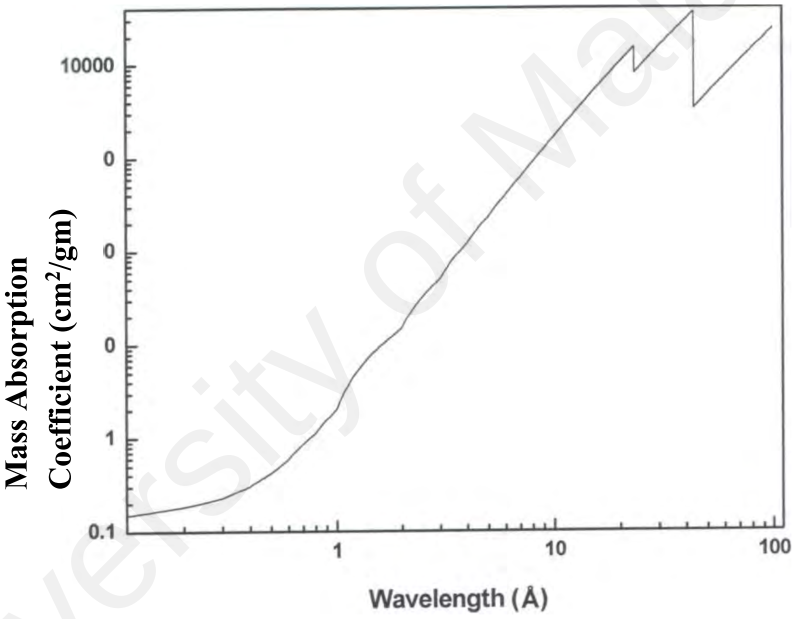

Figure 4.7: The mass absorption coefficient of mylar as a function of wavelength

When X-ray of wavelength, λ transmits through an absorption foil of thickness, x cm, with X-ray absorption coefficient, μ (λ) in cm^{-1}, the monochromatic absolute transmission is given by

$$T\,(x,\,\lambda) = I(x,\lambda)/I_o = e^{-\mu(\lambda)x}$$

where I (x,λ) is the intensity after the transmission and I_o is the initial intensity. It is shown in Figure 4.8 that the transmitted intensity decreases exponentially with initial intensity as a function of thickness and absorption coefficient of the thin foil.

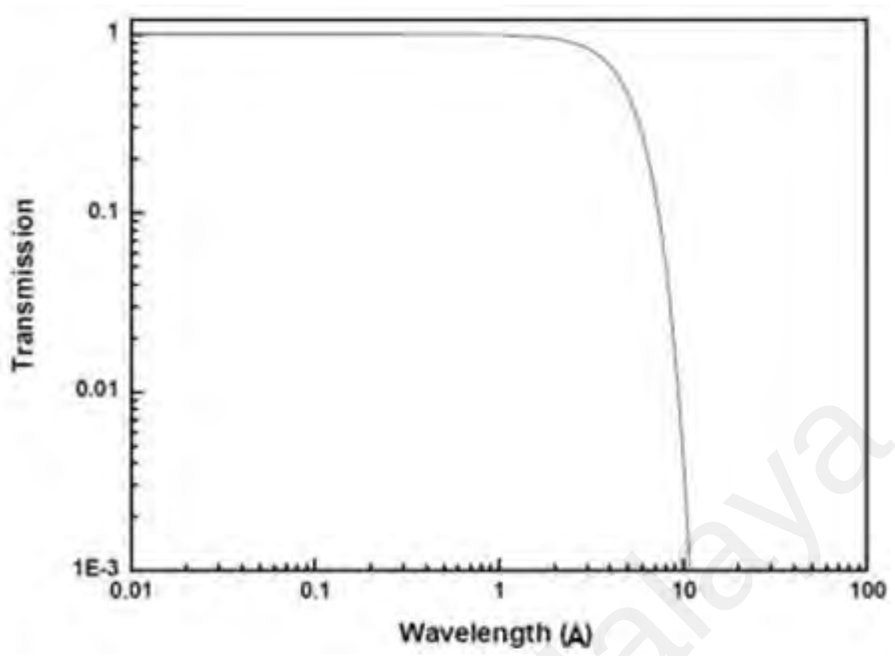

Figure 4.8: The transmission curve of 24 µm thick aluminized Mylar film.

4.3 EUV detector

The EUV detector used in this project is SXUVHS5 Si/Zr 100/200 nm photodiode from IRD (International Radiation Detectors). It is a high speed photodiode and equiped with Si/Zr filter with thickness of 100/200 nm. The SXUV photodiode can respond to photon in the wavelength range of 11-18 nm (Saboohi *et al*., 2012). The peak sensitivity of the SXUVHS5 Si/Zr 100/200 nm photodiode is at the wavelength of 13.5 nm as shown in Figure 4.9. The photodiode has a fast rise time of 700 ps. The SXUVHS5 Si/Zr 100/200 nm photodiode has an area of detection of 1 mm^2. This photodiode is biased at -45 V and is placed at the end on position of the capillary discharge system.

When SXUVHS5 Si/Zr 100/200 nm photodiode is exposed to plasma emission, the photons that are mostly in the range of wavelength of 11-18 nm will be transmitted through the Si/Zr filter and generate electron-hole pairs in the photodiode. These photogenerated carriers are separated by the p-n junction electric field and a current proportional to the numbers of generated electron-hole pairs is produced. This current will flow through an external circuit and the corresponding signal is recorded using the oscilloscope. The signal obtained is used to estimate the EUV energy emitted from the plasma based on the equation below:

$$E_{EUV} = \int V(t)\, dt\, [2\pi d^2]/(RSA)$$

where $\int V(t)dt$ is the area under the EUV photodiode signal $V(t)$, d is the distance between the source and the detector, R is a 51 Ω resistor, S is the sensitivity in C/J of the diode and A is the effective detection area of the photodiode.

The conversion efficiency, CE is generally defined as the ratio of EUV energy obtained to the input energy as shown in the equation below:

$$\text{CE} = E_{EUV}/E_{Input} \ x\ 100\%$$

The conversion efficiency of the EUV is calculated for different experimental conditions and are compared.

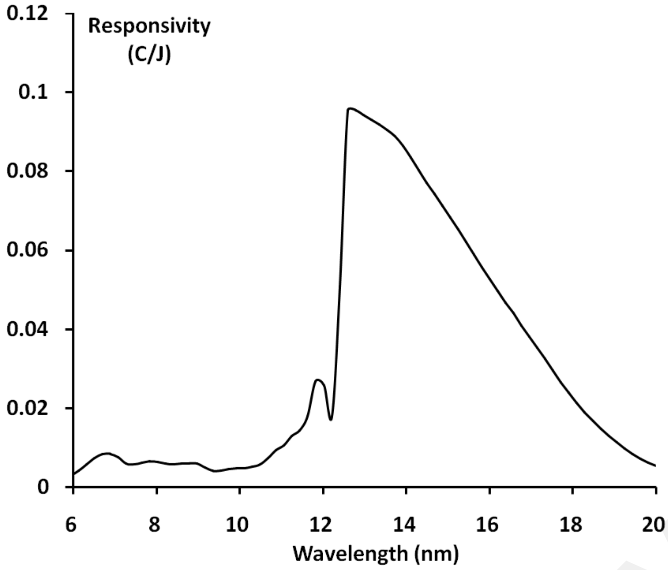

Figure 4.9: Response sensitivity curve of SXUVHS5 Si/Zr 100/200 nm.

3.4 Optical Emission Spectrometer

A HR 4000 optical spectrometer (Ocean Optics) is employed to obtain the visible spectrum of the plasma. The HR4000 spectrometer is responsive to the range of wavelength of 200-1100 nm and it is able to record up to 250 spectra per second. The signal to noise ratio of this spectrometer is 300:1. It has an optical resolution of 0.02-8.4 nm. The spectrometer is equipped with a Toshiba TCD 1304AP CCD with 3648 pixels to record the spectral image.

The HR4000 spectrometer is coupled to a single-strand fibre optic through a SMA 095 connector. The aperture size of the fibre optic is 0.22. The fibre optic is used to collect the emission from the plasma. The optical arrangement of the HR4000 spectrometer is illustrated in Figure 4.10.

1: SMA 905 connector

2: Entrance slit

3: Longpass absorbing filter

4: Collimating mirror

5. Grating

6: Focusing mirror

7: Detector collection lenses

8: Detector

9: Longpass sorting filter

10: Detector upgrades

Figure 4.10: The transverse of light in the HCR 4000 visible spectrometer (Ocean Optics) (http://oceanoptics.com/product-details/hr-optical-bench-options/).

4.5 LCR Discharge

In order to produce hot and dense plasma, a power source that is capable of delivering high current to the plasma device is required. This can be achieved by discharging high voltage capacitor with high capacity. After the capacitor with capacitance C is charged up to a high voltage V, an amount of energy of $CV^2/2$ is stored in the capacitor. The capacitor will discharge through the capillary upon triggering the switch.

The capillary discharge system can be represented schematically by the LCR circuit as shown in Figure 4.11.

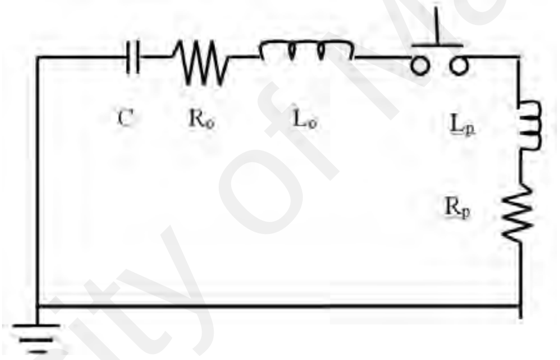

Figure 4.11: Schematic LCR discharge circuit.

In this circuit, the plasma is represented by a time-varying inductance, $L_p(t)$ and a resistance, $R_p(t)$ in series. L_o and R_o are the stray inductance and resistance of the circuit respectively. Stray inductance and resistance may be contributed by the cables used to connect the various components together as well as contributed by the switch. The capacitor or a bank of capacitors used also has an internal inductance. All these have been lumped together and represented by L_o and R_o. The circuit represents a typical LCR circuit of which the circuit equation can be written as:

$$V = IR + L(dI/dt) + \int (I/C)dt$$

where $L = L_o + L_p$ and $R = R_o + R_p$

$$V = I(R_o+R_p) + d[I(L_o + L_p)]/dt + \int (I/C)dt$$

For the capillary discharge studied in this project, we consider the plasma to be resistive and the plasma inductance is considered to be constant (further explanation regarding this consideration is discussed in section 5.5). Hence,

$$V = I(R_o + R_p) + d(LI)/dt + \int (I/C)dt$$

This equation will be normalised and will be written in the terms of normalised current, ι where $\iota = I/I_o$, normalised time, τ where $\tau = t/t_o$ where $t_o = (LC)^{1/2}$ is the characteristics time and $I_o = V_o(C/L)^{1/2}$.

Thus, the normalised form of the equation:

$$d\iota/d\tau + \alpha\iota + \int\iota d\tau = 1$$

where α is the damping factor. Since the plasma of our capillary discharge is resistive, thus,

$\alpha = R(C/L)^{1/2}$. In order to obtain the plasma resistance, we obtain the values of α by fitting the current signal that is obtained using the normalised equation with the current signal that is obtained experimentally as shown in section 5.5.1.

4.6 Plasma Temperature Estimation

In the section 4.5, we have shown that the plasma resistance, R is obtained by obtaining the damping factor, α through current fitting. The resistivity of the plasma is given by:

$$\eta = RA/l$$

where A = cross section area of the plasma which is the cross sectional area of the 1 mm diameter cylindrical channel. l = length of the plasma which is the length of the quartz capillary tube.

Thus, by obtaining the resistivity of the plasma, η the electron temperature of the plasma, T_e can be calculated based on the Spitzer's resistance formulae (Ashkenazy *et al*, 1991) which is given by:

$$T_e = [\pi e^2 m^{1/2} \ln\Lambda]^{2/3}/k\ [1/[(4\pi\varepsilon_o)^2 \eta]]^{2/3}$$

Where, $K = 1.38 \times 10^{-23}$ (Boltzman constant)

$e = 1.602 \times 10^{-19}$ (electron charge)

$m = 9.109 \times 10^{-31}$ (mass of electron)

$\ln\Lambda = 2$ (Coulomb logarithm)

$\varepsilon_o = 8.85 \times 10^{-12}$ (permissivity in free space)

4.7 FLYCHK Suite of Codes

FLYCHK is a straightforward, rapid tool to provide ionization and population distributions of plasmas in zero dimension with sufficient accuracy for most initial estimation. FLYCHK solves the rate equations for level population distributions by considering collisional and radiative atomic processes. This code is straightforward to be used and is general enough to be applied in most of the laboratory plasmas. It can be applied for low-to-high Z ions and under various plasma conditions: coronal, LTE or collisional-radiative, steady state or time dependent conditions, collisional driven or radiation driven, Maxwellian or non-Maxwellian electron distributions, optically thin or thick, and with single or mixture species (Chung *et al*., 2005).

The FLYCHK suite of codes employs schematic atomic structure and process for population distributions. The built-in atomic sets are included for all ionization stages of atoms up to Z = 93. Detailed population distributions are obtained by the solution of the rate equations considering collisional and radiative process.

A population kinetics model incorporates the results of atomic structure codes and scattering theories, plasma and statistical physics to describe atomic processes in atoms embedded in the plasma. The goal is to determine ionisation and level population distributions of a plasma for a given electron plasma temperature, T_e and electron density, N_e, and then assist in the further analysis and prediction of spectroscopic results. The elements of the population kinetics model implemented in FLYCHK are energy levels, radiative process, collisional process, auto ionisation and capture electron, and plasma effects (Chung *et al*., 2005).

FLYCHK employs the *jj* configuration averaged atomic states and oscillator strengths calculated using the Dirac-Hartee-Slater model for spectral analysis. FLYCHK is able to generate spectra that are originated by three types of transitions, namely the bound-bound, bound-free and free-free transitions.

In our research, we use FLYCHK code to generate the ion populations and EUV spectra for iron (Fe) plasma and copper (Cu) plasma and then comparison is made between the emission properties of the iron (Fe) and copper (Cu) plasmas. Capillary plasma in general has an electron density of 10^{16}-10^{20} cm^{-3} (Tomasel *et al*, 1993; Moreno *et al*., 1999; Wyndham *et al*., 2002; Shuker *et al*., 2006; Klosner *et al*., 2000; Oh *et al*., 2010; Valenzuela *et al*., 2015). In our capillary discharge system, we has estimated the electron density to be of the order of 10^{17} cm^{-3}. This estimation is done based on what is reported in (Shuker *et al*., 2006) as they have a metallic capillary discharge that has an operation technique that is similar to our system, which is based on injection of metallic vapour.

CHAPTER 5: RESULTS AND DISCUSSION

In this chapter, the discussions on the results obtained in this project will be divided into six sections:

a) The operation principle of pre-breakdown electron beam generation by the transient hollow cathode effect and its utilization to initiate the capillary discharge.

b) Comprehensive study on the emission properties of Metallic (stainless steel) capillary plasma. The emission of X-ray associated with the pre-breakdown phase, EUV emission during the first cycle of the discharge and visible light emission throughout the discharge are investigated for discharge voltage in the range of 8 to 26 kV and operating pressure in the range of 10^{-3}-10^{-5} mbar in air.

c) The effect of adding argon gas into the air ambient on EUV emission of the capillary discharge has been investigated. As a result, a stainless steel-argon capillary plasma is formed. The effect of using copper as anode material instead of stainless steel has also been investigated.

e) The estimation of plasma electron temperature by discharge current simulation.

f) Simulation of the EUV spectra of the iron (Fe) and copper (Cu) capillary plasma by using the FLYCHK code.

5.1 The Principle of Operation of the Electron Beam initiated Capillary discharge

In this work, a simple triggering system is used to initiate the metallic capillary discharge (Chan *et al.*, 2014). The vacuum chamber of the capillary discharge system is initially evacuated to 10^{-5} mbar. When the capacitor bank is charged up to the required voltage, the voltage is initially held across the main discharge electrodes and the spark gap. Upon applying the voltage pulse generated by the SCR triggering unit between the triggering pin and the stainless steel cathode plate, a spark occurs and a weakly ionised plasma is formed in the hollow cathode region (HCR). The formation of the hollow cathode plasma is indicated by the low visible light emission as detected by BPX 65 PIN photodiode (the range of wavelength of detection of BPX 65 PIN photodiode is 400-1100 nm) at around 200 ns before the main discharge (Figure 5.1).

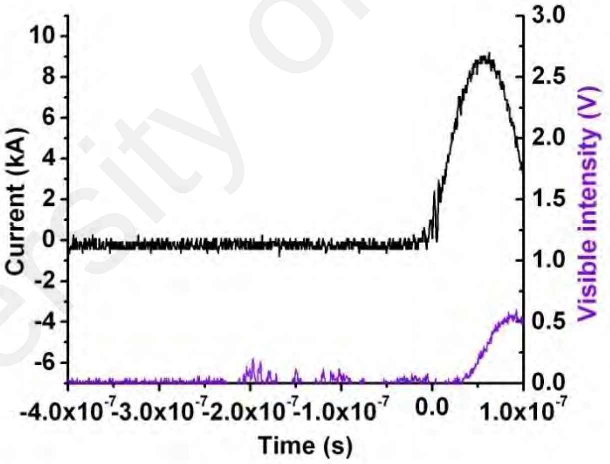

Figure 5.1: Low level visible light emission at the HCR.

The free electrons of the HC plasma are extracted due to the electric field penetration through the cathode aperture into the HCR and eventually leading to the formation of electron beam (Choi *et al.*, 1995; Favre *et al.*, 1995; Avaria *et al.*, 2009; Valdivia *et al.*, 2015). The electron beam with an estimated potential energy of equal to potential difference between the electrodes is then accelerated to pass through the capillary channel and eventually bombard at the tip of the anode (stainless steel). The bombardment of the electron beam on the anode tip evaporated the anode material and this phenomenon is signified by the X-ray pulse and sharp rise in the current signal (due to electron beam current detected by the magnetic probe) that are observed simultaneously just before the initiation of the discharge as depicted in Figure 5.2. It is also noticed that there is no prominent EUV or visible emission emitted during the occurrence of the sharp X-ray spike. This indicates that the discharge is caused by high energy electron beam which is in the range of keV.

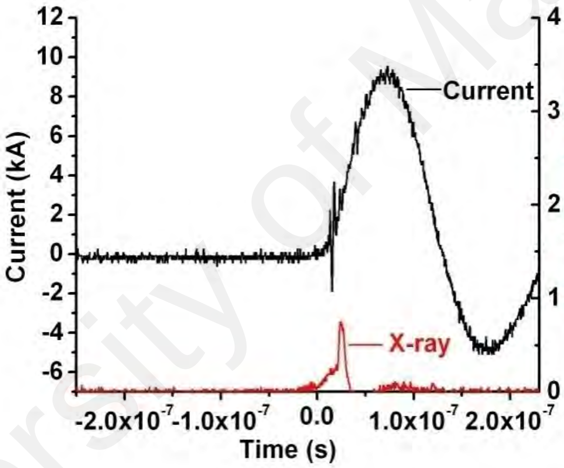

Figure 5.2: Typical current signal and X-ray emission at discharge voltage of 24 kV and pressure of 10^{-5} mbar.

Due to pressure gradient, the jet of the evaporated anode material is injected into the capillary channel which is subsequently heated to form the plasma during the main discharge. The constituents of the plasma are revealed from the time-integrated visible spectrum (Figure 5.3) of the capillary plasma obtained. The spectrum obtained shows that the capillary plasma formed is primarily consisting of iron (Fe) plasma. In order to check the contribution of the emission from the trigger spark towards the spectrum shown in Figure 5.3, the time-integrated visible spectrum of the trigger spark alone has been obtained separately as shown in Figure 5.4. It is clear that the spectral emission from the trigger spark is insignificantly weak compared to that of the main discharge.

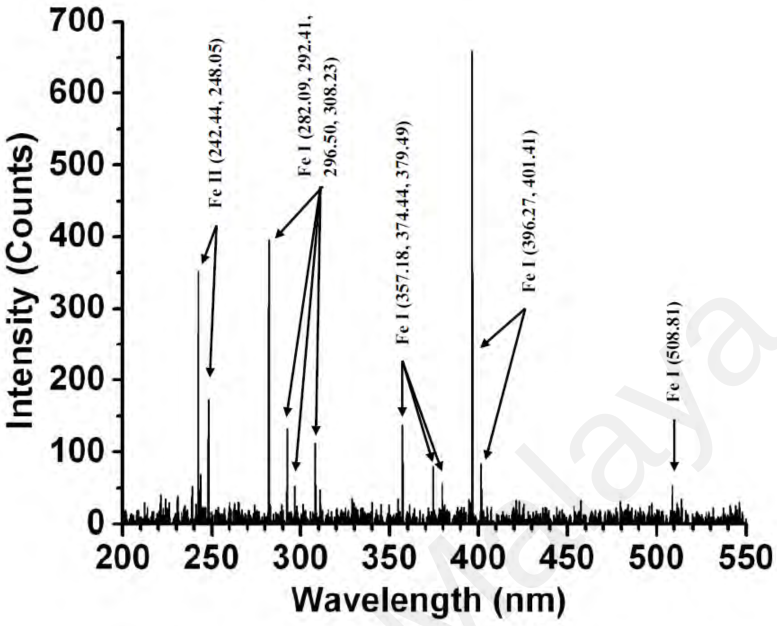

Figure 5.3: Time integrated spectrum of the visible emission detected by the spectrometer in the spectral region of 200- 550 nm at voltage of 24 kV and pressure of 10^{-5} mbar.

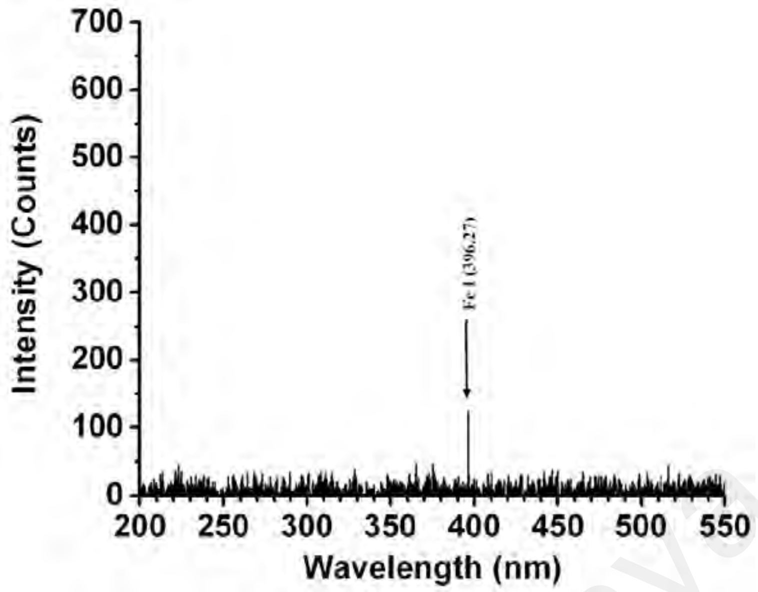

Figure 5.4: Time integrated spectrum of the visible emission of the HCR plasma detected by the spectrometer in the spectral region of 200- 550 nm.

The jet of the evaporated anode material that is injected into the capillary channel to form the capillary plasma is being heated up by the high discharge current and eventually emits in the EUV region. Figure 5.5 shows the EUV radiation emitted from the stainless steel capillary plasma detected by the SXUVHS5 Si/Zr 100/200 nm photodiode with sensitive region detection of 11-18 nm (Saboohi *et al*., 2012). It is observed that the EUV is dominant in the first cycle of the discharge current. An example of X-ray and EUV oscilloscope obtained simultaneously for a single discharge are shown in Figure 5.6. It is clear that the EUV is emitted after the emission of X-ray. Detailed studies of these emissions under different experimental conditions will be presented in the following sections of this chapter.

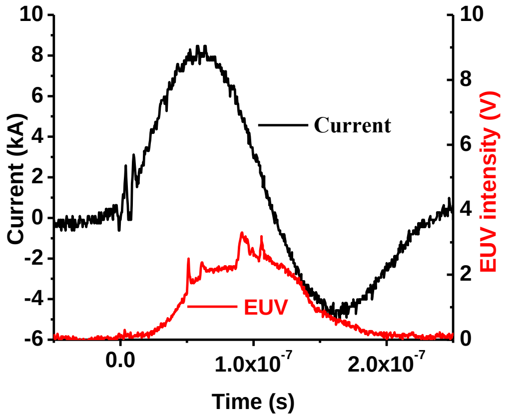

Figure 5.5: Typical current signal and EUV emission (11-18 nm) at the discharge voltage of 24 kV and pressure of 10^{-5} mbar.

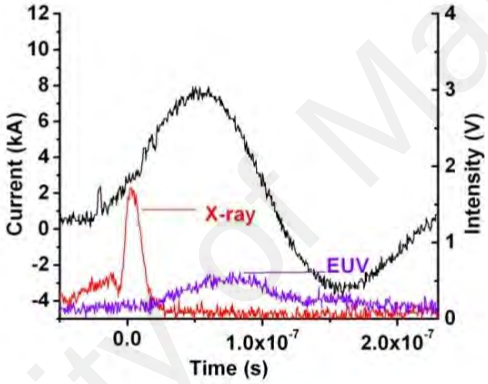

Figure 5.6: Typical current signal, X-ray and EUV emission (11-18 nm) at the discharge voltage of 24 kV and pressure of 10^{-5} mbar.

As the discharge current flowing through the plasma decreases in the reverse cycle of the current, the plasma cools down and begins to emit mostly in the visible region. Figure 5.7 exhibits the visible emission of the plasma detected by the BPX 65 PIN diode with spectral sensitivity range of UV to the near IR. Detailed studies of the visible emission of the plasma under different experimental conditions will be presented in the following sections of this chapter.

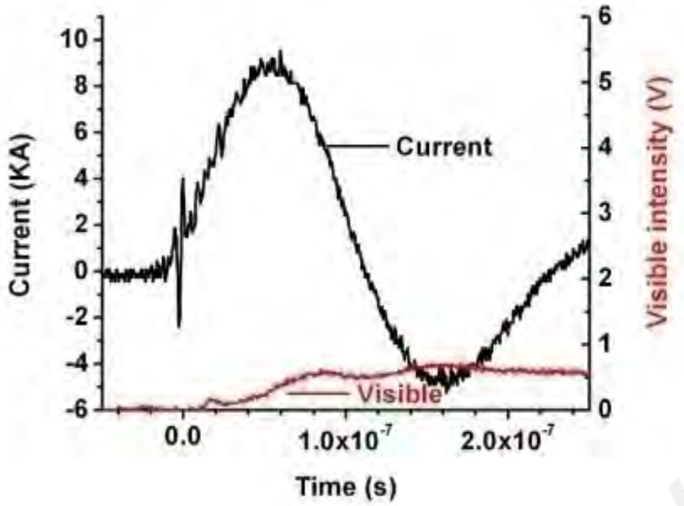

Figure 5.7: Typical current signal and visible emission at the discharge voltage of 24 kV and pressure of 10^{-5} mbar.

5.2 Pre-breakdown phase of the Capillary Discharge

The pre-breakdown phenomenon is based on the transient hollow cathode discharge (THCD) concept (Avaria *et al*., 2009, Wong *et al*., 1992, Wong *et al*., 1995, Krisch *et al*, 2000, Favre *et al.*, 2008). As mentioned earlier, upon triggering, local ionization occurs and results in the formation of hollow cathode (HC) plasma. This is evidenced from the initiation of emission of low level visible light at 200 ns before the initiation of the main discharge as can be observed in Figure 5.1.

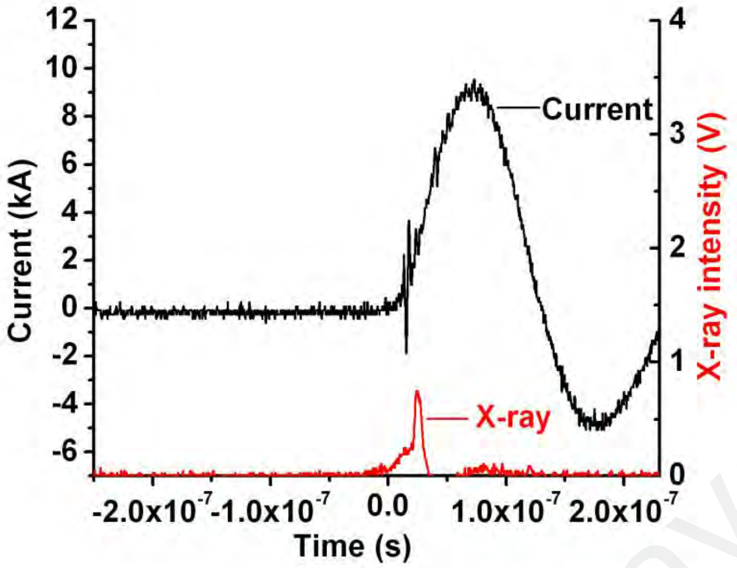

Figure 5.8: Typical current signal, low level light emission at the HCR and X-ray emission at the pressure of 10^{-5} mbar.

The applied electric field generated due to the voltage across the electrodes leaks through the cathode aperture and extracts the electrons from the HC plasma. The electrons are accelerated along the capillary channel and causes collisional ionization with the gas particles in the capillary channel as is indicated by the low level visible emission as shown in Figure 5.1, leading to the formation of high energy on-axis electron beams (Avaria *et al*., 2009) to bombard at the tip of the anode. It is noticed that there is a low level emission of X-ray with an amplitude of less than 0.25 V between 0 s and 20 ns (Figure 5.8). This indicates that a few excursions of electron beams to the anode are made prior to the sharp X-ray spike leading to the breakdown of the main discharge gap along the capillary channel.

4.3 Emission of a Metallic (Stainless Steel) Capillary Plasma

4.3.1 X-ray Emission

In order to obtain a comprehensive study on the metallic capillary plasma based on emission (in this study, stainless steel capillary plasma is used), the study must begin at the moment when the discharge is initiated. The X-ray emission which occurs at the initiation of the discharge due to bombardment of transient hollow cathode effect generated electron beam onto the anode are obtained and studied at various discharge voltages and operating pressures.

The operating pressure plays a significant role on the X-ray emission. The X-ray emission at the initiation of the capillary discharge is obtained at operating pressure in the range of 10^{-3}-10^{-5} mbar in order to determine the suitable condition for the initiation of the capillary discharge.

Figure 5.9 shows the X-ray emission obtained at operating pressure of 10^{-3} mbar, 10^{-4} mbar and 10^{-5} mbar and discharge voltage of 24 kV. It is observed that the X-ray intensity obtained at the operating pressure of 10^{-5} mbar is 1.6 V. As evidenced in Figure 5.9, the X-ray intensity drops to 0.9 V at the pressure of 10^{-4} mbar and finally to almost 0 V at the pressure of 10^{-3} mbar. This is because as the electron beam from the HCR plasma accelerated along the capillary channel, the electron beam will collide with the air particles and energy will transfer to the air particle in the capillary channel. At higher pressure there are more air particles in the capillary per unit volume and hence the collision cross section, σ is larger compared to that at lower pressure. Thus, the electron beam that reaches the anode at $P = 10^{-5}$ mbar has higher energy and is able to evaporate the anode tip effectively compared to the cases of $P = 10^{-4}$ mbar and $P = 10^{-3}$ mbar.

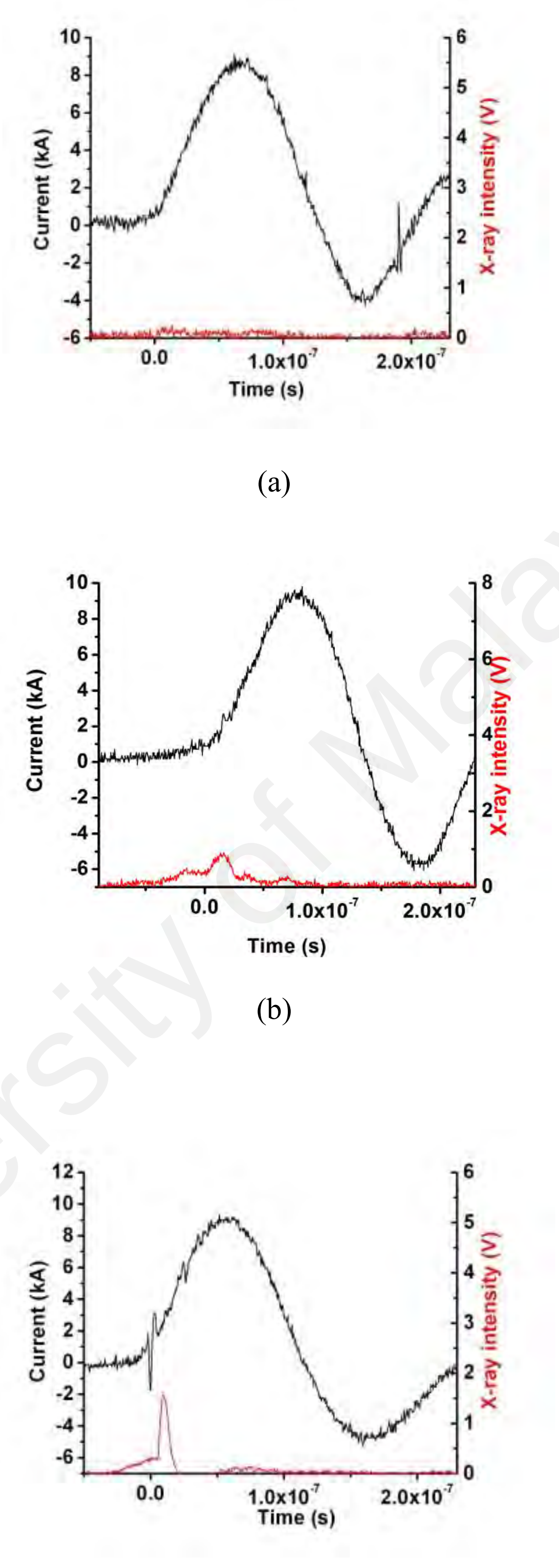

(a)

(b)

(c)

Figure 5.9: The X-ray emission obtained at the pressure of (a) 10^{-3} mbar (b) 10^{-4} mbar (c) 10^{-5} mbar and discharge voltage of 24 kV.

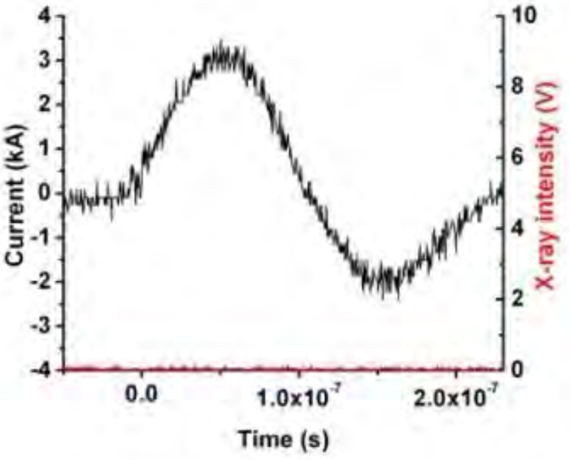
Current (kA)
X-ray intensity (V)
Time (s)
4
3
2
1
0
-1
-2
-3
-4
10
8
6
4
2
0
0.0
1.0x10^-7
2.0x10^-7

(a)

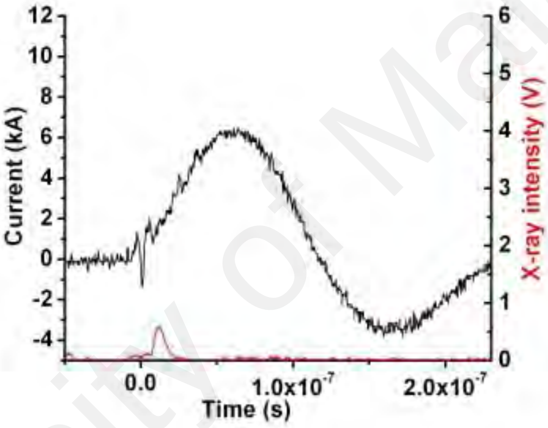
Current (kA)
X-ray intensity (V)
Time (s)
12
10
8
6
4
2
0
-2
-4
6
5
4
3
2
1
0
0.0
1.0x10^-7
2.0x10^-7

(b)

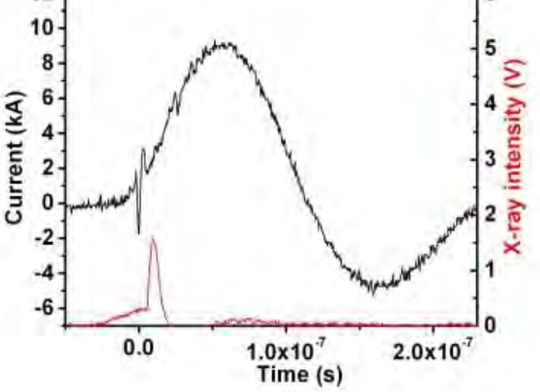
Current (kA)
X-ray intensity (V)
Time (s)
12
10
8
6
4
2
0
-2
-4
-6
6
5
4
3
2
1
0
0.0
1.0x10^-7
2.0x10^-7

(c)

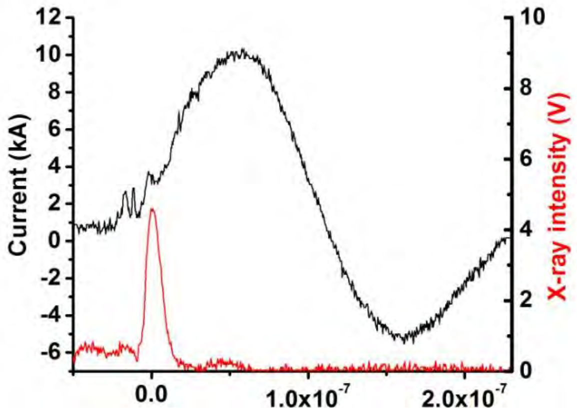

(d)

Figure 5.10: Typical current signal and the X-ray emission obtained at the discharge voltage of (a) 8 kV, (b) 16 kV, (c) 24 kV and (d) 26 kV at the pressure of 10^{-5} mbar.

Besides operating pressure, the effect of the discharge voltage is taken into consideration as well. In our experiment, the discharge voltage is varied from 8 to 26 kV as self-breakdown occurs frequently at 27 kV (the maximum charging voltage allowed for the capacitors is 30 kV). The lowest discharge voltage that enables the breakdown to occur at the pressure of 10^{-5} mbar is 8 kV. However, no emission of X-ray is observed at 8 kV discharge voltage as shown in Figure 5.10. It is believed that the X-ray emission intensity is very low and it is below the detection threshold of the PIN diode (with 24 µm aluminized mylar).

As the applied voltage is increased, the electrons beam generated in the THCD is accelerated to a higher energy and intensity due to the higher applied electric field. When bombardment of the electron beam at the anode tip occurs, higher intensity of energy is transferred to the anode tip. Thus, a more intense evaporation of the anode material will occur (this will be discussed later in section 5.3.2). This is evidenced from a stronger intensity of X-ray emission for higher discharge voltage as depicted in Figure 5.10. Figure 5.10 (d) shows the typical current signal and the X-ray emission obtained at the discharge voltage of 26 kV and pressure of 10^{-5} mbar. It is noticed that the amplitude of the X-ray pulse is higher than 4V. The effect of discharge voltage is also observed in the operating pressure of 10^{-4} mbar as shown in Figure 5.11.

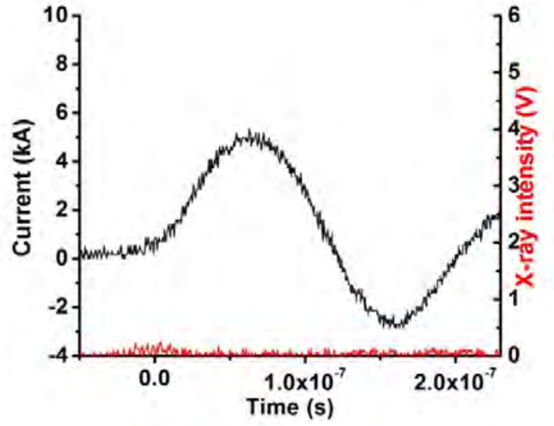
10
8
6
4
2
0
-2
-4
Current (kA)
6
5
4
3
2
1
0
X-ray intensity (V)
0.0
1.0x10-7
2.0x10-7
Time (s)

(a)

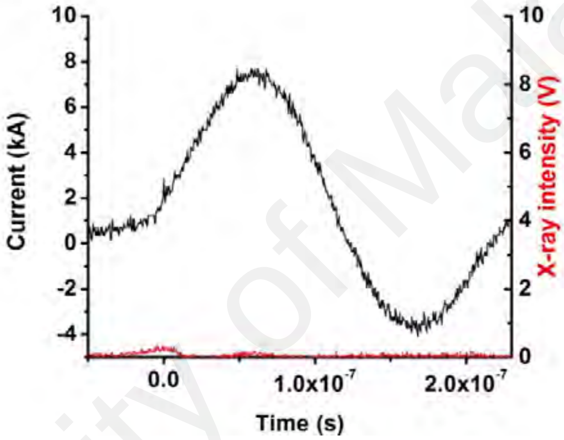
10
8
6
4
2
0
-2
-4
Current (kA)
10
8
6
4
2
0
X-ray intensity (V)
0.0
1.0x10-7
2.0x10-7
Time (s)

(b)

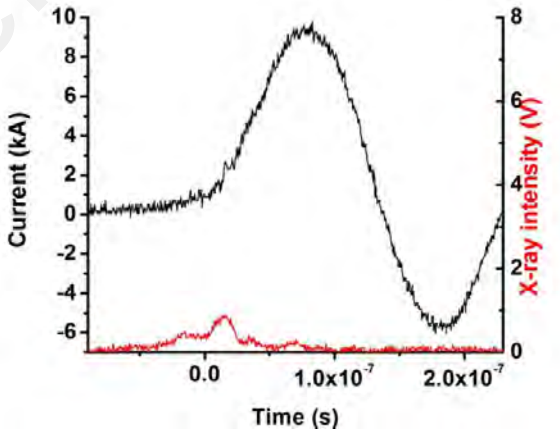
10
8
6
4
2
0
-2
-4
-6
Current (kA)
8
6
4
2
0
X-ray intensity (V)
0.0
1.0x10-7
2.0x10-7
Time (s)

(c)

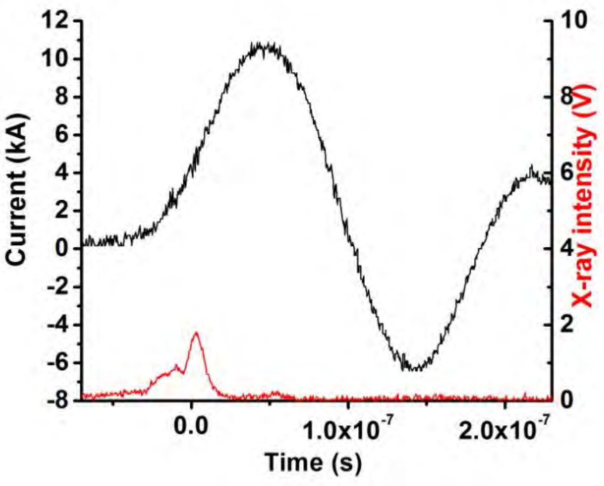

(d)

Figure 5.11: Typical current signal and the X-ray emission obtained at the discharge voltage of (a) 10 kV (b) 18 kV (c) 24 kV (d) 26 kV and pressure of 10^{-4} mbar.

However, the effect of discharge voltage on the X-ray emission is observed to be not significant as the pressure is raised to 10^{-3} mbar. The X-ray emission intensity remains the same, even though the discharge voltage is varied as exhibited in Figure 5.12. It is believed that the X-ray emission at the pressure of 10^{-3} mbar for discharge voltages from 8 to 26 kV is below the threshold detection of the X-ray PIN diode (with 24 µm aluminized mylar).

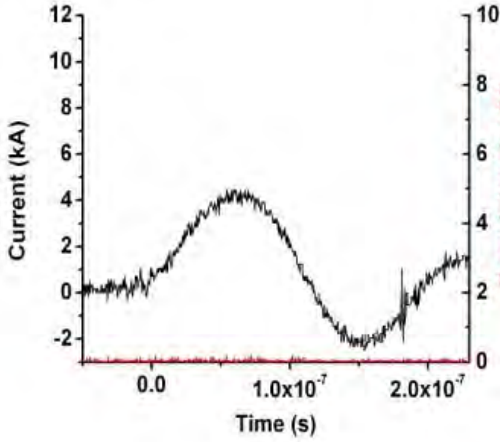

(a)

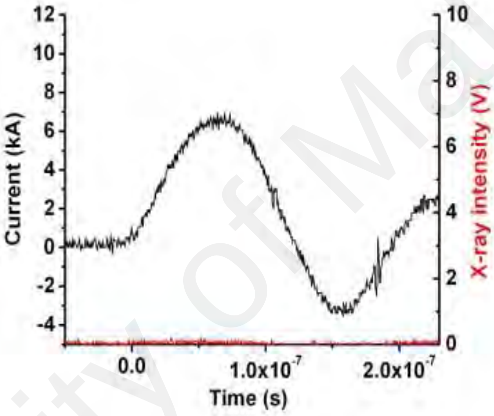

(b)

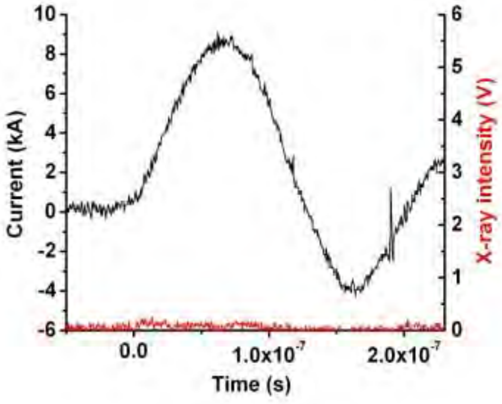

(c)

Figure 5.12: Typical current signal and the X-ray emission obtained at the discharge voltage of (a) 10 kV (b) 16 kV (c) 24 kV and pressure of 10^{-3} mbar.

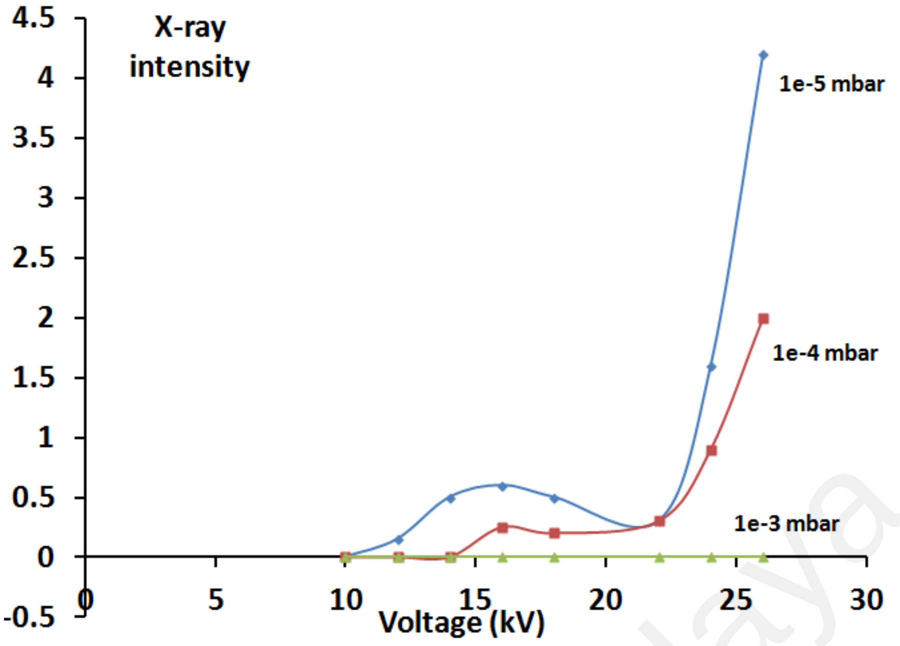

Figure 5.13: X-ray intensity at range of pressure from 10^{-3} to 10^{-5} mbar and discharge voltage of 10 to 26 kV.

Thus, it is observed that the X-ray emission which is produced due to the bombardment of THCD electron beam on the anode that will evaporate the anode material achieves its highest intensity at the pressure of 10^{-5} mbar for different discharge voltages (10-26 kV) as shown in Figure 5.13. This X-ray emission which is obtained at the initiation of the discharge is related to the evaporation of the anode material that will act as plasma fuel which will be discussed in the following section.

5.3.2 Evaporation of anode material as plasma fuel (stainless steel)

As mentioned earlier in section 5.1, the bombardment of the THCD electron beam (which is indicated by the X-ray emission at the initiation of the discharge as discussed in section 5.3.1) will evaporate the anode material and subsequently injects into the capillary as plasma fuel. This is evidenced from the spectral lines obtained using visible spectrometer, which portrays a plasma predominated by Fe which is originated from a stainless steel anode.

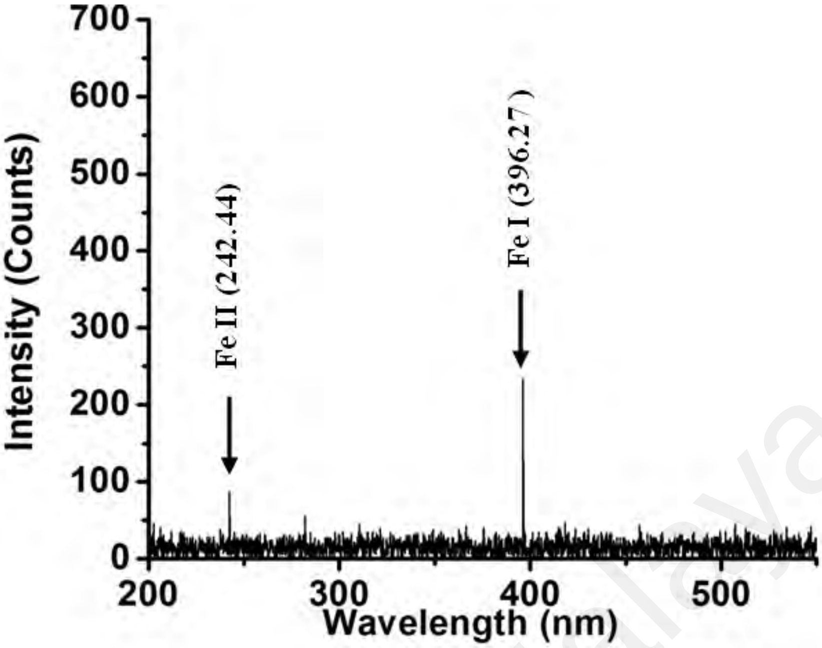
700
600
500
400
300
200
100
0
Intensity (Counts)
200
300
400
500
Wavelength (nm)
Fe II (242.44)
Fe I (396.27)

(a)

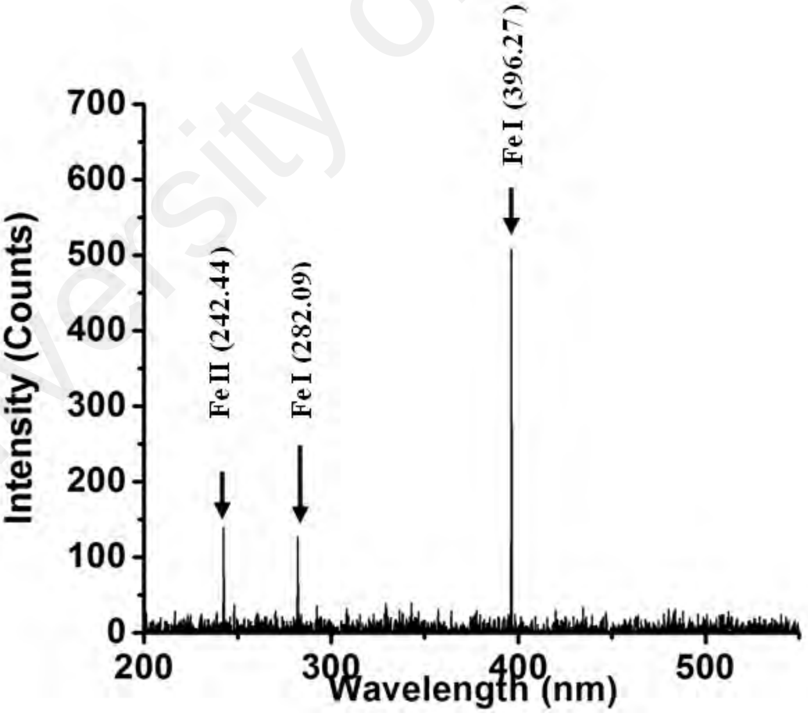
700
600
500
400
300
200
100
0
Intensity (Counts)
200
300
400
500
Wavelength (nm)
Fe II (242.44)
Fe I (282.09)
Fe I (396.27)

(b)

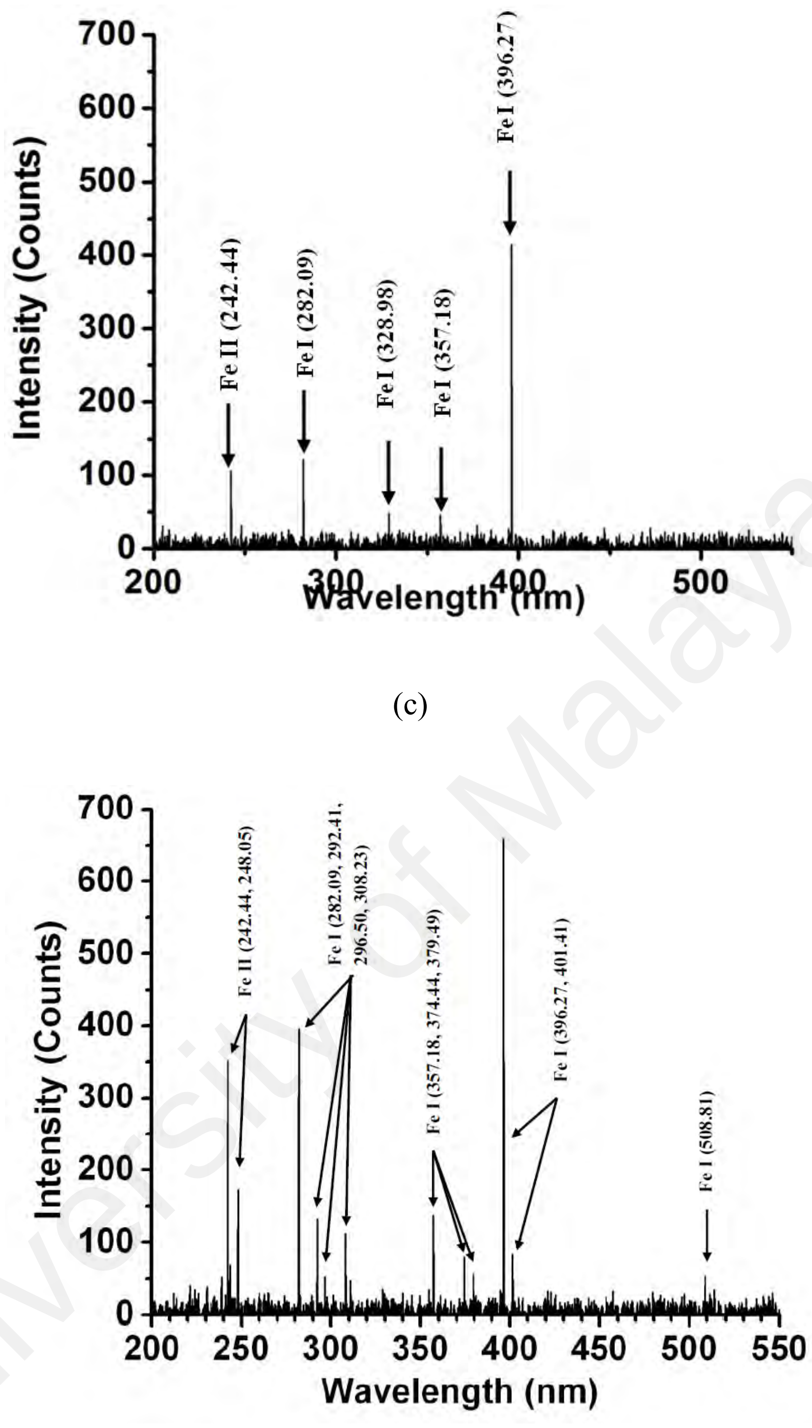

(c)

(d)

Figure 5.14: Time-integrated spectrum of the visible emission of the plasma at the discharge voltage of (a) 8 kV, (b) 16 kV, (c) 20 kV and (d) 24 kV with pressure of 10^{-5} mbar at range of wavelength of 200-550 nm.

Figure 5.14 (a) exhibits the visible spectrum of the plasma at the discharge voltage of 8 kV after the trigger signal is eliminated. Emission lines are observed at wavelengths of 396.27 nm and 242.44 nm respectively. These two spectral lines are identified as Fe^+ (Fe II) and Fe (Fe I) respectively as stated in the NIST database (*National Institute of Standard and Technology, 2013*). Table 5.1 shows the information of these two emission lines that are obtained from the NIST database (National Institute of Standard and Technology, 2013).

Table 5.1: Visible emission lines of the stainless steel (Fe dominant) capillary plasma at the discharge voltage (a) 8 kV, (b) 16 kV, (c) 20 kV and (d) 24 kV at the pressure of 10^{-5} mbar

Ionic species	Wavelength (nm)	Wavelength (nm) [*National Institute of Standard and Technology, 2013*]
Fe II (Fe^+)	242.44	242.48
Fe I (Fe)	396.27	396.31

(a)

Ionic species	Wavelength (nm)	Wavelength (nm) [*National Institute of Standard and Technology, 2013*]
Fe II (Fe^+)	242.44	242.48
Fe I (Fe)	282.09	282.09
Fe I (Fe)	396.27	396.31

(b)

Ionic species	Wavelength (nm)	Wavelength (nm) [*National Institute of Standard and Technology, 2013*]
Fe II (Fe^+)	242.44	242.48
Fe I (Fe)	282.09	282.09
Fe I (Fe)	328.98	328.94
Fe I (Fe)	357.18	357.19
Fe I (Fe)	396.27	396.31

(c)

Ionic species	Wavelength (nm)	Wavelength (nm) [*National Institute of Standard and Technology, 2013*]
Fe II (Fe^+)	242.44	242.48
Fe II (Fe^+)	248.05	248.10
Fe I (Fe)	282.09	282.09
Fe I (Fe)	292.41	292.42
Fe I (Fe)	296.50	296.53
Fe I (Fe)	374.44	374.41
Fe I (Fe)	379.49	379.50
Fe I (Fe)	357.18	357.19
Fe I (Fe)	396.27	396.31
Fe I (Fe)	401.41	401.43
Fe I (Fe)	508.81	508.82

(d)

As the discharge voltage is increased to 16 kV, 18 kV and 24 kV respectively, more emission lines of Fe at various wavelengths are observed such as Fe^+(Fe II) at 248.05 nm and Fe (Fe I) at (282.09 nm, 292.41 nm, 296.50 nm, 308.23 nm, 328.98 nm, 357.18 nm, 374.44 nm, 379.49 nm, 404.41 nm and 508.81 nm).

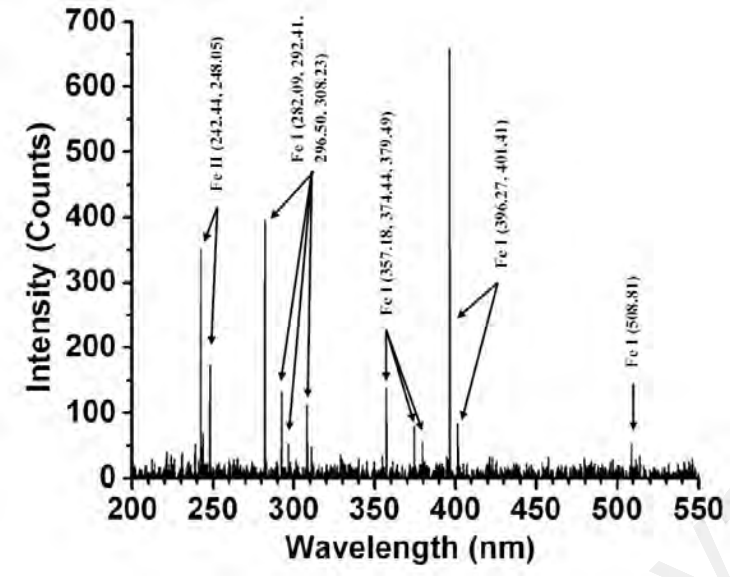

(a)

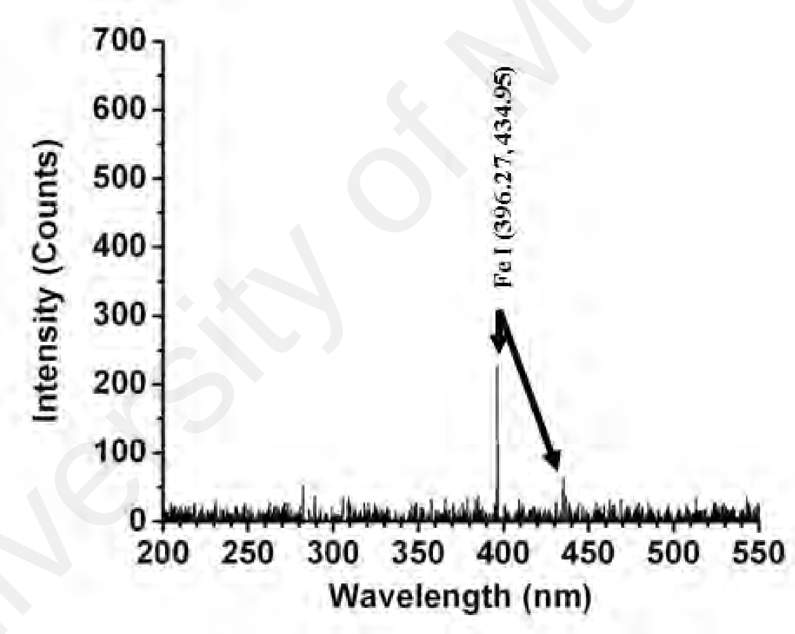

(b)

Figure 5.15: Time-integrated spectrum of the visible emission of the plasma at the discharge voltage of 10 kV and pressure of (a) 10^{-5} mbar and (b) 10^{-3} mbar at range of wavelength of 200 -650 nm.

As discussed in section 5.3.1 at higher pressure (10^{-3} mbar) the electron beam from the HCR plasma is not effective in the evaporation of the anode material compared to lower pressure (10^{-5} mbar). This is evidenced from the significant reduction of X-ray emission intensity and the absence of current dip in the current signal at the initiation of the discharge as shown in Figure 5.9. As the jet of the evaporated anode materials penetrates into the capillary to form the capillary plasma during the main discharge, the time-integrated spectrum in Figure 5.15 shows that there is less Fe emission lines observed from the plasma of higher pressure (10^{-3} mbar) compared to lower pressure (10^{-5} mbar). Thus, the time-integrated spectrum also further confirms that the evaporation of the anode is less effective in the case of higher pressure (10^{-3} mbar).

The stainless steel anode vapor which consists of predominantly Fe will subsequently be injected into the capillary channel as fuel for the capillary plasma that emits in the EUV and visible region. In the following section, we are going to study and discuss the EUV radiation that is emitted from the capillary plasma.

5.3.3 EUV Emission of Stainless Steel Plasma

The jet of the evaporated anode material (stainless steel) is injected into the capillary to form plasma. The plasma starts to emit in the EUV region once the discharge is initiated and the plasma has been heated up sufficiently. The EUV emission of the stainless steel capillary plasma is detected by using SXUVHS5 Si/Zr 100/200 nm photodiode (sensitive to the range of wavelength of 11-18 nm) at the discharge voltage of 10 to 26 kV and operating pressure of 10^{-3} to 10^{-5} mbar.

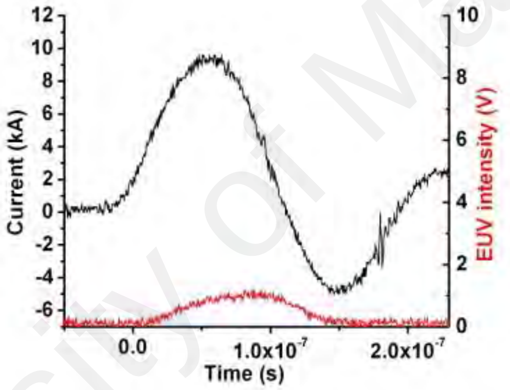

(a)

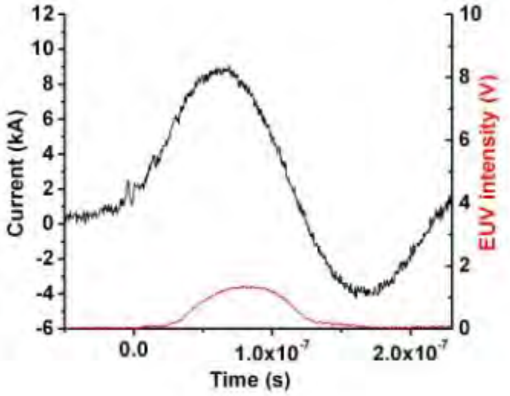

(b)

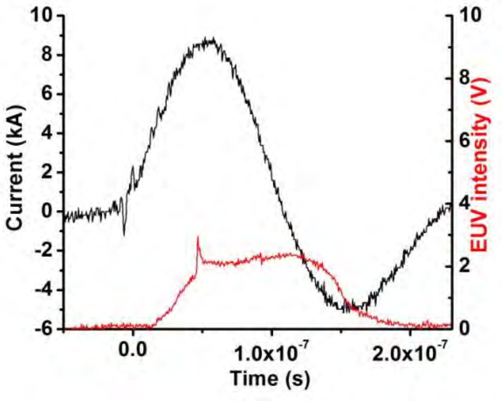

(c)

Figure 5.16: Typical current signal and EUV emission (11-18 nm) at the discharge voltage of 26 kV and pressure of (a) 10^{-3} mbar, (b) 10^{-4} mbar and (c) 10^{-5} mbar.

Figure 5.16 exhibits the time-resolved EUV emission of the stainless steel capillary plasma at the discharge voltage of 26 kV and operating pressure of 10^{-3} mbar, 10^{-4} mbar and 10^{-5} mbar. The EUV intensity rises gradually with current signal during the first quarter cycle of the current signal. This suggests that the increase of EUV emission is caused by joule heating effect of the plasma (Valenzuela *et al*., 2012). At the pressure of 10^{-5} mbar, a sharp spike occurs in the EUV signal during the current peak. It is believed that an extremely fast event has occurred which gives rise to this transient disturbance in the EUV signal. The EUV emission at the pressure of 10^{-5} mbar has a faster rise time compared to the EUV emission at the pressure of 10^{-3} mbar and 10^{-4} mbar. This is because the joule heating (Valenzuela *et al*., 2012) of the stainless plasma at the pressure of 10^{-5} mbar is more effective as there is less air particles compared to that at the pressure of 10^{-3} mbar and 10^{-4} mbar and thus, causes the rate of joule heating to be higher. At the operating pressure of 10^{-3} mbar and 10^{-4} mbar, the EUV energy emitted from the stainless steel plasma has a peak intensity of 1.2 V for both operating pressures and a total energy of 10.2 mJ and 11.3 mJ respectively whereas when the operating pressure is decreased to 10^{-5} mbar, the peak intensity of the EUV emission reaches an amplitude of about 3 V corresponding to an estimated total EUV energy of 32.8 mJ.

As the operating pressure is increased to 10^{-4} mbar and eventually to 10^{-3} mbar, the electron beam from the HCR plasma is not effective in the erosion of the anode compared to lower pressure (10^{-5} mbar). This is evidenced from the significant difference of intensity of X-ray emission occurs at the initiation of the discharge as depicted in Figure 4.9. Due to the frequent collision of the THCD electron beam with the air particles (as discussed in section 5.3.1), the electron beam that reaches the anode at $P = 10^{-4}$ mbar and $P = 10^{-3}$ mbar is less energetic and is unable to evaporate the anode tip effectively compared to the case of $P = 10^{-5}$ mbar. Thus, there is less amount of stainless steel ion contributing to the formation of the capillary metallic plasma. This leads to lower emission of EUV at higher operating pressure compared to lower operating pressure.

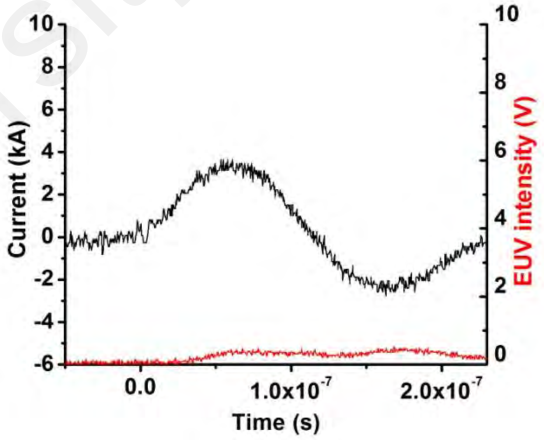

(a)

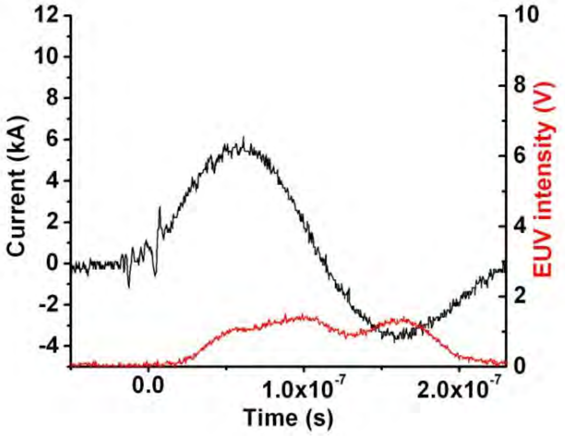

(b)

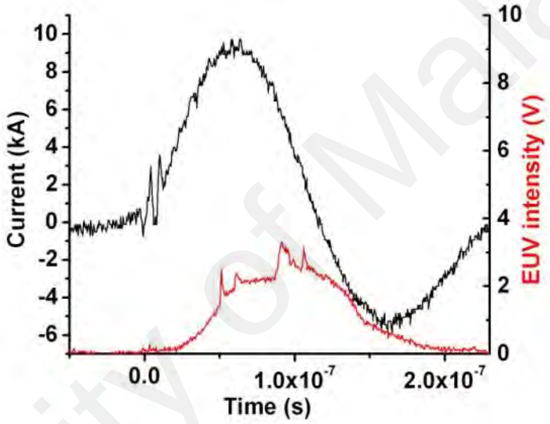

(c)

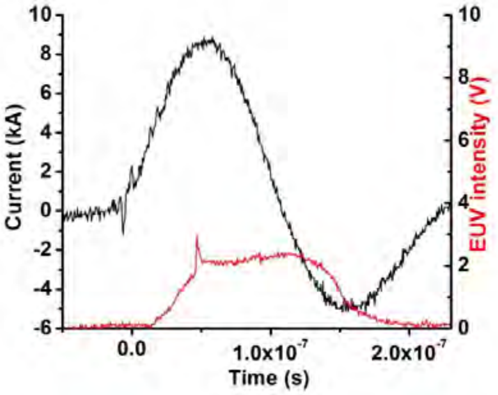

(d)

Figure 5.17: Typical current signal and EUV emission (11-18 nm) at the discharge voltage of (a) 10 kV (b) 16 kV (c) 24 kV and (d) 26 kV and pressure of 10^{-5} mbar.

Figure 5.17 exhibits the EUV signal emitted from the capillary plasma at the discharge voltages of 10 kV, 16 kV, 24 kV and 26 kV and pressure of 10^{-5} mbar. At 10 kV, the EUV energy emitted is only 7.56 mJ with total input energy of 1.08 J. It is evidenced that the input energy produced at the discharge voltage of 10 kV is not sufficient to heat up the plasma to emit in the EUV region. When the discharge voltage is increased to 16 kV, corresponding to an input energy of 2.76 J, the EUV energy produced reaches 20.7 mJ. It is noticed that the intensity of the EUV emission at the discharge voltages of 16 kV and 24 kV reaches maximum intensity at about 40 ns after the current peak. It is believed that in these cases the plasma is overheated at the time of the current peak so that the radiation emitted has wavelength beyond the detection range of the EUV detector. The output EUV energy achieved at 26 kV is 32.8 mJ. It is also noticed that in the EUV signals obtained at discharge voltages of 24 kV and 26 kV show a variable number of spikes. This is due to the fast increase in plasma temperature.

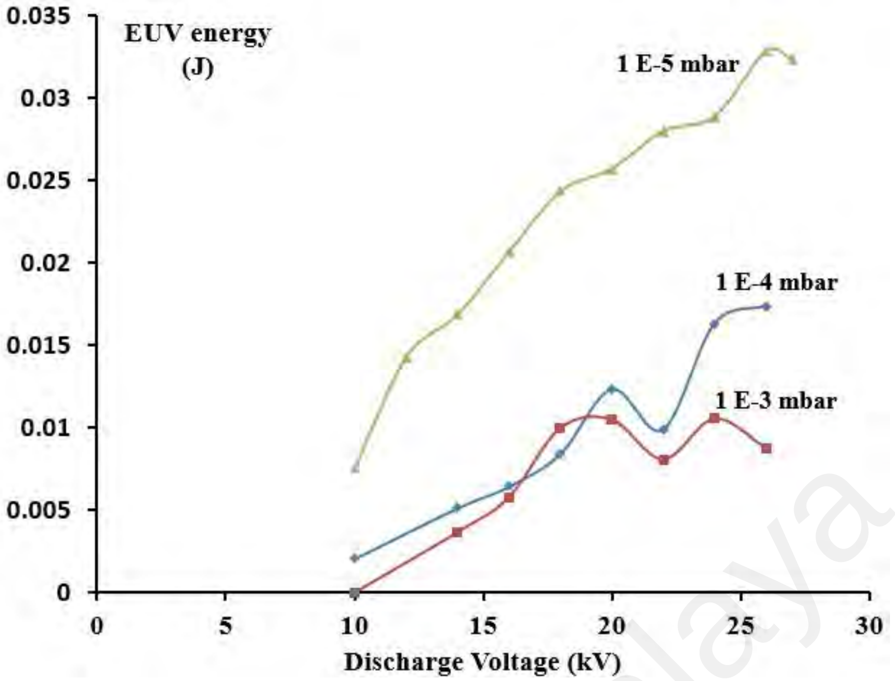

Figure 5.18: EUV energy of the stainless steel capillary plasma at the discharge voltage of 10 to 26 kV and operating pressure of 10^{-3} to 10^{-5} mbar.

Table 5.2. Emission of EUV energy at the discharge voltage of 10 to 26 kV and operating pressure of 10^{-3} to 10^{-5} mbar.

Discharge Voltage (kV)	EUV energy (mJ)		
	P = 10^{-5} mbar	P = 10^{-4} mbar	P = 10^{-3} mbar
10	7.56	2.09	negligible
14	16.9	5.13	3.66
16	20.7	6.44	5.79
18	24.3	8.41	9.98
20	25.7	12.3	10.5
22	28.0	9.90	8.08
24	28.8	16.3	10.6
26	32.8	17.4	8.79

Figure 5.18 and table 5.2 indicate the EUV energy obtained at the discharge voltage of 10 to 26 kV and operating pressure of 10^{-3} to 10^{-5} mbar. It is observed that the EUV energy obtained at the pressure of 10^{-5} mbar is higher compared to that

obtained for 10^{-4} mbar and 10^{-3} mbar for the range of discharge voltage tested. This is because there is smaller amount of stainless steel plasma that contributes to the EUV emission due to weaker electron beam bombardment at the anode at higher pressure as discussed earlier in section 5.3.1. At the operating pressure of 10^{-5} mbar, the highest EUV energy achieved for stainless steel plasma is 32.8 mJ and it occurs at the discharge voltage of 26 kV. At the discharge voltage of 27 kV, the EUV energy emitted by the stainless steel plasma begins to drop. This is believed to be due to the fact that the plasma is overheated and starts to emit in shorter wavelength.

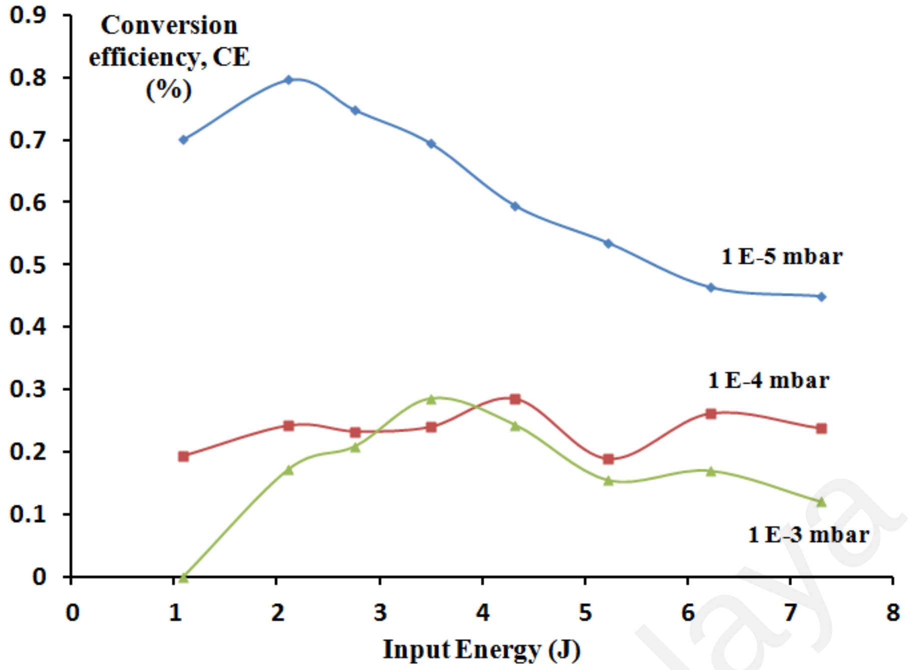

Figure 5.19: Conversion efficiency (CE) of EUV energy of the stainless steel capillary plasma for operating pressure of 10^{-3} to 10^{-5} mbar.

Table 5.3: Conversion efficiency (CE) of EUV energy of the stainless steel capillary plasma with input energy of 1.08 to 7.3 J (corresponds to the discharge voltage of 10 to 26 kV) and operating pressure of 10^{-3} to 10^{-5} mbar.

Discharge Voltage (kV)	Input Energy (J)	Conversion efficiency (%)		
		P = 10^{-5} mbar	P = 10^{-4} mbar	P = 10^{-3} mbar
10	1.08	7.00E-01	1.94E-01	0.00E+00
14	2.12	7.96E-01	2.43E-01	1.73E-01
16	2.76	7.47E-01	2.33E-01	2.09E-01
18	3.50	6.94E-01	2.40E-01	2.85E-01
20	4.32	5.95E-01	2.85E-01	2.43E-01
22	5.23	5.35E-01	1.89E-01	1.55E-01
24	6.22	4.64E-01	2.61E-01	1.70E-01
26	7.30	4.49E-01	2.38E-01	1.20E-01

Figure 5.19 shows the conversion efficiency of the EUV energy with respect to the input energy of the stainless steel capillary plasma at the discharge voltage of 10 to

26 kV and operating pressure of 10^{-3} to 10^{-5} mbar. It is observed that the stainless steel capillary plasma achieves its highest EUV energy conversion efficiency at the pressure of 10^{-5} mbar. The highest conversion efficiency of EUV energy of the stainless steel capillary plasma achieved is 0.8% which is corresponding to the discharge voltage of 14 kV (input energy of 2.12 J) and operating pressure of 10^{-5} mbar as shown in Table 5.3 and Figure 5.19.

5.3.4. Time-resolved Imaging of the Visible Stainless steel Plasma

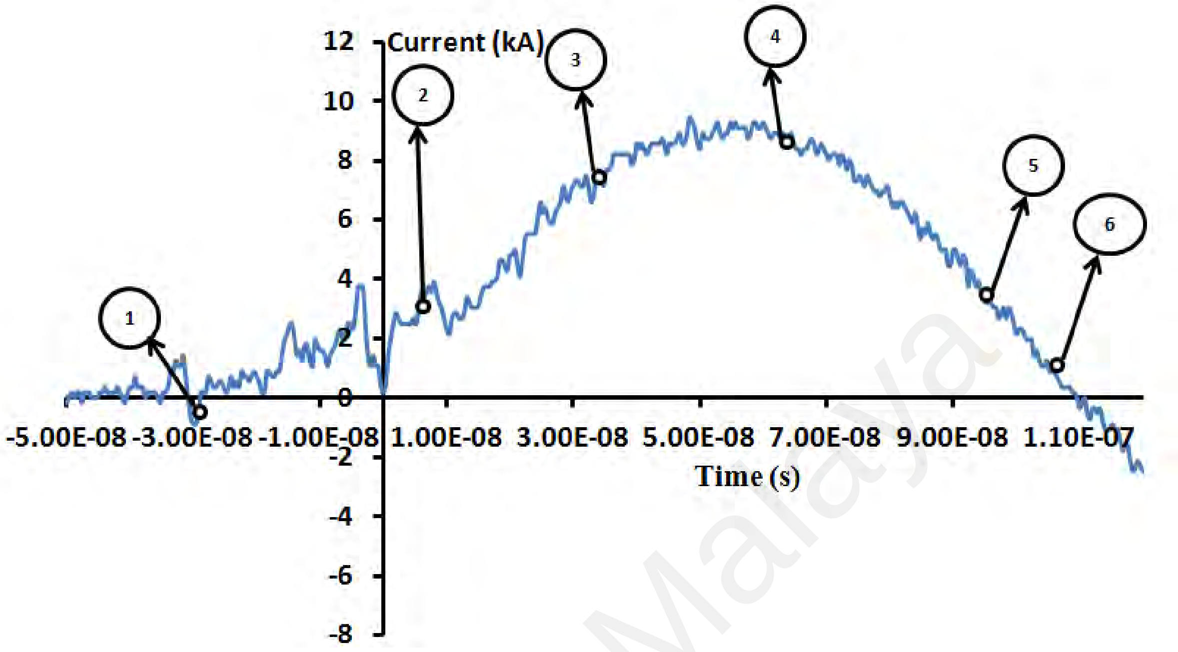

Figure 5.20 (a): Current waveform with labels at different times corresponding to the images that are shown in Figure 4.20 (b).

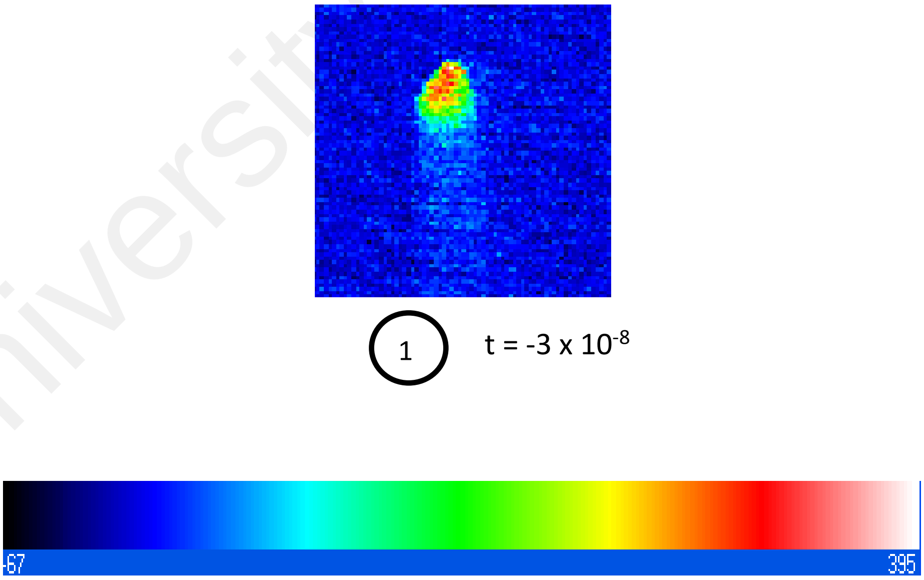

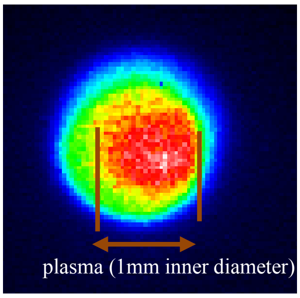

② $t = 7 \times 10^{-9}$ s

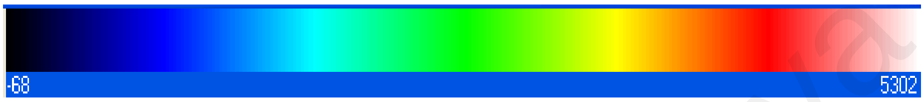

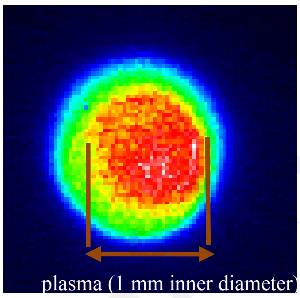

③ $t = 3.5 \times 10^{-8}$

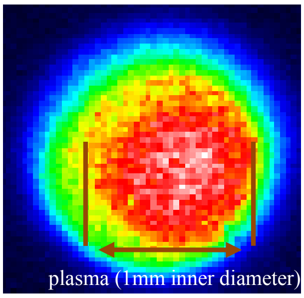

④ $t = 6.2 \times 10^{-8}$

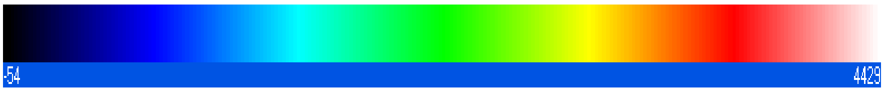

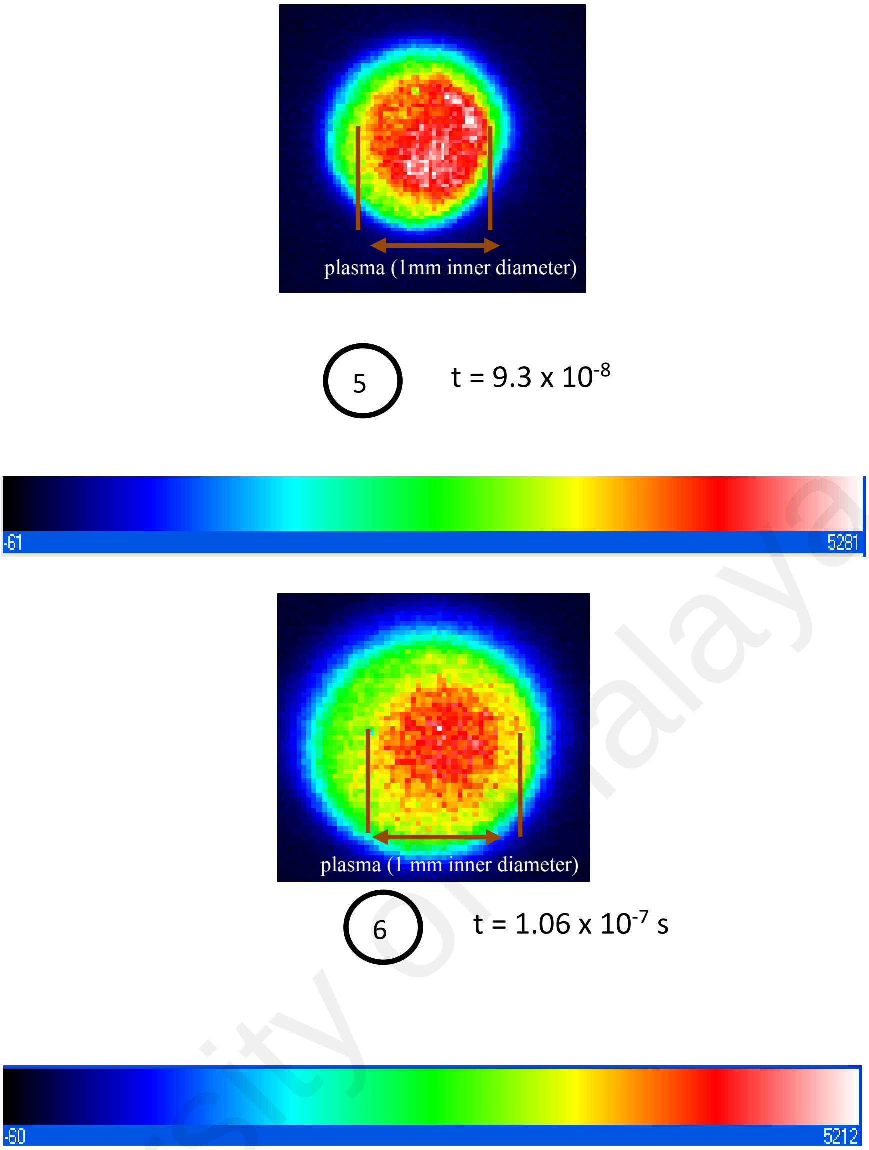

Figure 5.20 (b): Time-resolved visible images of the plasma. The pseudocolour indicates the relative intensity.

Figure 5.20 shows the current waveform and time-resolved visible images of the stainless steel capillary plasma obtained at the pressure of 10^{-5} mbar with peak current of around 9 kA. The quartz capillary used has an inner diameter of 1 mm and outer diameter of 6 mm. The tip of the triggering pin which is used to initiate the discharge has a length of 3 mm. The exposure time for each image is 4 s.

The capillary discharge is initiated by a triggering spark at the hollow cathode region as can be observed in image 1. The shadow of the triggering pin is observed in image 1. The plasma begin to form in the capillary shortly after the breakdown as low intensity of plasma emission is observed in image 2. As the current rises, the plasma is heated up gradually due to joule heating effect (image 2 and 3). The emission of the plasma is intense and the intensity becomes a lot more uniform at the current peak as portrayed in image 4. It is also observed that there is no compression of the plasma column. Then, the plasma begin to expand and diffuses to the capillary wall as exhibited in image 5. Finally, the plasma cools down as the magnitude of the discharge current continues to drop as shown in image 6. There is no severe compression of the plasma column observed as the plasma column size is consistent throughout the first half of the first cycle of the discharge. Thus, the plasma is dominated by joule heating and a resistive plasma column is formed.

5.4. Enhancement of EUV Emission from Capillary Plasma

Several efforts to enhance the efficiency of EUV energy produced from the stainless steel plasma for the range of discharge voltage of 10 to 26 kV and operating pressure of 10^{-3} 10^{-5} mbar will be discussed in this section. The effects of introducing argon gas into the capillary discharge, replacing the stainless steel anode by a copper anode and increasing the input electrical energy on the EUV energy enhancement will be investigated.

5.4.1. Effect of Ambient Gas on the EUV Emission

In order to investigate the effect of ambient gas on the EUV emission of the capillary discharge, argon gas is filled into the capillary for a series of discharges. The experimental parameters such as discharge voltage and operating pressure are varied in order to maximize the EUV production.

The experiment is carried out by pumping the capillary discharge chamber to a base pressure of 10^{-5} mbar and then argon gas is continuously flown in until the pressure of the chamber is maintained at 10^{-4} mbar throughout the experiment. Upon triggering, the stainless steel vapour of the anode is injected into the capillary and eventually a plasma consisting of a mixture of stainless steel vapour and argon is expected to be formed.

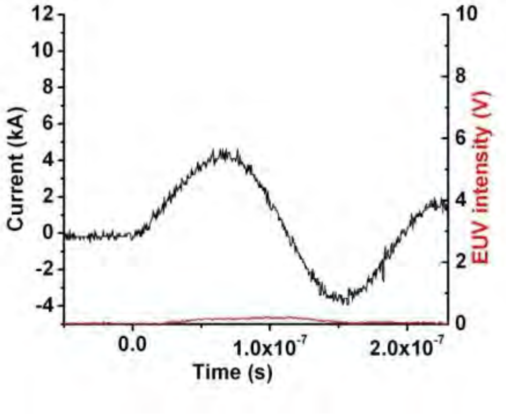

Current (kA)
EUV intensity (V)
Time (s)
0.0
1.0x10^-7
2.0x10^-7

(a)

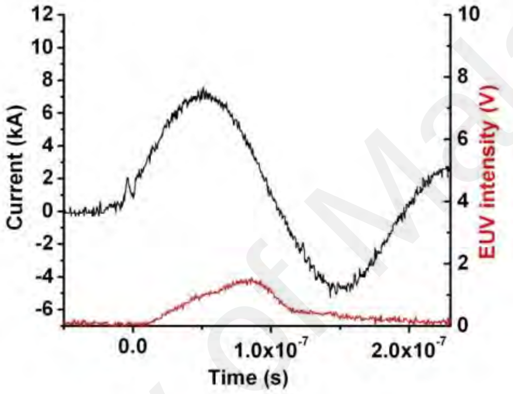

Current (kA)
EUV intensity (V)
Time (s)
0.0
1.0x10^-7
2.0x10^-7

(b)

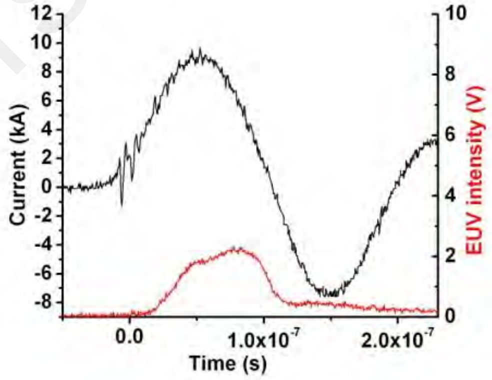

Current (kA)
EUV intensity (V)
Time (s)
0.0
1.0x10^-7
2.0x10^-7

(c)

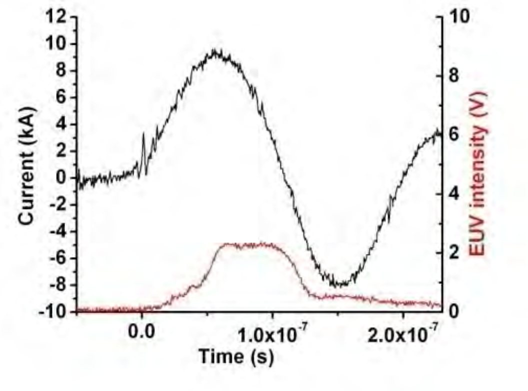

(d)

Figure 5.21: Typical current signal and the EUV emission obtained at the discharge voltage of (a) 10 kV (b) 18 kV (c) 24 kV (d) 26 kV and pressure of 10^{-4} mbar argon ambient.

At the discharge voltage of 10 kV, the EUV emission is very weak [Figure 5.21 (a)] and the EUV energy produced is only 2.1 mJ. The energy provided into the system is only 0.69 J. Thus, the input energy provided is not sufficient in order to heat up the capillary plasma into emitting EUV. Thus, the plasma is not able to reach the suitable temperature for EUV emission. In order to increase the energy provided for the heating of capillary plasma for EUV emission, the discharge voltage is increased gradually. At the discharge voltage of 18 kV, the EUV energy of the stainless steel-argon capillary plasma has increased to 13 mJ with peak intensity of 0.7 V.

As the voltage is increased to 24 kV which is corresponded to the total input energy of 6 J, the total EUV energy achieved is 21.7 mJ in Argon ambient. It is also noticed that the EUV signal at 24 kV has higher intensity throughout the period of the first half cycle of the discharge current compared to the EUV signal obtained at discharge voltage of 18 kV as observed in Figure 5.21. This is because the capillary plasma is heated up by discharge current that has shorter rise time at 24 kV compared to 18 kV and thus enable higher intensity of EUV emission.

In comparison of the EUV energy obtained at the pressure of 10^{-4} mbar between air ambient and Argon ambient, the EUV energy obtained in Argon ambient is higher compared to air ambient as portrayed in Figure 5.22. At 24 kV, the EUV energy achieved in air ambient is only 12.3 mJ, which is around 9 mJ less than the EUV produced in Argon ambient. In order to further confirm the cause of the difference between the EUV energy emitted in Argon ambient and air ambient is contributed from Argon plasma, the X-ray emission at the initiation of the discharge which shows the evaporation of the anode is obtained and is shown in Figure 5.23. It is evidenced that the evaporation of anode materials in air ambient is more significant compared to Argon ambient as the intensity of the X-ray at the initiation of the discharge in air ambient (0.9 V) is higher than the X-ray in Argon ambient (0.3 V). Thus, there are more stainless steel (dominated by Fe) vapour in air ambient compared to Argon ambient. This stainless steel will eventually contribute to the capillary plasma formation that will emit in the EUV region. However, the EUV energy of the capillary plasma obtained in Argon ambient is higher than air ambient for the discharge voltage of 24 kV and for other discharge voltages (10 to 26 kV) as well as portrayed in Figure 5.22 as stated above. Thus, it is confirmed that Argon gas plays a significant role in the EUV production compared to stainless steel vapour in Argon ambient.

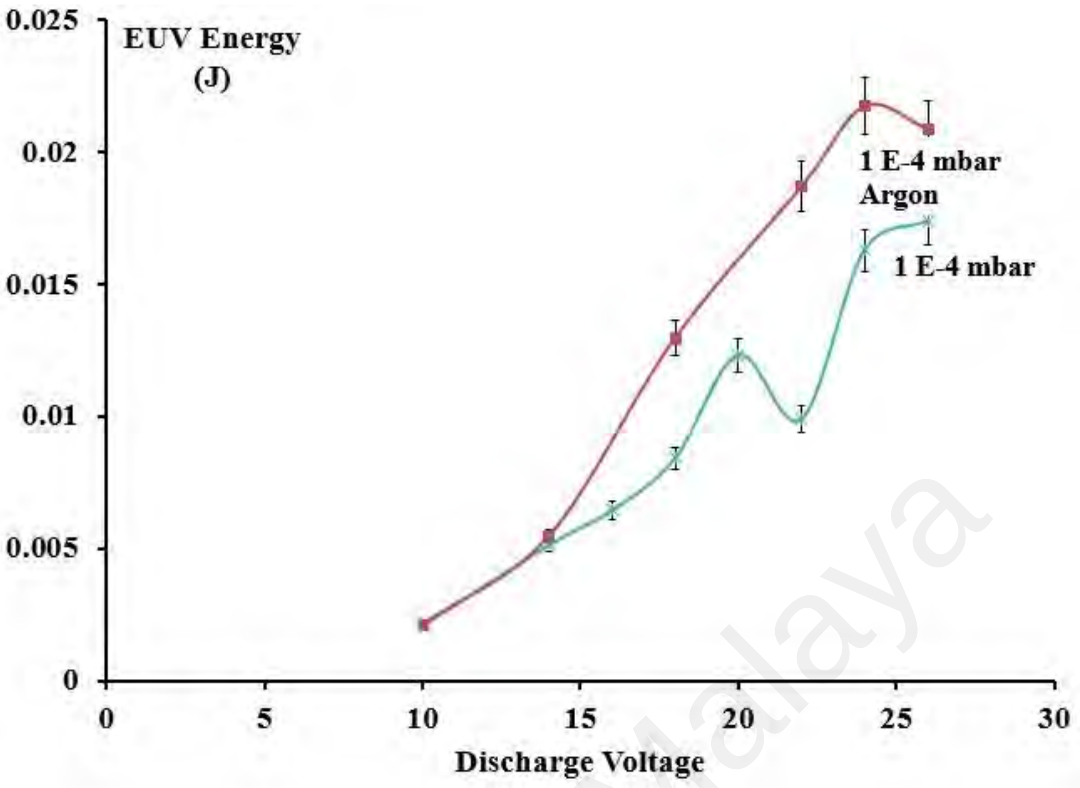

Figure 5.22: EUV energy of the stainless steel-argon capillary plasma at the pressure of 10^{-4} mbar Argon and stainless steel plasma at the pressure of 10^{-4} mbar air ambient at the discharge voltage of 10 to 26 kV.

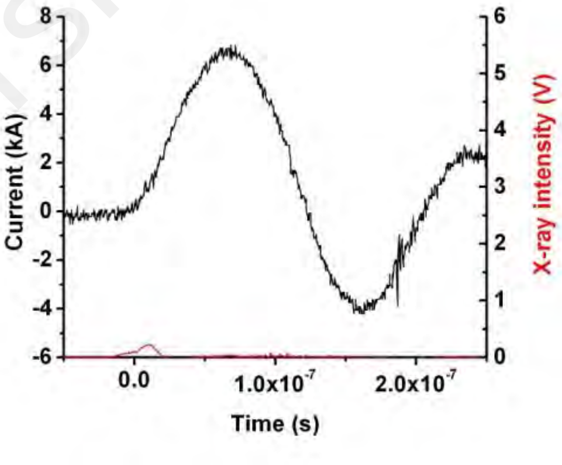

(a)

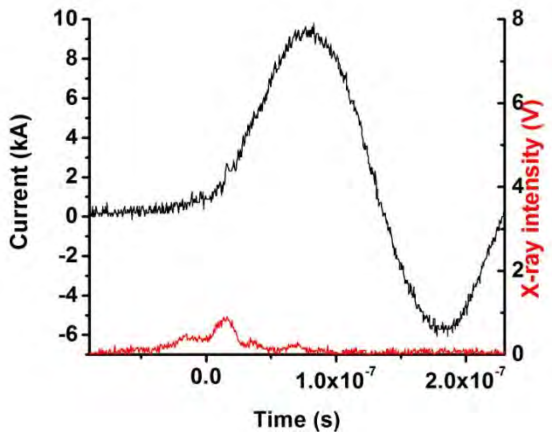

(b)

Figure 5.23: Typical current signal and the X-ray emission obtained at the discharge voltage of 24 kV and pressure of (a) 10^{-4} mbar argon ambient (b) 10^{-4} mbar air ambient.

The pressure of the Argon gas is varied in order to see its effect on the EUV enhancement. In this experiment, the pressure is varied in the range of 10^{-2} to 10^{-4} mbar. Figure 5.24 shows the EUV signal obtained at the discharge voltage of 18 kV at the pressure of 10^{-4} mbar and 10^{-2} mbar. It is observed that the maximum EUV intensity achieved by the plasma is higher at lower operating pressure (10^{-4} mbar) which is 1.5 V compared to 0.6 V at higher operating pressure (10^{-2} mbar) consistently. Thus, it is believed that the plasma at lower operating pressure emits in the wavelengths that is closer to 13.5 nm as the photodiode has the detective range of 11 to 18 nm with maximum sensitivity at 13.5 nm.

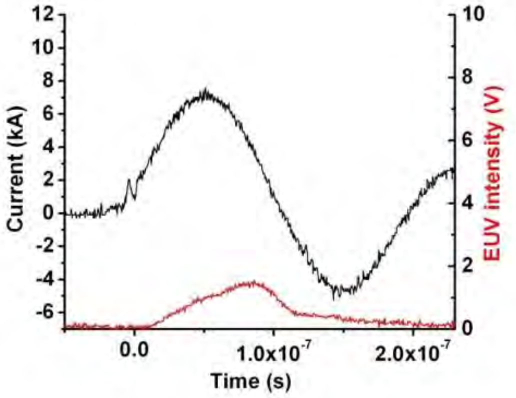

(a)

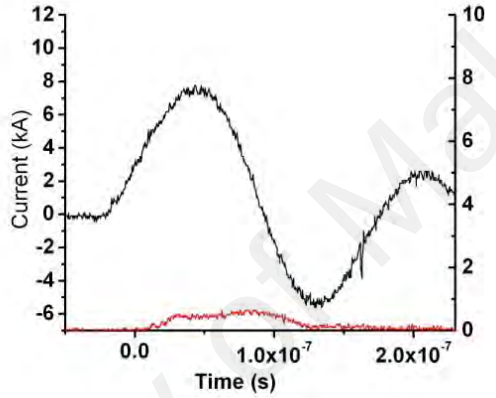

(b)

Figure 5.24: Typical current signal and the EUV emission obtained at the discharge voltage of 18 kV and pressure of (a) 10^{-4} mbar Argon ambient (b) 10^{-2} mbar Argon ambient.

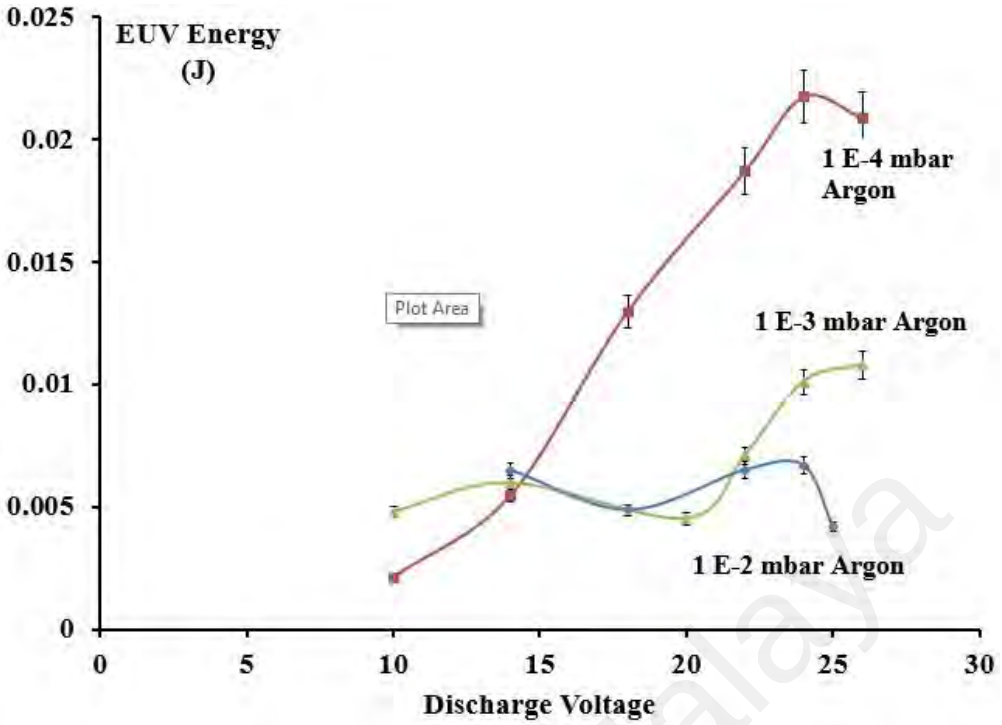

Figure 5.25: EUV energy of the argon ambient capillary plasma at the discharge voltage of 10 to 26 kV and operating pressure of 10^{-2} to 10^{-4} mbar.

It is observed that the operating pressure for the highest EUV energy production at most discharge voltage of the stainless steel-argon capillary plasma is 10^{-4} mbar as shown in Figure 5.25. The condition for highest EUV energy emission is at the discharge voltage of 24 kV and operating pressure of 10^{-4} mbar. The EUV energy achieved at this condition is 21.7 mJ which leads to a conversion efficiency of 0.35%.

Figure 5.26 shows the optimum operating pressure for EUV energy production in air ambient (which is at 10^{-5} mbar, the base pressure) and argon ambient (which is at 10^{-4} mbar) at the discharge voltage of 10 to 26 kV. It is observed that the highest EUV energy emitted by the stainless steel capillary plasma at 10^{-5} mbar air ambient (at 26 kV) is higher (with a difference 11.1 mJ) than the highest EUV energy emitted by the stainless steel-argon capillary plasma at 10^{-4} mbar argon ambient (at 24 kV). The EUV conversion efficiency achieved at 10^{-5} mbar air ambient and discharge voltage of 26 kV is 0.45% (Table 5.3) which is higher compared to the EUV conversion efficiency achieved at 10^{-4} mbar argon ambient and discharge voltage of 24 kV. Thus, the addition of argon gas does not enhance the EUV energy production successfully in a metallic capillary discharge.

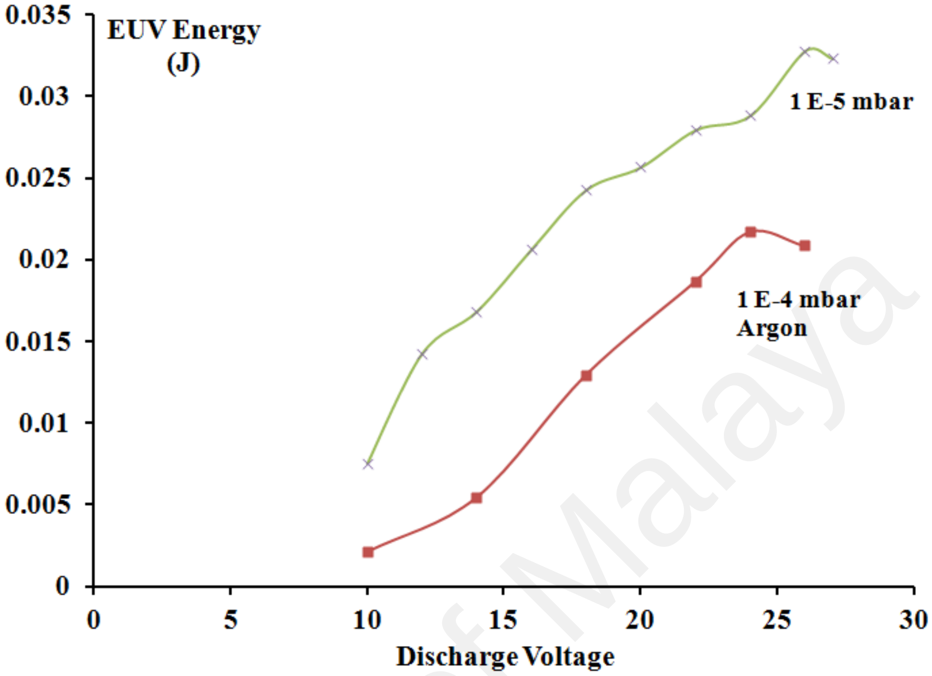

Figure 5.26: EUV energy production for stainless steel capillary plasma at optimum operating pressure in air ambient and Argon ambient respectively which is at 10^{-5} mbar air ambient and at 10^{-4} mbar argon ambient at the discharge voltage of 10 to 26 kV.

5.4.2 EUV Energy of Copper Capillary Plasma

Copper anode is used in order to produce a copper capillary plasma for the purpose of EUV enhancement. Since it is determined that the optimum pressure of our metallic capillary discharge for EUV production is 10^{-5} mbar (base pressure), thus the operating pressure is maintained at 10^{-5} mbar for copper capillary discharge.

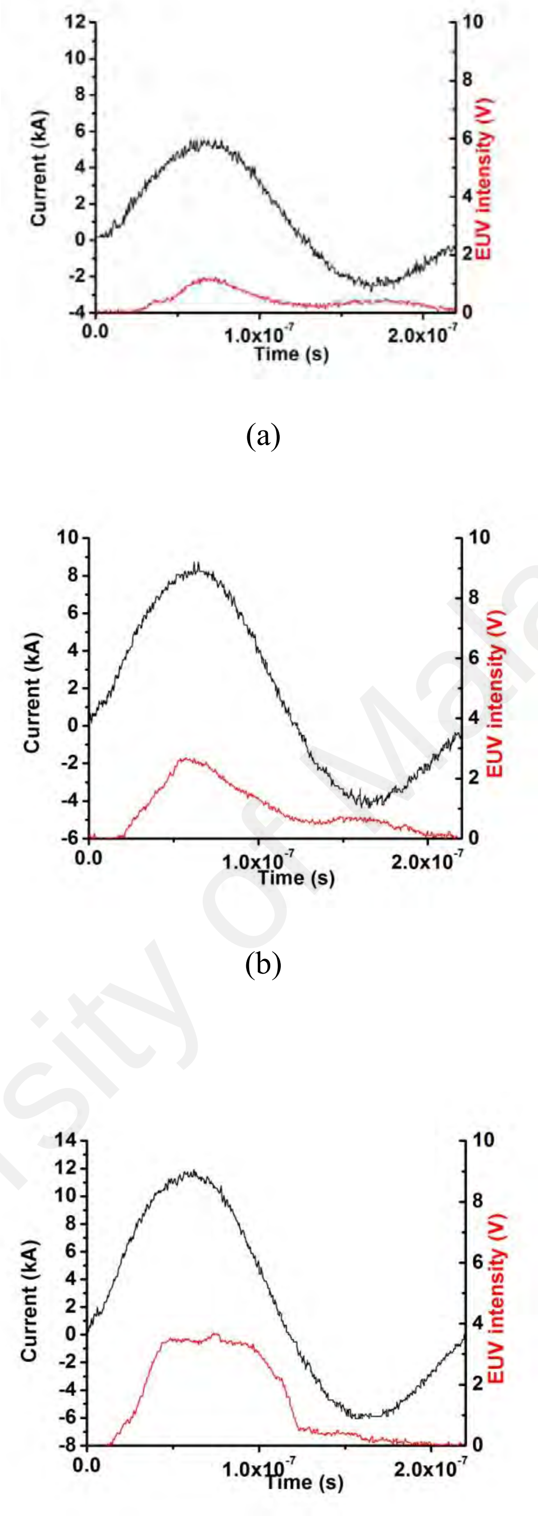

(a)

(b)

(c)

Figure 5.27: Typical current signal and the EUV emission obtained at the discharge voltage of (a) 10 kV (b) 18 kV (c) 24 kV and pressure of 10^{-5} mbar.

Figure 5.27 shows the current signal and EUV emission obtained at the discharge voltage of 10 kV, 18 kV and 24 kV of a copper plasma. The EUV intensity of copper plasma rises gradually with the current signal for the first 50 ns and drop gradually with the current signal in the 50 to 100 ns. The EUV emission starts to fade away at the reverse cycle of the current signal. Table 5.4 shows the EUV energy emitted from the copper plasma at the discharge voltage of 10 to 27 kV at the pressure of 10^{-5} mbar. It is observed that the EUV energy emitted increases with the increase of discharge voltage. The highest EUV energy achieved by our capillary discharge system, which is powered by capacitors with total capacitance of 21.6 nF is 38 mJ. The EUV energy produced by our capillary discharge system with upgraded with new capacitors of higher capacitance will be discussed in section 5.7.

Table 5.4: The EUV energy emitted from the copper plasma at the discharge voltage of 10 to 26 kV at the pressure of 10^{-5} mbar.

Discharge voltage (kV)	Input energy (J)	EUV energy (J)
10	1.08	9.90E-03
12	1.56	1.49E-02
14	2.12	1.94E-02
16	2.76	2.23E-02
18	3.50	2.58E-02
20	4.32	2.66E-02
22	5.23	2.83E-02
24	6.22	3.23E-02
26	7.30	3.60E-02
27	7.87	3.80E-02

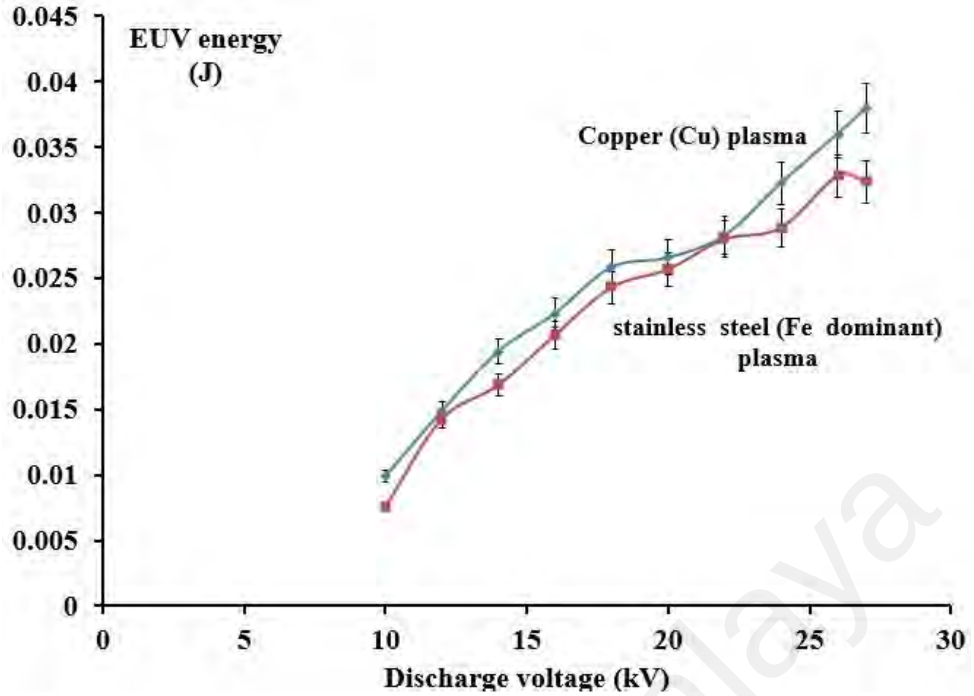

Figure 5.28: EUV energy of the copper and stainless steel capillary plasma at the discharge voltage of 10 to 27 kV and operating pressure of 10^{-5} mbar.

Figure 5.28 shows the comparison of the EUV energy obtained from the copper and stainless plasmas respectively at discharge voltage 10 to 27 kV and 10^{-5} mbar. It is evident that the copper plasma produces higher EUV energy compared to stainless steel plasma. Thus, it is determined that using copper anode to produce copper plasma is able to enhance the EUV production for the similar discharge voltage or input energy and eventually increase the EUV energy conversion efficiency (see Figure 5.29). Spectral lines of the copper plasma in the EUV range of 11 to 18 nm is simulated and will be shown in section 5.6.

Table 5.5: Conversion efficiency (CE) of EUV energy of the copper capillary plasma with input energy of 1 to 8 J (corresponds to the discharge voltage of 10 to 27 kV) and operating pressure of 10^{-5} mbar.

Discharge Voltage (kV)	Input Energy (J)	Conversion efficiency (%)
10	1.08	0.92
12	1.56	0.96
14	2.12	0.92

16	2.76	0.81
18	3.50	0.74
20	4.32	0.62
22	5.23	0.54
24	6.22	0.52
26	7.30	0.49
27	7.87	0.48

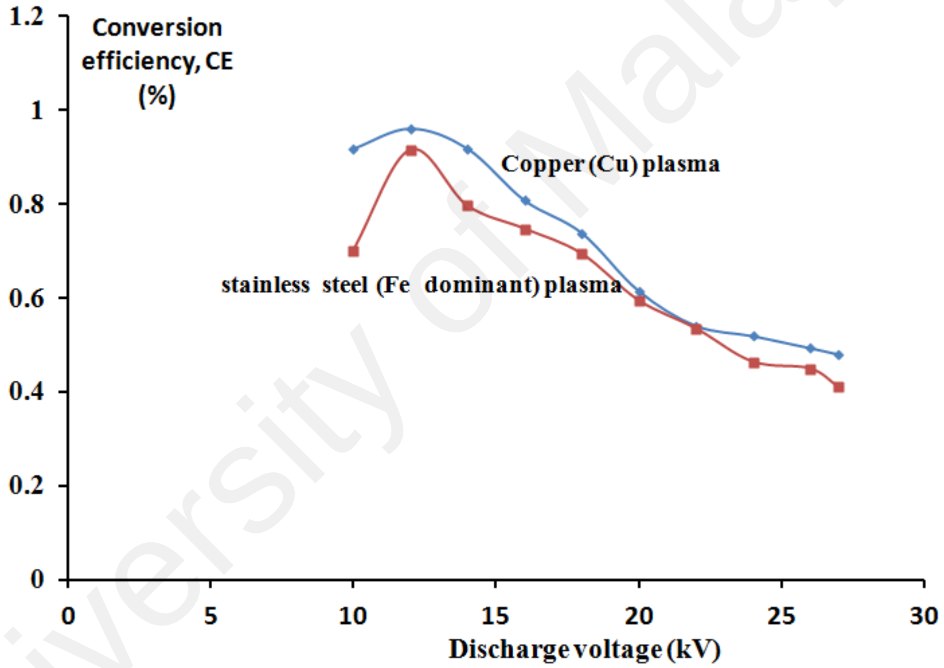

Figure 5.29: Conversion efficiency (CE) of EUV energy of the stainless steel and copper capillary plasmas with discharge voltage of 10 to 27 kV corresponding to the input energy of 1 to 8 J and operating pressure of 10^{-5} mbar.

5.5 Estimation of Electron Temperature of the Metallic Capillary Plasma

In a capacitor discharge system, the discharge circuit is represented by a LCR circuit. Thus, the discharge current of the capillary discharge can be simulated based on the LCR circuit equation given by (as stated in section 4.6):

$$V = IR + L(dI/dt) + \int (I/C)dt,$$

$$V = I(R_o+R_p) + (d/dt)\,(L_o + L_p)(I) + \int (I/C)dt,$$

where C represents the total capacitance of the capacitors that are used to power the capillary discharge system. L represents the total inductance of the capillary discharge which is contributed by of the circuit inductance (stray inductance), L_o and plasma inductance, L_p. Finally, R represents the total resistance of the capillary discharge which consists of the circuit resistance (stray resistance), R_o and plasma resistance, R_p.

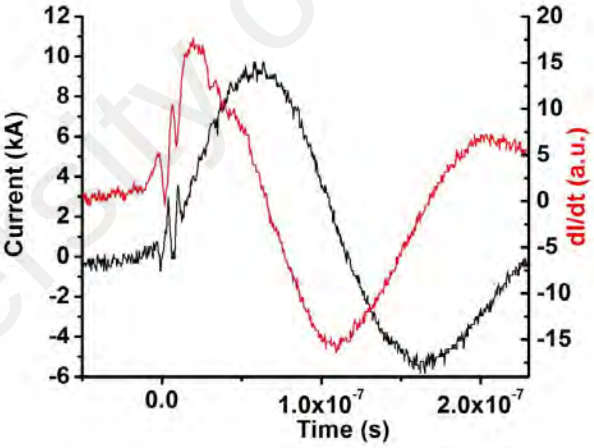

(a)

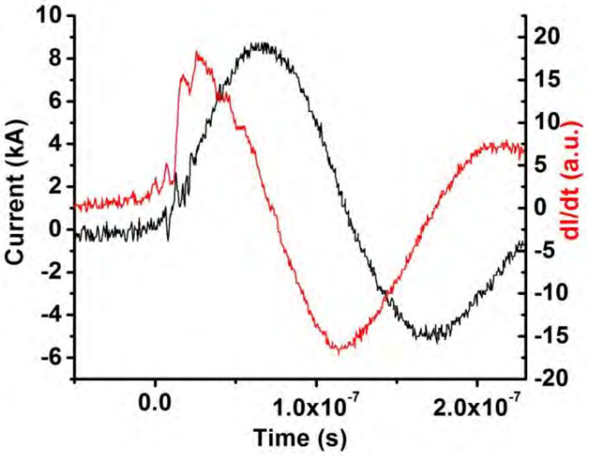

(b)

Figure 5.30: The Typical current and dI/dt waveforms at the discharge voltage of (a) 24 kV and (b) 26 kV.

Figure 5.30 exhibits the current signal and *dI/dt* signal at the discharge voltage of 24 kV and 26 kV. The dips that occur in both the current and *dI/dt* signals at the initiation of the discharge are due to electron bombardment on the anode that causes the bremsstrahlung process to occur and results in the emission of X-ray. It is observed that there is no significant dip in the current as well as *dI/dt* signals after the initiation of the discharge even at the current peak where *dI/dt* = 0 and this is true for all the current and *dI/dt* signals obtained at the discharge voltage of 10 to 26 kV. In our previous publication (Chan *et al*., 2009), we had shown by using time resolved imaging method that the plasma column formed during the discharge (at the peak current of around 9 kA) of the capillary discharge system used in the work reported here was a stable column and there was no evidence of pinching. Thus, it is believed that there is no significant compression or pinching of the plasma. This signifies that the plasma inductance is negligible and thus the capillary plasma formed can be modelled as a resistive load. By taking the capillary plasma as resistive load, the normalised form of the LCR circuit equation (refer to section 4.6 for details regarding this normalised equation) is given by:

$$d\iota/d\tau + \alpha\iota + \int \iota d\tau = 1$$

The discharge current waveform simulation is done by adjusting or varying the value of α, the damping factor, which is dependent on the resistance of the plasma as α is given by:

$$\alpha = R\ (C/L_o)^{1/2}$$

The time-varying plasma resistance will then be determined. With the determination of the plasma resistance, the electron temperature of the plasma is estimated based on the Spitzer expression, $\eta \sim T_e^{-3/2}$ (Spitzer, 1956), which predicted a decrease in the plasma resistance with an increase in the electron temperature. Similar method to estimate the electron temperature of the capillary discharge plasma based on the resistance had also been reported elsewhere (Ashkenazy *et al.*, 1991).

The current waveform of the stainless steel and copper capillary discharges at the discharge voltage of 12 kV, 24 kV and 26 kV and operating pressure of 10^{-5} mbar. The current simulation is only done for plasma obtained at the operating pressure of 10^{-5} mbar as the best EUV energy production is obtained at 10^{-5} mbar.

4.5.1 Stainless steel plasma

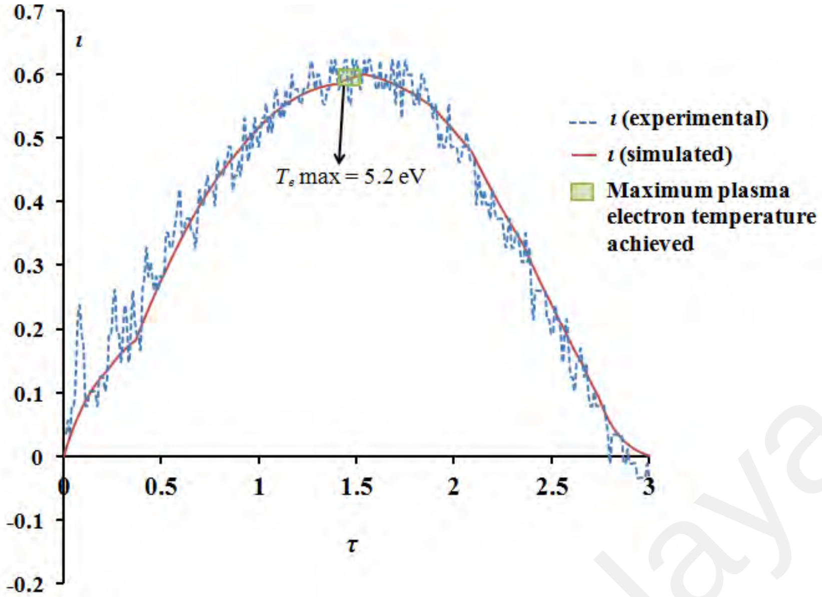

(a)

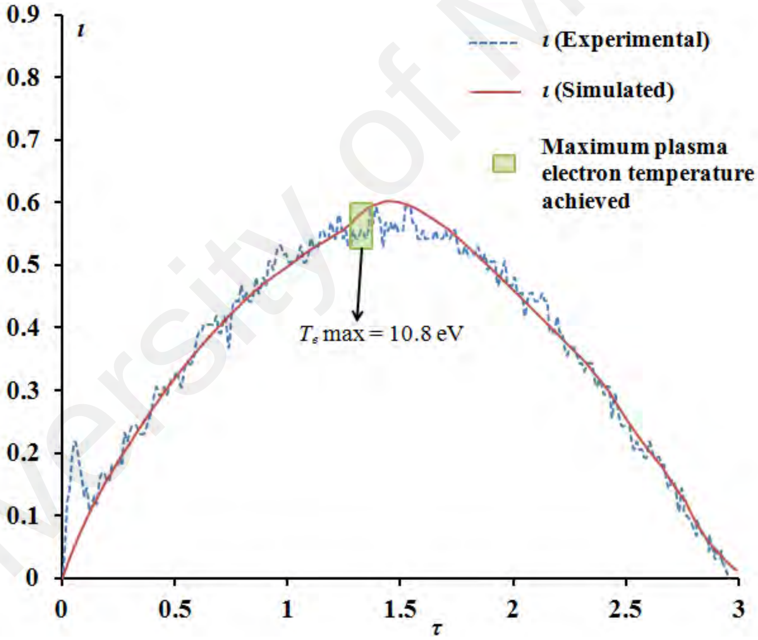

(b)

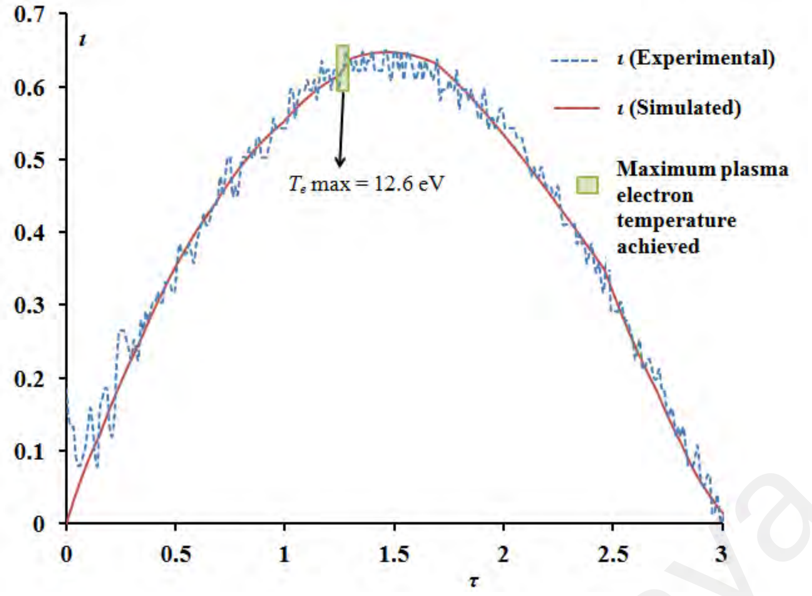

(c)

Figure 5.31: The fitting of the normalised simulated current waveform with the normalised experimental current waveform for discharge voltage of (a) 12 kV (b) 24 kV (c) 26 kV.

Figure 5.31 exhibit the fitting of the normalised simulated current waveform with the experimental current waveform for the discharge voltage of 12 kV, 24 kV and 26 kV for stainless steel plasma. Through the fitting of the current waveform, the resistance of the plasma is obtained and hence, the electron temperature of the plasma is computed. Table 5.6 shows the maximum electron temperature achieved for discharge voltage of 12 kV, 24 kV and 26 kV which occurs around the current peak of each discharge voltage. As expected, the plasma electron temperature is observed to increase at higher discharge voltage. At discharge voltage of 26 kV, the electron temperature is 12.6 eV, which is the appropriate temperature for EUV emission by the plasma.

Table 5.6: The maximum electron temperature of the stainless steel capillary discharge plasma achieved at the discharge voltage of 12 kV, 24 kV and 26 kV.

Discharge Voltage (kV)	Maximum plasma electron temperature achieved which is around the current peak (eV)
12	5.2
24	10.8
26	12.6

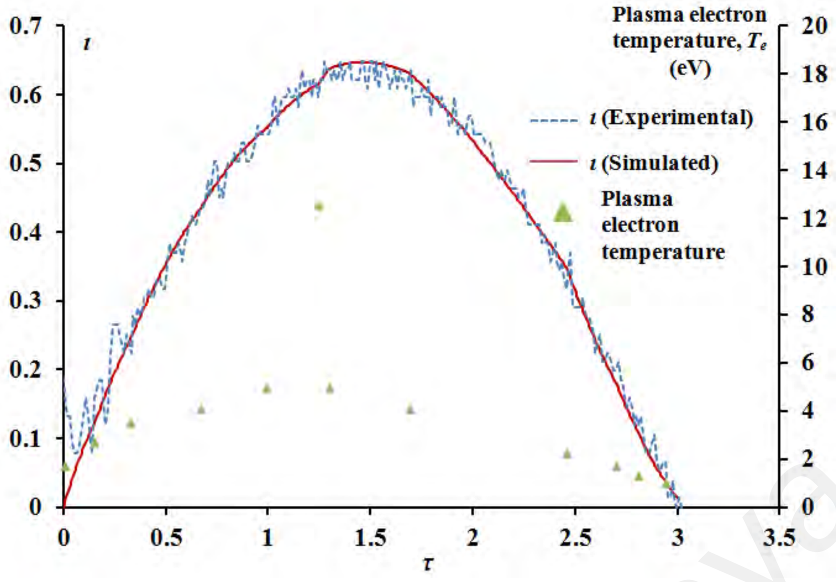

(a)

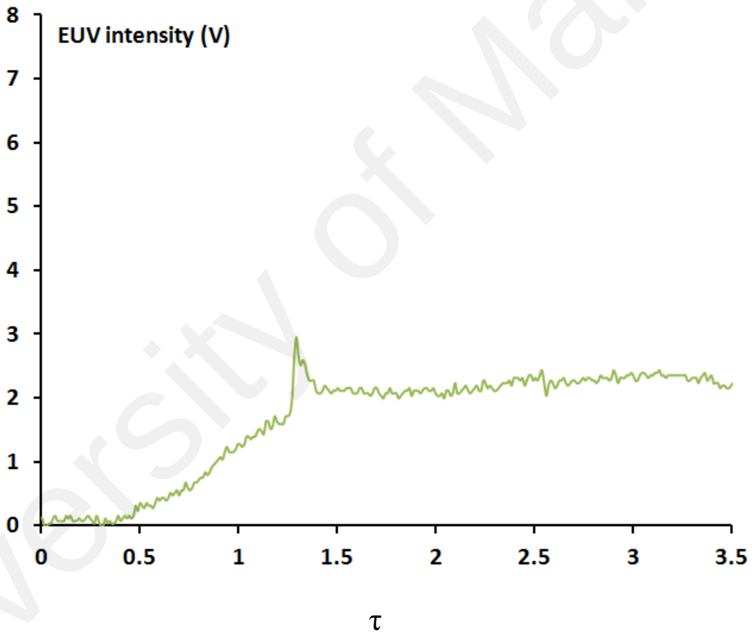

(b)

Figure 5.32: (a) Time-resolved plasma electron temperature and normalised current waveform obtained experimentally and also with simulation at the discharge voltage of 26 kV. (b) EUV emission obtained simultaneously with the current waveform.

Figure 5.32 (a) shows the time-resolved plasma electron temperature obtained at the discharge voltage of 26 kV. It is observed that as the discharge current increases (from τ = 0 to τ = 1), the electron temperature of the plasma increases gradually. This is followed by a sharp increase in the electron temperature as the current is reaching its maximum or peak magnitude. A sharp spike in the EUV emission [Figure 5.32 (b)] is also observed to correspond to the sharp increase of electron temperature of the plasma. Thus, it is evidenced that the sharp rise is due to fast occurring temperature changes. Further investigation on the relationship between the plasma electron temperature and EUV emission by simulation of the plasma emission using FLYCHK will be presented in section 5.6.

5.5.2 Copper Plasma

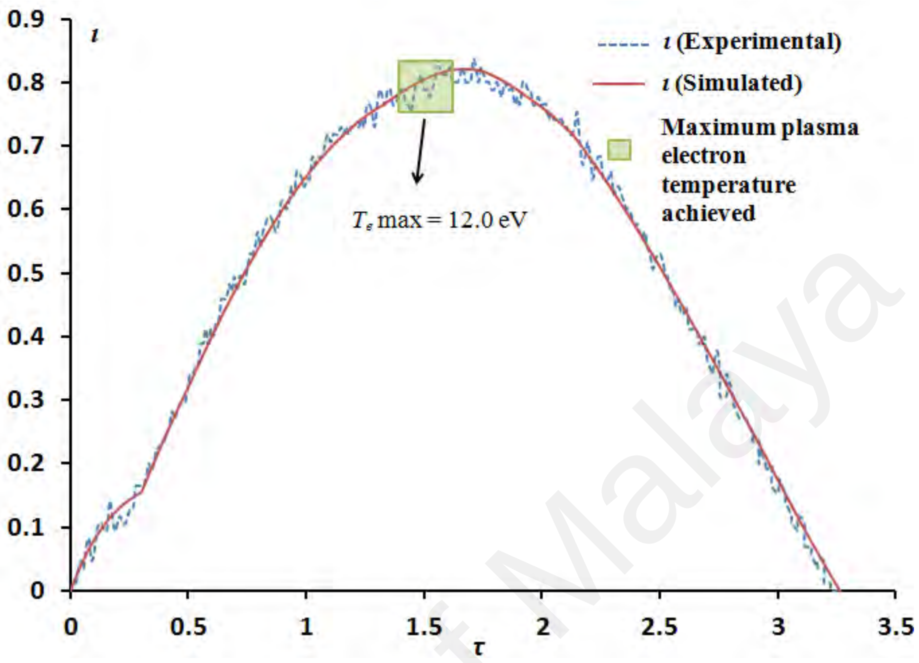

(a)

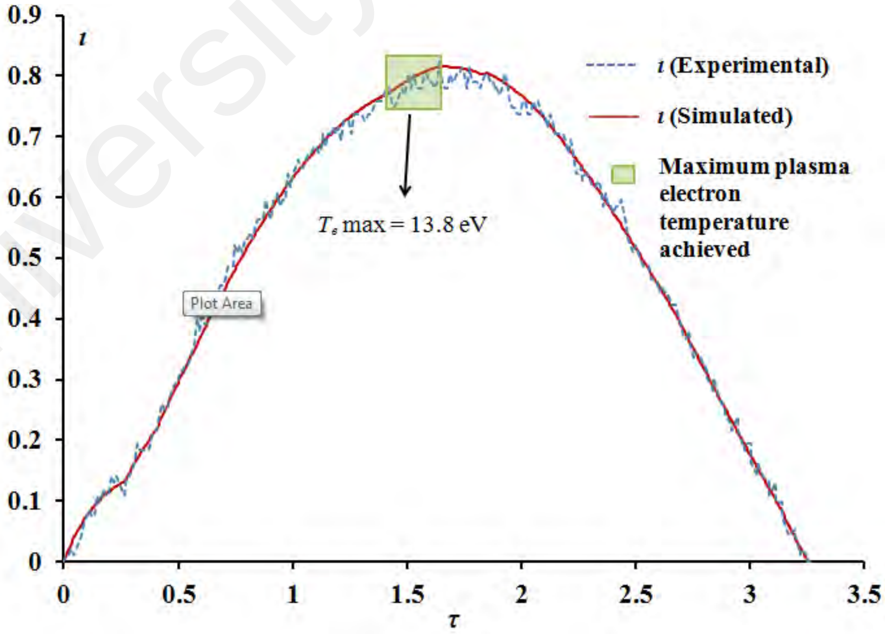

(b)

Figure 5.33: The fitting of the normalised simulated current waveform with the normalised experimental current waveform for discharge voltage of (a) 24 kV (b) 26 kV.

Discharge Voltage (kV)	Maximum plasma electron temperature achieved which is around the current peak (eV)
24	12.0
26	13.8

Table 5.7: The maximum plasma electron temperature achieved at the discharge voltage of 24 kV and 26 kV.

Figure 5.33 portrays the fitting of the normalised simulated current waveform with the experimental current waveform for the discharge voltage of 24 kV and 26 kV for copper plasma and Table 5.7. exhibits the plasma electron temperature achieved at the discharge voltage of 24 kV and 26 kV. The electron temperature for the discharge voltage of 24 kV and 26 kV are chosen to be simulated as the EUV emission produced at these discharge voltage are among the highest (Figure 5.28) and also to make comparison with the stainless steel plasma. As expected, the maximum plasma electron temperature achieved increases with the increase of discharge voltage as the peak current achieved (11.5 kA at 24 kV and 12.4 kA at 26 kV) increases with the discharge voltage.

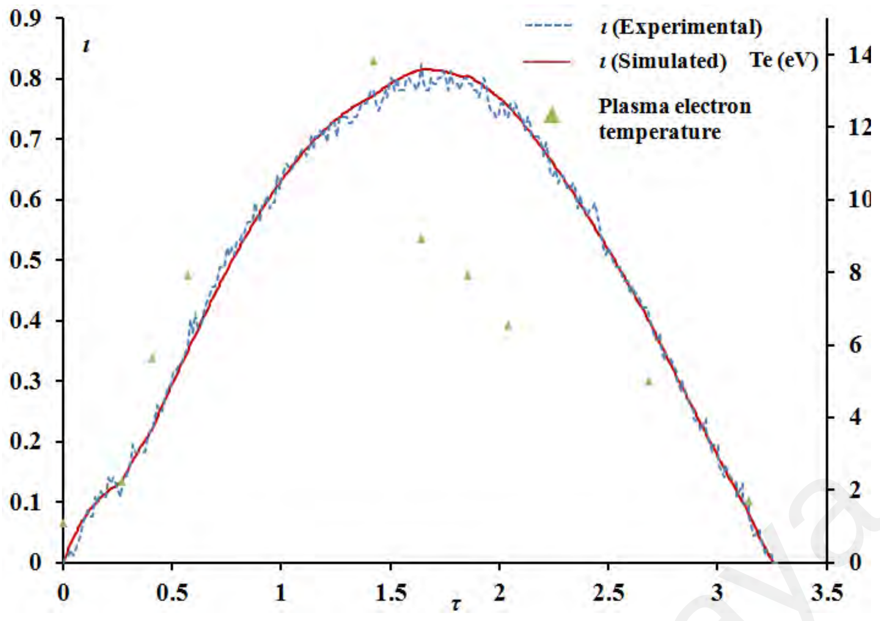

Figure 5.34: Time-resolved plasma electron temperature and normalised current waveforms obtained experimentally and by simulation at the discharge voltage of 26 kV.

Figure 5.34 shows the time-resolved copper plasma electron temperature obtained at the discharge voltage of 26 kV. It is observed that as the discharge current increases (from τ = 0 to τ = 1.5), the electron temperature of the plasma rises due to joule heating effect. After the current peak, the copper capillary plasma starts to cool down as the plasma electron temperature decreases gradually with the decrease of the discharge current.

5.5.3 Comparison of Electron Temperature between Stainless Steel Plasma and Copper Plasma

It is obtained that the copper plasma best electron temperature is higher than the stainless steel plasma best electron temperature at both discharge voltages of 24 kV and 26kV. At the 24 kV, the best temperature achieved by the copper plasma electron is 12.0 eV compared to 10.8 eV which is achieved by the stainless steel plasma electron. At 26 kV, the copper plasma best electron temperature achieved is 13.8 eV which 1.2

eV higher than the stainless steel plasma best electron temperature. This is evidenced from the discharge current obtained where the discharge current of the copper plasma is higher than stainless steel plasma (as an example, at the discharge voltage of 26 kV, the peak current of copper plasma is about 12 kA compared to stainless steel which is about 9 kA) and resulting the joule heating to be more effective in copper plasma.

5.6 Simulation of EUV properties of the Metallic Plasma using FLYCHK codes.

The EUV emission properties of the metallic capillary plasma such as the EUV spectra and ionic species population are simulated by using FLYCHK suite of codes (Chung *et al, 2005*). In order to apply FLYCHK code for simulation, a range of possible electron temperature and a range of electron density must be obtained. It was reported that the estimation of capillary plasma in general has an electron density of 10^{16}-10^{19} cm^{-3} (Tomasel *et al*, 1993; Moreno *et al*., 1999; Wyndham *et al*., 2002; Shuker *et al*., 2006; Klosner *et al*., 2000; Oh *et al*., 2010; Valenzuela *et al*., 2015). The capillary discharge system used in this project is similar to the system reported by Shuker *et al*, who had estimated the electron density of the order of 10^{17} cm^{-3}.

The EUV emission of the plasma can be originated from the line radiations, recombination radiation and bremsstrahlung radiation. Line radiation is emitted from the bound-bound transition while recombination radiation is emitted from the bound-free transitions. Bremsstrahlung radiation is emitted from the free-free transition.

5.6.1 Stainless Steel Capillary Plasma

The SXUVHS5 Si/Zr 100/200 nm photodiode that is used to detect the EUV emission has a spectral range from 11 nm to 18 nm, with peak sensitivity at the wavelength of 13.5 nm (Saboohi *et al., 2012*). Hence, the EUV emission obtained is contributed by predominantly photons at this wavelength range. According to the NIST database, the ionic species that emit in the range of wavelength of 11 to18 nm are Fe $^{6+}$, Fe^{7+}, Fe^{8+} Fe^{9+}, Fe^{10+}, Fe^{11+}, Fe^{14+}, Fe^{15+}, Fe^{18+}, Fe^{19+}, Fe^{20+}, Fe^{21+} and Fe^{22+} while the Fe ionic species that are prominent in emitting line radiation at 13.5 (92 eV) are Fe^{6+}, and Fe^{21+} (National Institute of Standard and Technology, 2013) as shown in Table 5.8. Thus, the relative ion populations curves for these two ionic species are computed by using FLYCHK codes (Chung *et al*., 2005), assuming NLTE model and electron density of $N_e \sim 10^{17}$ cm^{-3} (Shuker *et al,* 2006) for electron temperature, T_e in the range of 1 eV to 3000 eV as shown in Figure 5.35.

Table 5.8: The expected lines at 13.5 nm from Ferum ions Fe^{6+} and Fe^{21+} (National Institute of Standard and Technology, 2013).

Ion	Wavelength (nm)	Lower level Configuration (Conf.), Term, J	Upper level Configuration (Conf.), Term, J
Fe^{6+}	13.4940	$3p^6\ 3d^2\ {}^1G\ 4$	$3p^5({}^2P^0)3d^2({}^3F)4s({}^2F)\ {}^3G^0\ 3$
Fe^{6+}	13.5488	$3p^6\ 3d^2\ {}^1G\ 4$	$3p^5({}^2P^0)3d^2({}^3F)4s({}^2F)\ {}^3G^0\ 5$
Fe^{21+}	13.465	$2s^2\ 2p^2\ {}^4p\ 5/2$	$2p^3\ {}^4S^0\ 3/2$

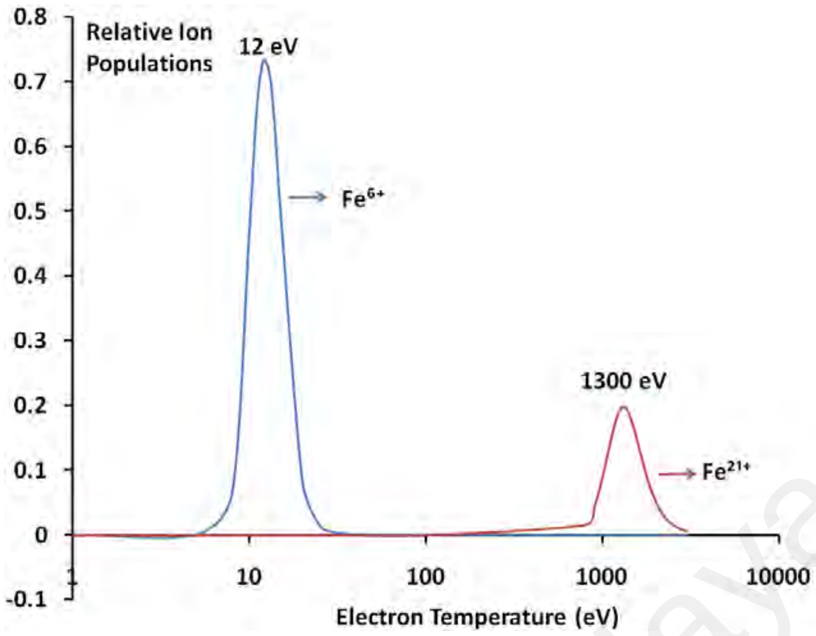

Figure 5.35: Relative ion population curves for Fe^{6+} (Fe VII) and Fe^{21+} (Fe XXII) for temperature in the range of 1 to 3000 eV.

Figure 5.35 shows the relative ion population curve for Fe^{6+} (Fe VII) which peaks at electron temperature of 12 eV and also ion population curve for Fe^{21+} (Fe XXII) which peaks at electron temperature of 1300 eV. As simulated in section of 5.5.1, the highest plasma electron temperature achieved at the discharge voltage of 12 kV, 24 kV and 26 kV are 5.2 eV, 10.8 eV and 12.6 eV respectively. Thus, the ionic specie that is produced in the range of electron temperature of above 100 eV, which is Fe^{21+}, will not be present in our stainless steel capillary plasma. Thus, it is believed that the ionic specie that emits at 13.5 in our stainless steel capillary plasma is the Fe^{6+}.

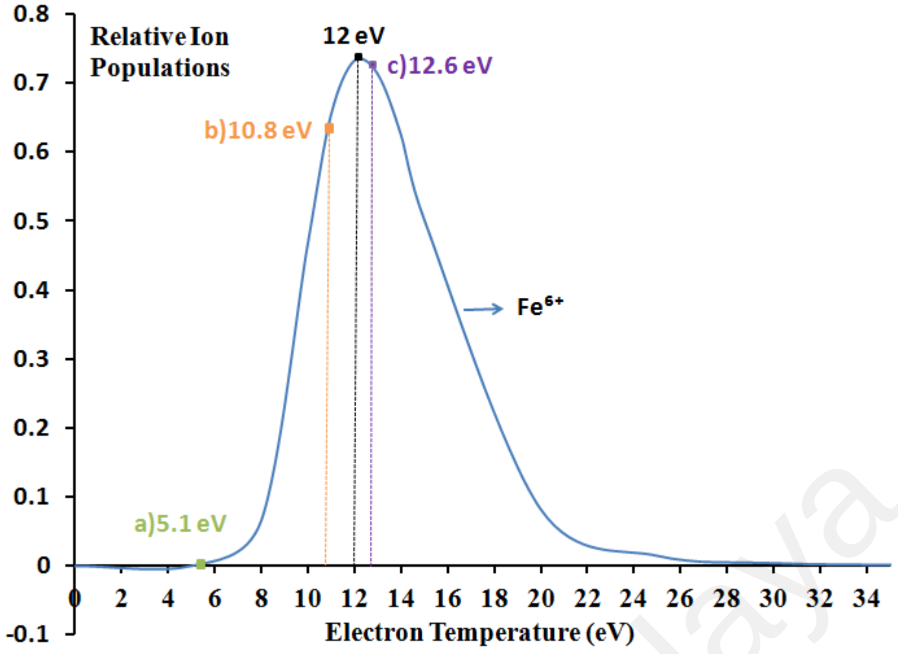

Figure 5.36: Relative ion population curve for Fe^{6+} (Fe VII) and the maximum electron temperature achieved at the discharge voltage of (a) 12 kV (b) 24 kV (c) 26 kV.

Figure 5.36 exhibits the relative ion population curves for Fe^{6+} (Fe VII) and the best electron temperature achieved at the discharge voltage of 12 kV, 24 kV and 26 kV. As mentioned earlier, the Fe^{6+} (with the transition stated in Table 5.8) is the ionic specie that emits at 13.5 nm and this particular ionic specie achieves its highest population at the plasma electron temperature at 12 eV.

At the discharge voltage of 12 kV which is equivalent to input energy of 1.56 J, the highest or the best plasma electron temperature achieved is 5.1 eV. It is observed in Figure 5.36 that the relative ion population of Fe^{6+} is very small (between 0 to 0.05) at 5.1 eV. Thus, it is believed that the input energy to the system at 12 kV discharge is not sufficient to heat up the plasma to the suitable condition for EUV emission in the range of 11 to18 nm. Figure 5.37 (a) shows the bound-bound emission of Fe in the range of 10 to 20 nm at the electron temperature of 5.1 eV which is within the range of detection of the EUV photodiode of 11 to 18 nm. The three main peaks in Figure 5.37 (a) are contributed by Fe VII (12.34 nm), Fe VII (15.72 nm) and Fe VII (17.55 nm).

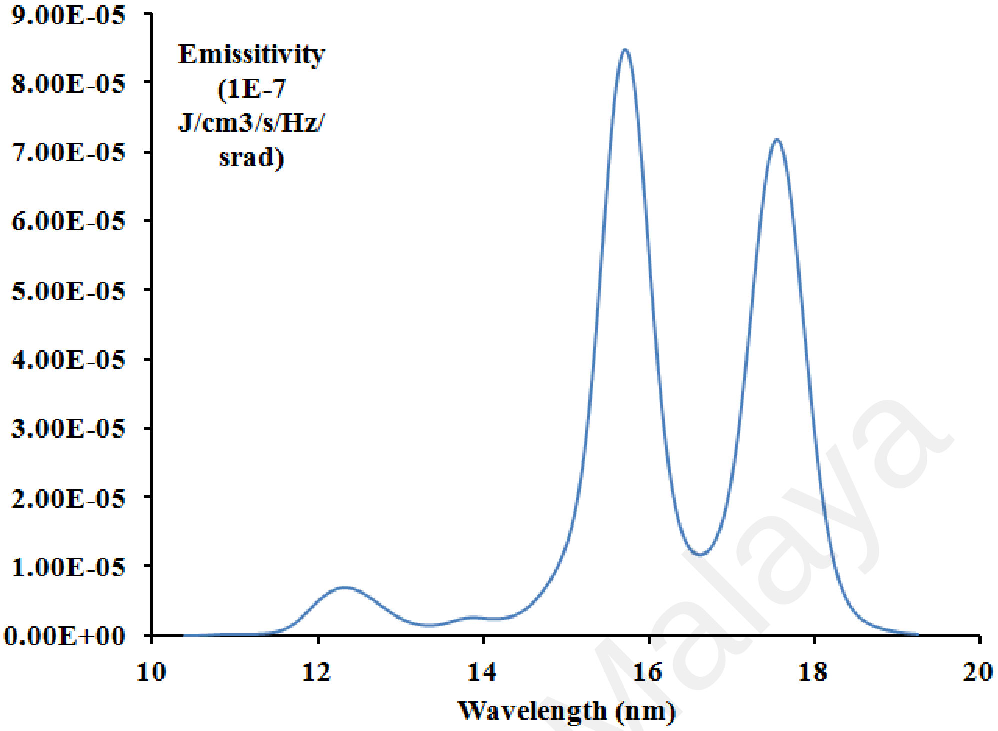

(a)

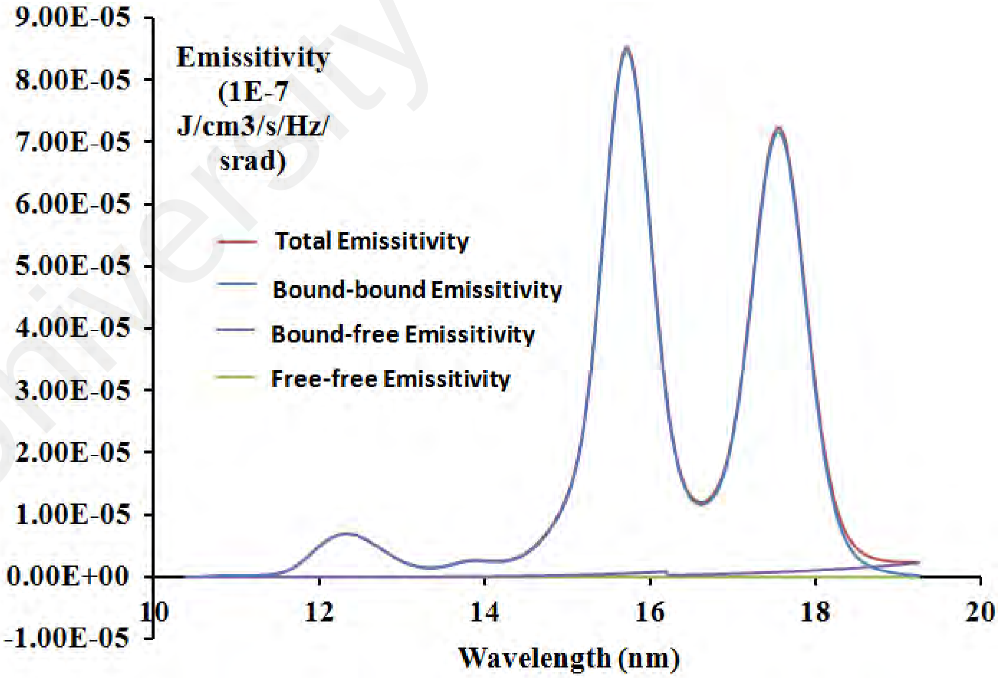

(b)

Figure 5.37: (a) Emissivity for bound-bound emission of Fe in the range of 10 to 20 nm at electron temperature of 5.1 eV. (b) EUV emission spectra of Ferum in the range of 10 to 20 nm at electron temperature of 5.1 eV.

Figure 5.37 (b) exhibits the EUV emission spectra of stainless steel plasma in the range of 10 to 20 nm at electron temperature of 5.1 eV. The total emissivity of EUV radiation peaks at the wavelength of 15.7 nm. It is observed that the emission at 15.7 nm is mainly contributed by photons emitted from bound-bound transition which is from the energy level of $3p^63d4f\ ^1F^0$ 3 to $3p^53d^2\ ^1G$ 4 (National Institute of Standard and Technology, 2013). At this electron temperature of 5.1 eV, the two peaks observed are in the range of wavelength longer than 13.5 nm (Fe VII-15.72 nm and Fe VII-17.55 nm) and the emissivity at the two peaks are 8.46 x 10^{-12} J/cm3/s/Hz/srad and 7.17 x 10^{-12} J/cm3/s/Hz/srad respectively. A small peak (Fe VII-12.34 nm) is observed at wavelength shorter than 13.5 nm with intensity of only 6.99 x 10^{-13} J/cm3/s/Hz/srad. The emissivity at 13.5 nm is only about 4.00 x 10^{-13} J/cm3/s/Hz/srad. Bound-free and Free-free emissions are insignificant in the range of wavelength of 11 to 18 nm. This due to the plasma electron temperature achieved that is not very high, which is in the range of 10-20 eV. Thus, the plasma emission is dominated by line radiation.

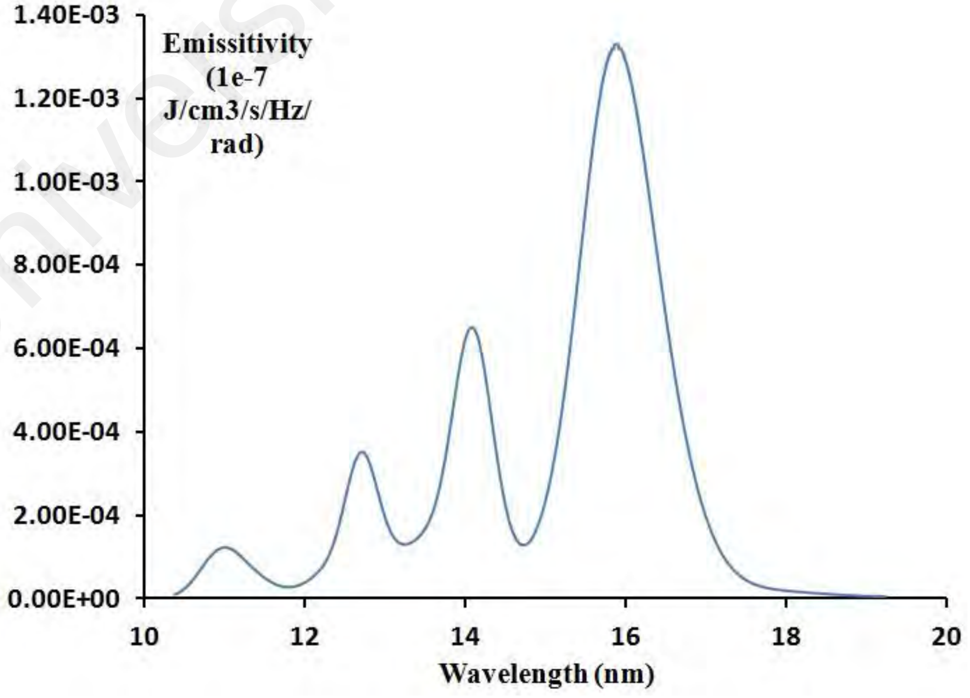

(a)

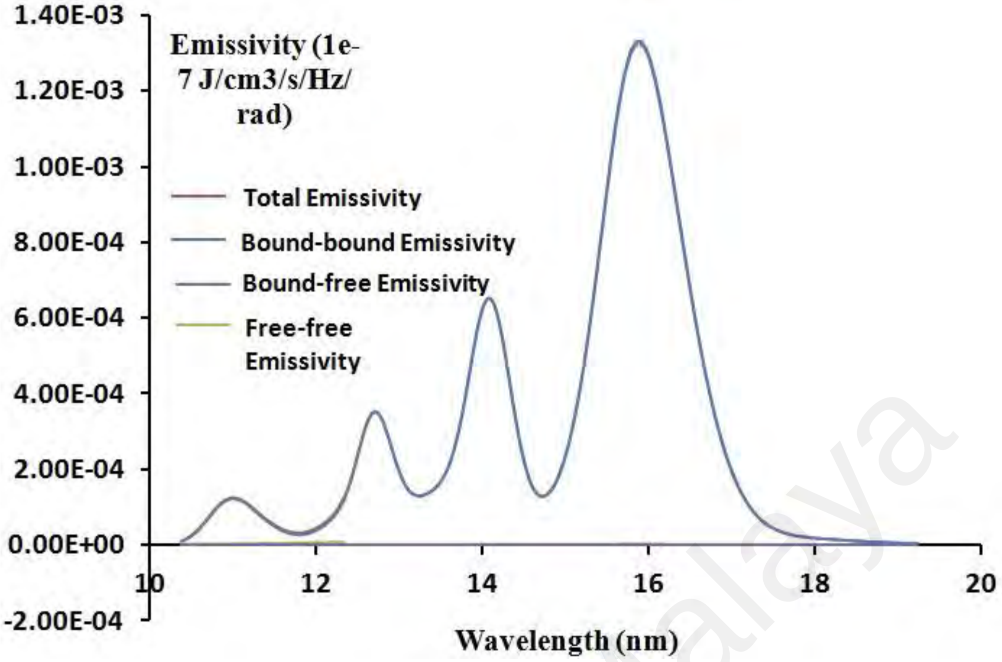

(b)

Figure 5.38: (a) Bound-bound emissivity of Fe in the range of 10 to 20 nm at electron temperature of 10.8 eV. (b) EUV emission spectra of Ferum in the range of 10-20 nm at electron temperature of 10.8 eV.

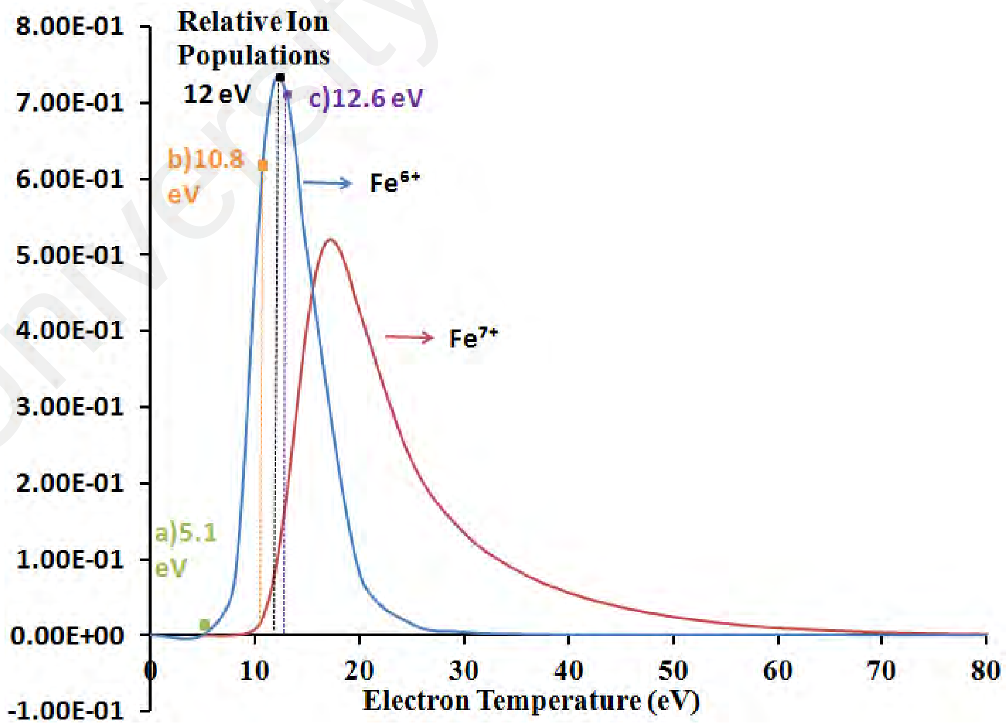

Figure 5.39: Relative ion population curves for Fe^{6+} (Fe VII) and Fe^{7+}(Fe VIII) and the maximum electron temperature achieved at discharge voltage of (a) 12 kV (b) 24 kV (c) 26 kV.

As the discharge voltage is increased to 24 kV, the highest plasma electron temperature achieved rises to 10.8 eV as a result of the increase of the input energy provided to the plasma. It is shown in Figure 5.36 that the relative ion populations at the electron temperature of 10.8 eV is close to the peak (maximum) of the Fe^{6+} ion population curve which occurs at the electron temperature of 12 eV. The relative ion population of Fe^{6+} at the electron temperature of 10.8 eV is approximately 0.65 which is higher compared to the relative ion population of Fe^{6+} at the electron temperature of 5.1 eV. Thus, as the plasma is heated up to a higher temperature in the suitable range, the plasma is able to emit in the EUV region of 11 to 18 nm more efficiently due to the increase of ion population of Fe^{6+} (the dominant ionic specie at electron temperature 10.8 eV) and Fe^{7+} (as shown in Figure 5.39) which contributes to the EUV emission at 11 to 18 nm. The EUV energy achieved at 24 kV is 28.8 mJ. Figure 5.42 (a) shows the bound-bound emissivity in the range of wavelengths of 10 to 20 nm at electron temperature of 10.8 eV. The peaks that are shown in Figure 5.38 (a) are Fe VII (11.01 nm), Fe VII (12.70 nm), Fe VII (14.06 nm) and Fe VII (15.87 nm). It is evidenced that the peaks occur at shorter wavelength (higher photon energy) compared to the peaks obtained at electron temperature of 5.1 eV in Figure 5.37 (a).

It is observed that the EUV emission at electron temperature of 10.8 eV is dominated by bound-bound transition as shown in the total emissivity curve in Figure 5.38 (b). The emissivity at 13.5 nm increase to 1.74×10^{-11} J/cm3/s/Hz/srad compared to 4.00×10^{-13} J/cm3/sHz/srad at the electron temperature of 5.1 eV. The intensity of the total EUV emissivity at the electron temperature of 10.8 eV is higher compared to the total EUV emissivity obtained at the electron temperature of 5.1 eV (as shown in Figure 5.42 in the end of this section). The peak of the total EUV emissivity achieved occurs at the wavelength of 15.87 nm with the intensity of 1.33×10^{-10} J/cm3/s/Hz/srad and it is originated from the transition of $3p^63d4f$ $1G^0$ 4 to $3p^63d^2$ ^1G 4 (National Institute of Standard and Technology, 2013). Thus, the intensity of the peak of the total EUV emissivity at the electron temperature 10.8 eV is higher compared to the peak of the total EUV emissivity at the electron temperature 5.1 eV. Bound-free and free-free emissivity is very low and is negligible especially at the range of wavelength of 12.5-18 nm.

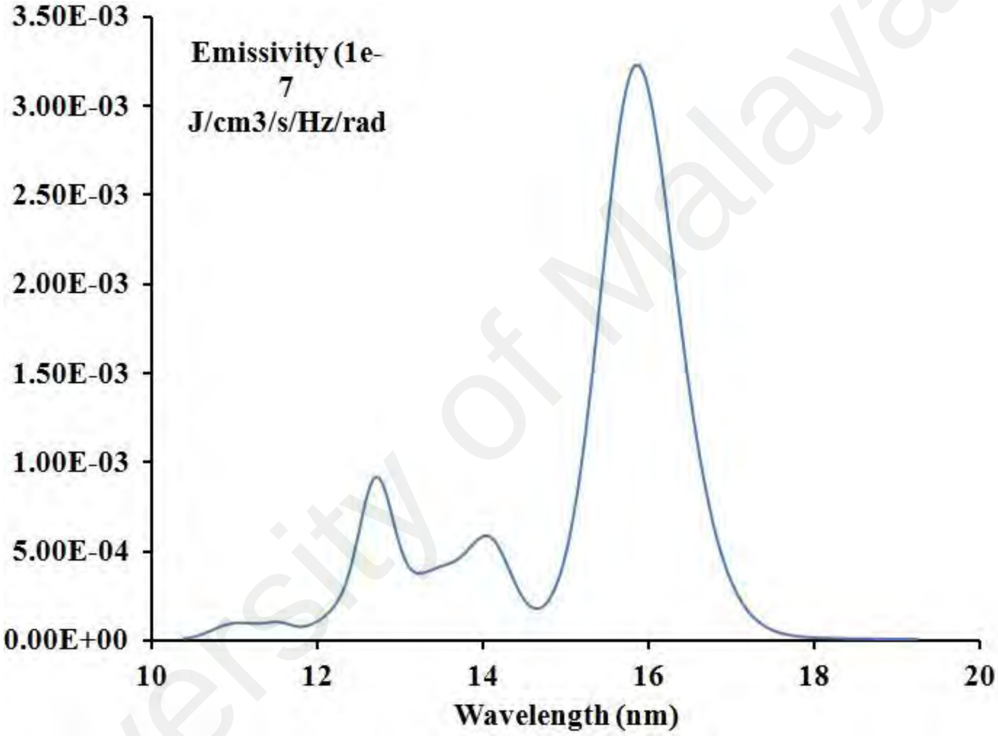

(a)

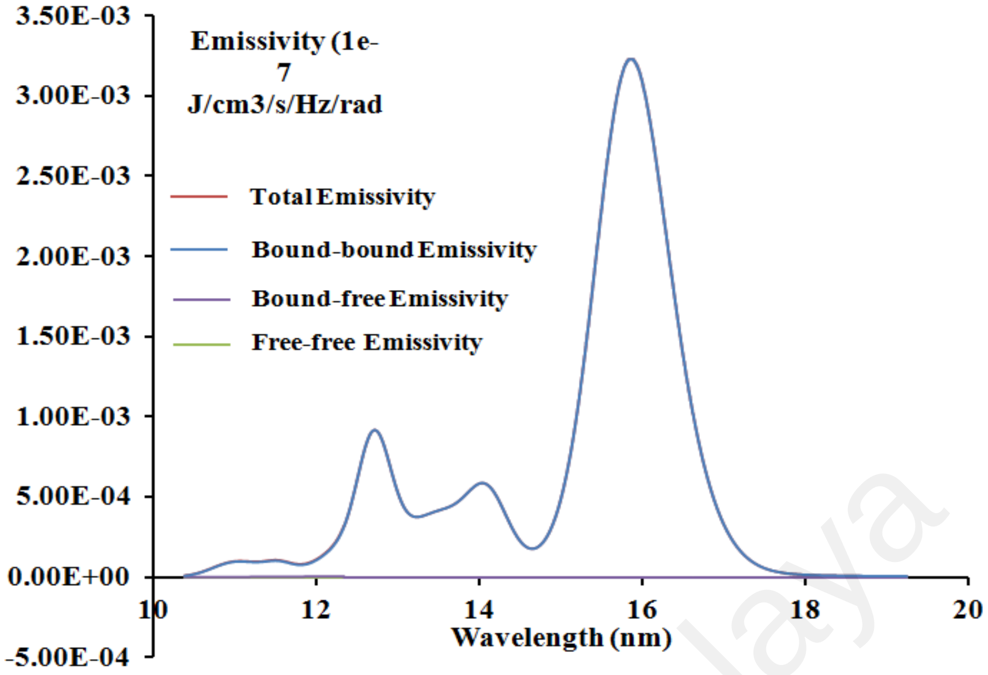

(b)

Figure 5.40: (a) Emissivity (bound-bound) of Ferum in the range of 10 to 20 nm at the electron temperature of 12.6 eV. (b) EUV emission spectra of Ferum in the range of 10 to 20 nm at the electron temperature of 12.6 eV (the red line-total emissivity, is underneath the blue line-bound-bound emissivity).

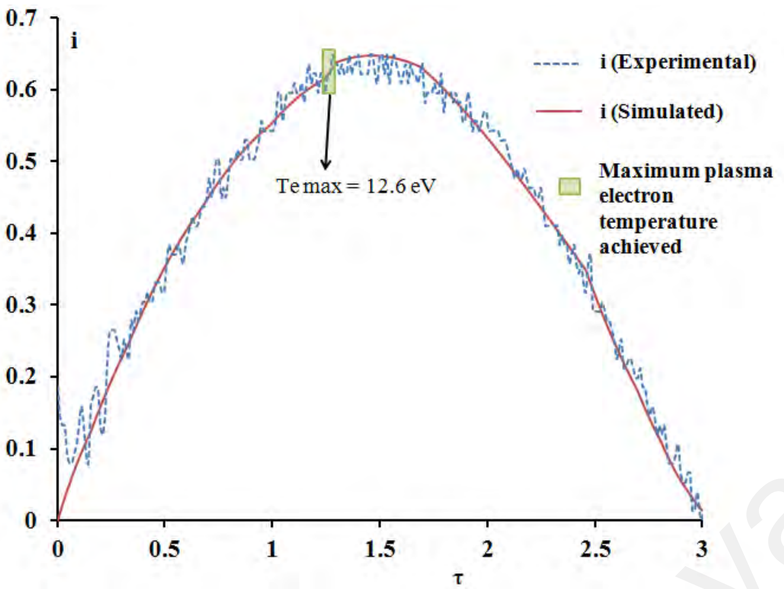

(a)

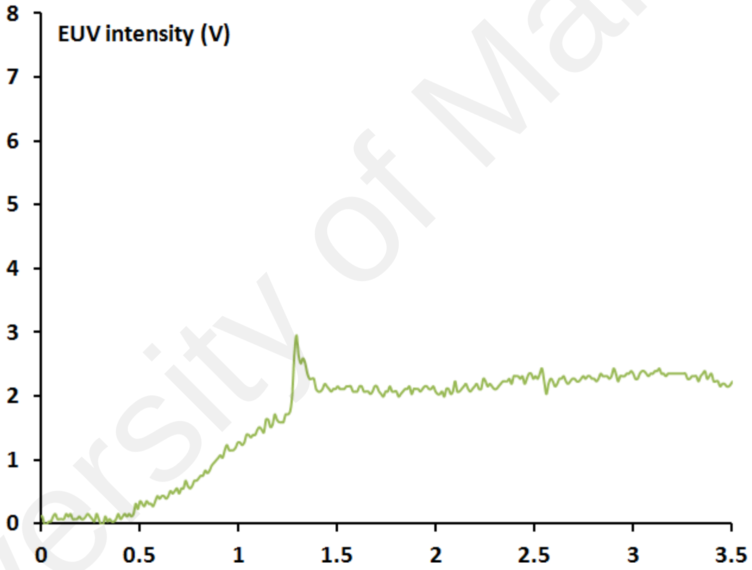

(b)

Figure 5.41: (a) The best plasma electron temperature achieved and normalised current waveform obtained experimentally and also with simulation at the discharge voltage of 26 kV. (b) EUV emission obtained at the discharge voltage of 26 kV.

At the discharge voltage of 26 kV, the best electron temperature achieved is 12.6 eV. It is evidenced in Figure 5.36 that the relative ion populations at the electron temperature of 12.6 eV is very close to the electron temperature at the peak (maximum) of the Fe^{6+} ion population curve. It is also interesting to note that the maximum electron temperature is observed to correspond to the sharp rise in the EUV intensity obtained experimentally as shown in Figure 5.41. With the combination of the analysis of Figure 5.36 and Figure 5.40 and also the known fact that the photodiode has the maximum sensitivity at 13.5 nm (Figure 4.9), a more concrete explanation of the sharp rise in the EUV signal is obtained. The sharp rise is due to the increase of ion population of Fe^{6+} that emits at the wavelength of 13.5 nm.

As noticed in Figure 5.36 and Figure 5.39, the relative ion population of Fe^{6+} at the electron temperature of 12.6 eV is approximately 0.73 which is higher compared to the relative ion population of Fe^{6+} at the electron temperature of 10.8 eV while the relative ion population of Fe^{7+} at electron temperature of 12.6 eV increase to 0.15 compared to 0.03 at the electron temperature of 5.1 eV. The increase of these ion population will contribute to the EUV emission of the plasma and this is evidenced from the EUV energy of 32.8 mJ obtained experimentally at the discharge voltage of 26 kV (maximum electron temperature achieved is 12.6 eV) as compared to 28.8 mJ at discharge voltage of 24 kV. Figure 5.40(a) shows the EUV bound-bound emissivity in the range of wavelengths of 10 to 20 nm at the electron temperature of 12.6 eV. The peaks that are shown in the bound-bound emissivity are Fe VII (12.70 nm), Fe VII (14.06 nm) and Fe VII (15.84 nm). It is observed that the EUV emission at the electron temperature of 12.6 eV is dominated by bound-bound transition as portrayed in the total emissivity curve in Figure 5.40 (b). The total emissivity at 13.5 nm increases to 4.18 x 10^{-11} J/cm3/s/Hz/srad compared to 1.74 x 10^{-11} J/cm3/s/Hz/srad at the electron temperature of 10.8 eV. The total EUV emissivity at the electron temperature of 12.6 eV is higher compared to the total EUV emissivity obtained at the electron temperature of 10.8 eV (as show in Figure 5.42 below). The peak of the total EUV emissivity achieved occurs at the wavelength of 15.84 nm with the intensity of 3.23 x 10^{-10} J/cm3/s/Hz/srad and it is originated from the transition of $3p^6 3d4f$ $1G^0$ 4 to $3p^6 3d^2$ ^1G 4

(National Institute of Standard and Technology, 2013) which is the same peak shown as 15.87 nm in Figure 5.38 (a). Thus, the intensity of the peak of the total EUV emissivity at the electron temperature of 12.6 eV is higher compared to the peak of the total EUV emissivity at the electron temperature of 10.8 eV. Bound-free and free-free emissivity are negligible.

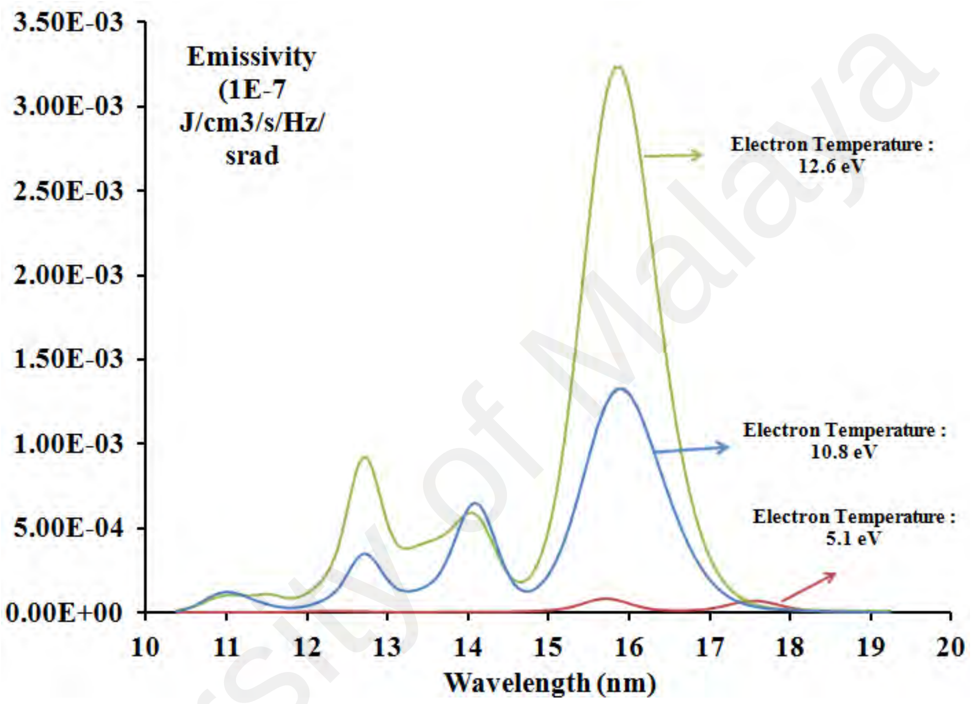

Figure 5.42: Total Emissivity of the EUV emission in the range of wavelength of 10 to 20 nm at the electron temperature of 5.1 eV, 10.8 eV and 12.6 eV.

5.6.2 Copper Capillary Plasma

It is calculated in section 5.4 that the EUV energy achieved by the copper plasma is higher than the iron (stainless steel) plasma. Thus, in this section, the EUV spectra for copper plasma is presented and comparison is made with the EUV spectra of stainless steel plasma.

According to the NIST database, the Cu ionic species that emit in the range of wavelength of 11 to 18 nm are Cu^{9+}, Cu^{10+}, Cu^{11+}, Cu^{12+}, Cu^{13+}, Cu^{14+}, Cu^{15+}, Cu^{16+}, Cu^{17+}, Cu^{18+}, Cu^{19+}, Cu^{21+}, Cu^{22+}, Cu^{23+}, Cu^{24+}, Cu^{25+}, Cu^{26+}, Cu^{27+} while the Cu ionic species that are prominent in emitting line radiation at 13.5 (92 eV) is Cu^{10+} (National Institute of Standard and Technology, 2013) as shown in Table 5.9.

Table 5.9: The expected lines at 13.5 nm from Cu ions Cu^{10+} (National Institute of Standard and Technology, 2013).

	Wavelength (nm)	Lower level Conf., Term, J	Upper level Conf., Term, J
Cu^{10+}	13.4914	$3p^6\ 3d^2\ {}^2D\ {}^3/_2$	$3p^5\ ({}^2P^0)\ 3d^2\ ({}^3F)\ {}^2D^0\ {}^3/_2$
Cu^{10+}	13.4989	$3p^6\ 3d^2\ {}^2D\ {}^3/_2$	$3p^5\ ({}^2P^0)\ 3d^2\ ({}^3F)\ {}^2D^0\ {}^5/_2$
Cu^{10+}	13.5286	$3p^6\ 3d^2\ {}^2D\ {}^3/_2$	$3p^5\ ({}^2P^0)\ 3d^2\ ({}^3P)\ {}^2P^0\ {}^3/_2$

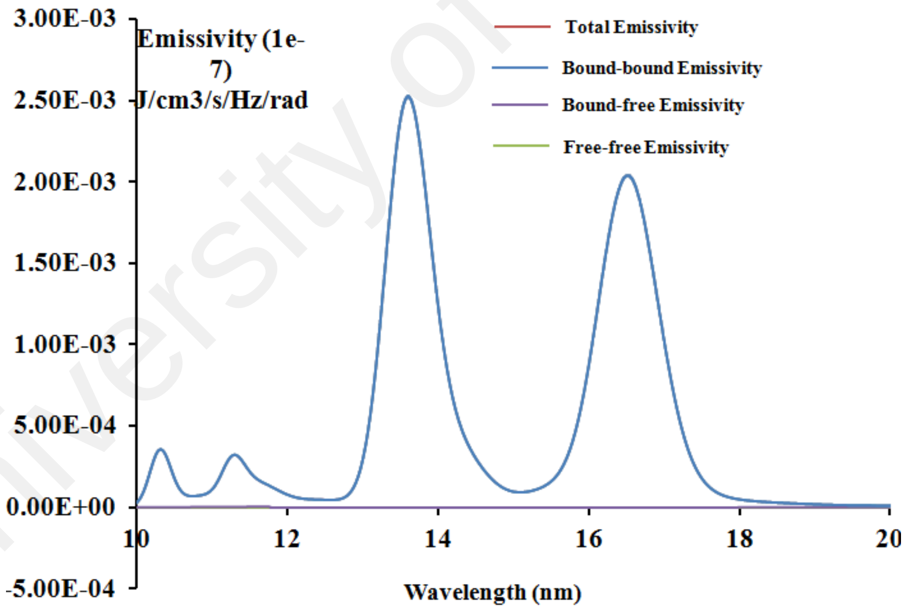

Figure 5.43: EUV emission spectra of Cuprum in the range of 10 to 20 nm at the electron temperature of 12.0 eV (the red line-total emissivity, is underneath the blue line-bound-bound emissivity).

At the discharge voltage of 24 kV, the highest or the best plasma electron temperature achieved is 12 eV. The EUV energy achieved at 24 kV is 28.8 mJ. It is observed that the EUV emission of copper plasma at the electron temperature of 12.0

eV is dominated by bound-bound transition as portrayed in the total emissivity curve in Figure 5.43. The total emissivity at 13.5 nm is 2.4 x 10^{-10} J/cm3/s/Hz/srad. The peak of the total EUV emissivity achieved occurs at the wavelength of 13.60 nm with the intensity of 2.53 x 10^{-10} J/cm3/s/Hz/srad. Bound-free and free-free emissivity is very low and is insignificant in this range of wavelength.

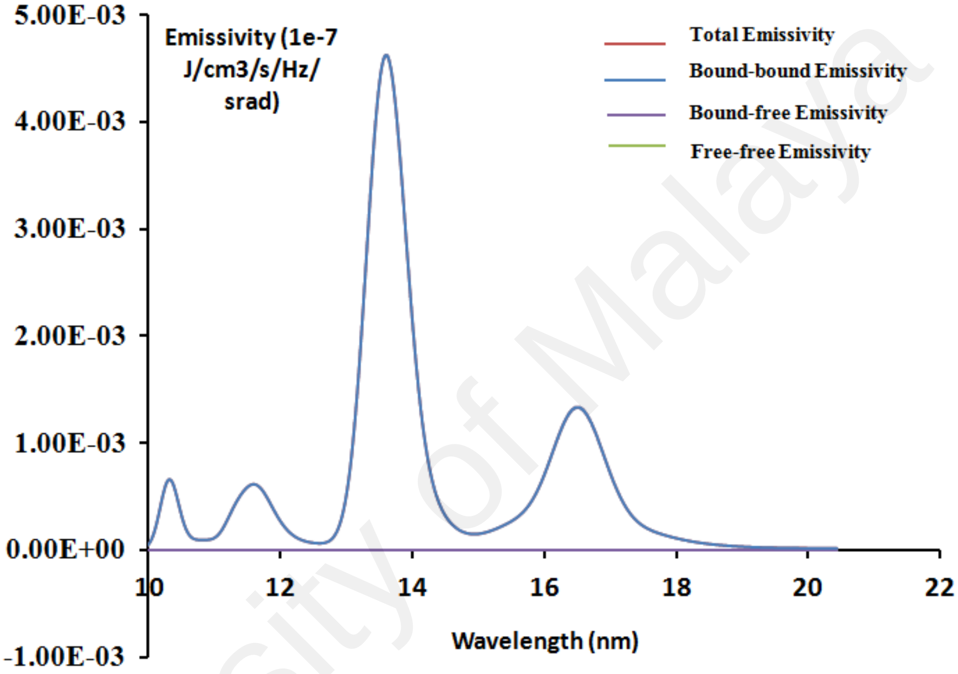

Figure 5.44: EUV emission spectra of Cu in the range of 10 to 20 nm at the electron temperature of 13.8 eV (the red line-total emissivity, is underneath the blue line-bound-bound emissivity).

As the discharge voltage is increased to 26 kV, providing an input energy of 7.3 J, the maximum electron temperature achieved is 13.8 eV. Figure 5.44 shows the EUV emission spectra of copper in the range of wavelengths of 10 to 20 nm at the electron temperature of 13.8 eV. It is observed that the EUV emission at the electron temperature of 13.8 eV is dominated by bound-bound transition as portrayed by the total emissivity curve in Figure 5.44. The total emissivity at 13.5 nm increases at the electron temperature of 13.8 eV to 4.39 x 10^{-10} J/cm3/s/Hz/srad compared to 2.4 x 10^{-10} J/cm3/s/Hz/srad at the electron temperature of 12.0 eV (as show in Figure 5.45). The peak of the total EUV emissivity achieved at the electron temperature of 13.8 eV occurs at the wavelength of 13.59 nm with the intensity of 4.60 x 10^{-10} J/cm3/s/Hz/srad. Bound-free and free-free emissivity are negligible.

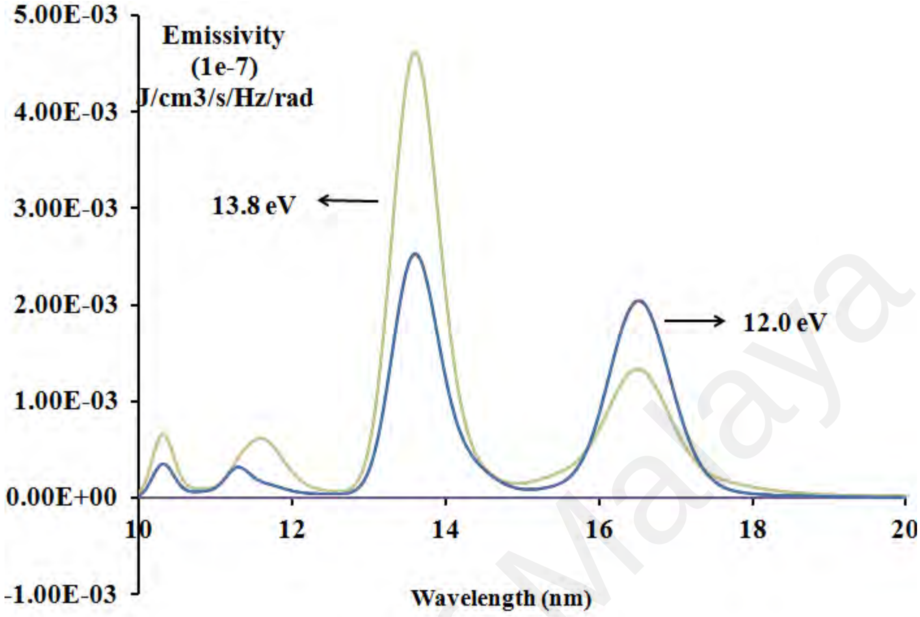

Figure 5.45: Total Emissivity of the EUV radiation in the range of wavelength of 10 to 20 nm at the electron temperature of 12.0 eV and 13.8 eV.

5.6.3 Comparison of EUV Emission Spectra of Stainless Steel (Fe) Plasma and Copper Plasma

It is evidenced that Cu achieves higher emissivity at the wavelength near 13.5 nm compared to Fe. At the discharge voltage of 26 kV, the EUV emissivity at 13.5 nm for copper plasma is 4.39 x 10^{-10} J/cm3/s/Hz/srad is higher compared to stainless steel plasma which is 4.18 x 10^{-11} J/cm3/s/Hz/srad. This is aligned with the EUV energy experimental result which is obtained using the SXUVHS5 Si/Zr 100/200 nm photodiode that has peak sensitivity at 13.5 nm as shown in Figure 4.9. The EUV energy obtained experimentally as shown in Figure 5.28 shows that Cu plasma is a better EUV energy emitter compared to Fe, particularly for emission at the wavelength of 13.5 nm.

5.7 EUV Enhancement by using capacitors with a higher capacitance to power the capillary discharge

It is observed that our capillary discharge system which is powered by capacitors with total capacitance of 21.6 nF, the EUV energy produced by the copper plasma increases with the increased of discharge voltage or input energy as observed in Table 5.4 and Figure 5.28. Unfortunately, the charging voltage limit for the capacitors of the previous system is 30 kV. Thus, capacitors of higher capacitance with total capacitance of 1.2 μF is purchased to power the capillary system in order to provide higher input energy to the system for EUV production.

5.7.1 EUV energy of the capillary discharge powered with capacitors of 1.2 µF and comparison with 21.6 nF

In our experiments, the capacitors are charged up from 4-8 kV (higher than 8 kV, the capillary will crack), providing an input energy of 9.6-38.4 J. The EUV energy obtained is shown below.

Table 5.10: EUV energy emitted from the copper plasma at the discharge voltage of 4-8 kV at the pressure of 10^{-5} mbar (new system with the total capacitance of 1.2 µF).

Discharge voltage (kV)	Input Energy (J)	EUV energy (J)
4.0	9.6	6.82E-02
4.5	12.15	6.64E-02
5.0	15	6.67E-02
5.5	18.15	6.99E-02
6.0	21.6	7.35E-02
6.5	25.35	7.51E-02
7.0	29.4	7.45E-02
7.5	33.75	8.07E-02
8.0	38.4	8.35E-02

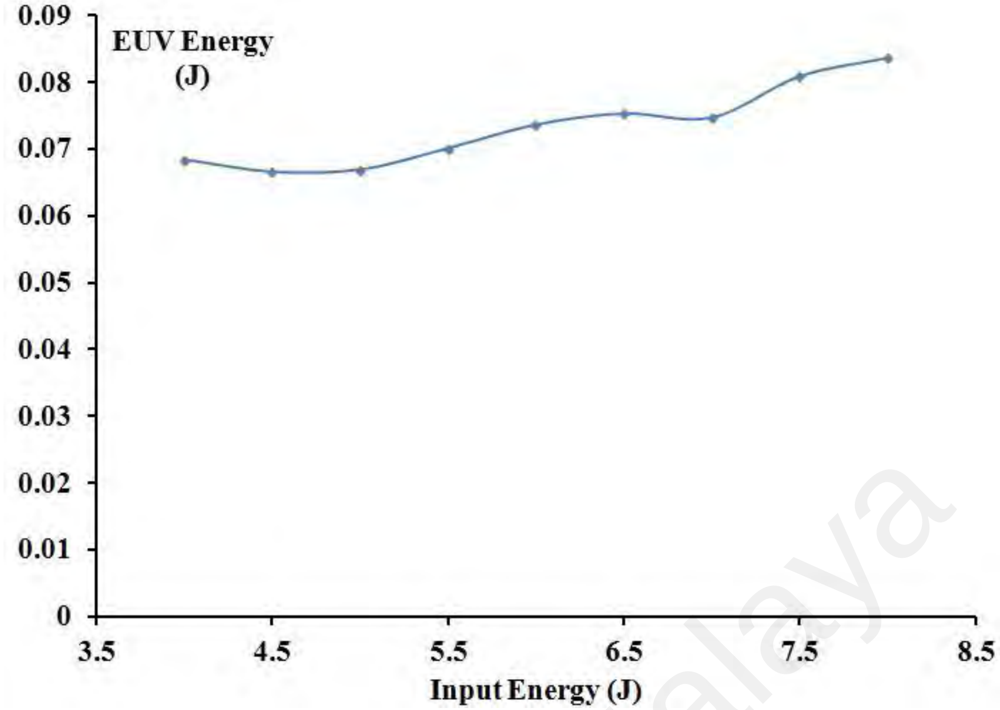

Figure 5.46: EUV energy of the copper capillary plasma at the discharge voltage of 4-8 kV at the operating pressure of 10^{-5} mbar that is powered with capacitors with total capacitance of 1.2 µF.

Table 5.11: Conversion efficiency of EUV energy at the input energy of 10-38 J and operating pressure of 10^{-5} mbar (powered with capacitors with total capacitance of 1.2 µF).

Discharge voltage (kV)	Input Energy (J)	Conversion efficiency (%)
4.0	9.6	0.71
4.5	12.15	0.55
5.0	15	0.45
5.5	18.15	0.39
6.0	21.6	0.34
6.5	25.35	0.30
7.0	29.4	0.25
7.5	33.75	0.24
8.0	38.4	0.22

As observed in Table 5.10 and Figure 5.46, the EUV energy produced by the capillary plasma increases gradually with the discharge voltage or input energy. The highest EUV energy achieved by our capillary discharge system when it is powered with the capacitors of total capacitance of 1.2 µF is 83.5 mJ with the input energy of

38.4 J (discharge voltage of 8 kV). The highest conversion efficiency achieved is 0.71% which occurs at the discharge voltage of 4 kV.

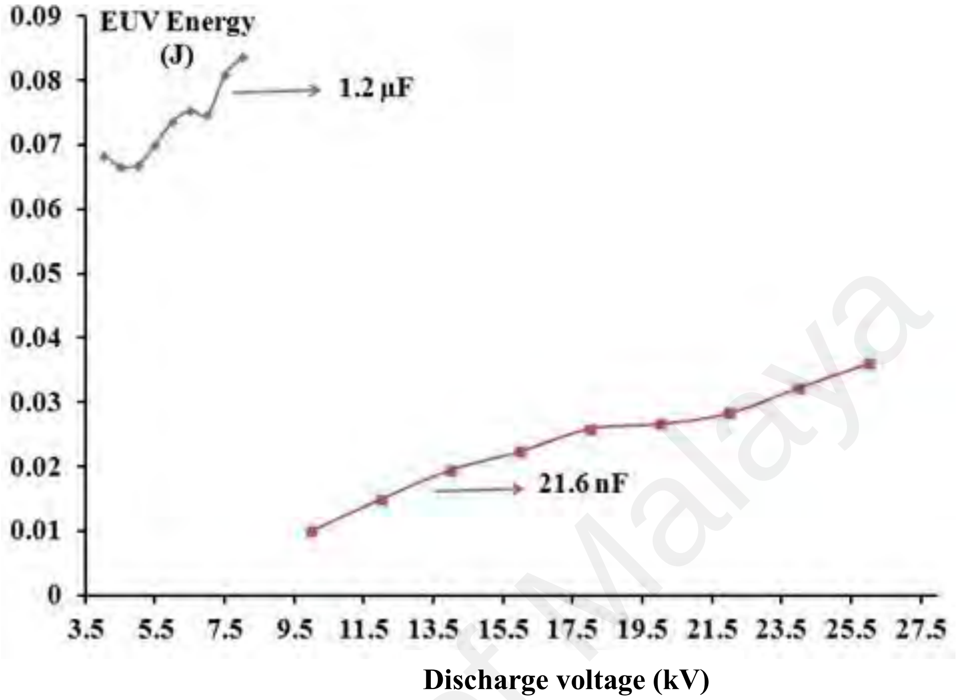

Figure 5.47: EUV energy of the copper capillary plasma that is powered with capacitors with total capacitance of 1.2 µF and 21.6 nF respectively.

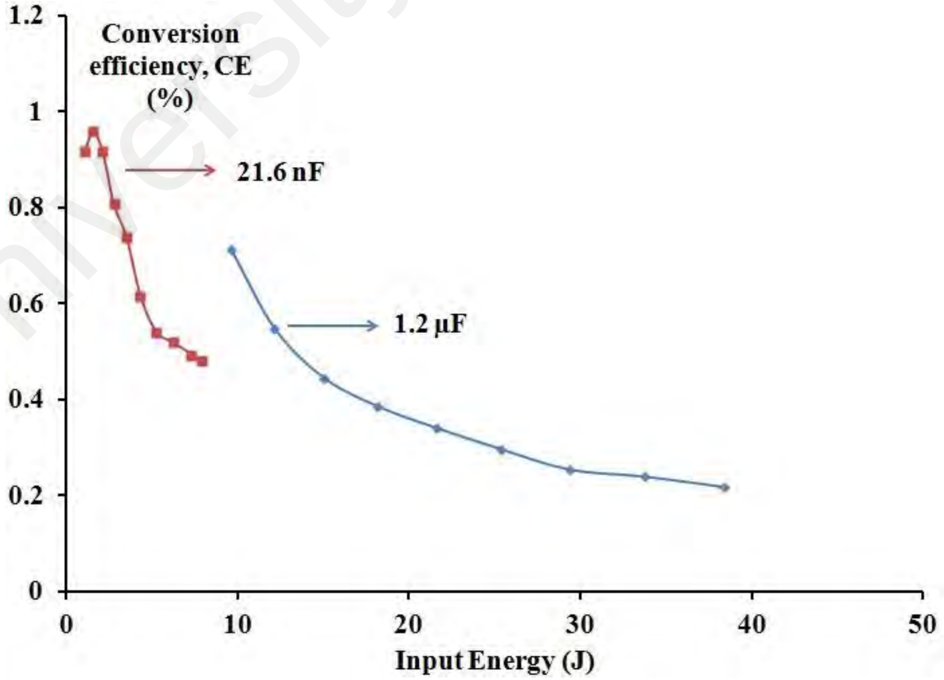

Figure 5.48: Conversion efficiency of EUV energy of the copper capillary plasma that is powered with capacitors with total capacitance of 1.2 µF and 21.6 nF respectively.

It is evidenced that the highest energy achieved by the capillary discharge system that is powered by capacitors of total capacitance of 1.2 μF is higher compared to the highest EUV energy achieved by the capillary discharge system when it is powered by capacitors of total capacitance of 21.6 nF which means with capacitance of 1.2 μF, the energy provided to heat up the plasma increases. However, the overall EUV energy conversion efficiency achieved by the capillary discharge system, when it is powered with capacitors of total capacitance of 21.6 nF is higher compared to it when it is powered with capacitors of total capacitance of 1.2 μF. Thus, there is advantage and disadvantage in increasing the input energy in order to enhance EUV production. Thus, it is concluded that varying the anode material is a better option to enhance the EUV production of the capillary discharge. Besides that, the plasma will get overheated if the input energy is too high and causes the plasma to emit in shorter wavelength which will be out of the desired wavelength region.

CHAPTER 6: CONCLUSIONS AND SUGGESTIONS

A simple technique of generation of metallic plasma capillary discharge has been developed (Chan *et al*., 2014). It makes use of the electron beam that is generated from the THCD to bombard on the tip of the anode and thus, evaporates the material of the anode. Due to pressure gradient, the anode material vapour is injected into the capillary. At the same moment, after a few excursions of electron beam bombarding on the anode (depending on intensity of the electron beam of each excursion) breakdown will occur, the capacitors will discharge through the capillary and heat up the anode material vapour to form plasma.

The bombardment of the electron beam on the anode is indicated by the emission of X-ray at the initiation of the discharge as discussed in section 5.3. The intensity of the X-ray increases as the discharge voltage increases. However, the intensity of the X-ray decreases as the pressure in the capillary discharge chamber (operating pressure) is raised from 10^{-5} to 10^{-3} mbar. This is due the collision between the electron beams with the air particles per unit volume as the electron beam is accelerated along the capillary channel that causes energy to be transferred to the air particle in the capillary channel. Thus, the electron beam becomes weaker as it reaches the anode at higher operating pressure which is 10^{-3} mbar.

The injection of the anode material vapour is evidenced from the time-integrated visible spectrum that is obtained by using the HR 4000 Ocean Optics spectrometer. It is proven that the stainless steel plasma (as stainless steel anode is used) is predominantly by iron (Fe). It is observed that, as the discharge voltage is increased, there are more Fe emission lines. However, as the operating pressure is increased from 10^{-5} to 10^{-3} mbar, the emission lines becomes a lot less prominent as observed in Figure 4.15. This is related to the significant reduction of X-ray emission intensity that shows the less effectiveness of evaporation of the anode at higher pressure (10^{-3} mbar) as portrayed in Figure 5.13.

The anode material (stainless steel predominantly Fe) is heated up in the capillary to form plasma and subsequently emits in the EUV region. A SXUVHS5 Si/Zr 100/200 nm photodiode (IRD) which is sensitive to the range of wavelength of 11-18 nm (with peak sensitivity at 13.5 nm) is used to detect the EUV emission of the capillary plasma. It is obtained that the EUV is emitted once the discharge is initiated and the intensity rises gradually with current signal during the first quarter of the first cycle of the current signal. This shows that the EUV emission is caused by joule heating effect of the plasma. The EUV energy obtained from the plasma decreases with the increased of operating pressure from 10^{-5} to 10^{-3} mbar. Thus, the optimum pressure for EUV production is 10^{-5} mbar. It is obtained that the EUV energy increases with the increased of discharge voltage in the range of 10-26 kV. with discharge voltage in the range of 10-26 kV, however, the EUV energy produced drops at the discharge voltage of 27 kV. Thus the optimum condition for EUV production of a stainless steel Fe predominant plasma formed in a capillary with 1 mm inner diameter and 10 mm long occurs at the operating pressure of 10^{-5} mbar and discharge voltage of 26 kV. The EUV energy achieved is 32.8 mJ.

In order to enhance the EUV emission, the effect of the ambient gas on the EUV emission of the capillary discharge has been investigated. In this case, argon gas is used and it is observed that the stainless steel plasma emits higher EUV energy at lower argon pressure. In another series of experiments, copper anode is used, and thus producing a copper capillary plasma. The best EUV energy produced by the copper plasma is 38 mJ at discharge voltage of 27 kV and pressure of 10^{-5} mbar with CE of 0.48%.

The plasma electron temperature at the operating pressure of 10^{-5} mbar is calculated by simulating the discharge current using the LCR circuit equation. The damping factor, α is obtained through the simulation and the resistance of the plasma is obtained. From the resistance of the plasma, the plasma electron temperature is obtained. The maximum plasma electron temperature of the stainless steel Fe predominant plasma obtained at the discharge voltage of 12 kV is 5.1 eV. The plasma electron temperature rises with discharge voltage as the maximum plasma electron temperature achieved at the discharge voltage of 24 kV and 26 kV are 10.8 eV and 12.6 eV respectively. The copper plasma electron temperature is obtained as well, for the discharge voltage of 24 kV and 26 kV and it is found that the temperatures are 12.0 eV and 13.8 eV respectively.

Based on the plasma electron temperature obtained, the EUV spectra in the range of wavelength of 11-18 nm (aligned with the sensitivity detection range of the photodiode used) is simulated using FLYCHK codes (Chung *et al.*, 2005) for both stainless steel Fe predominant and copper plasma. The EUV emission is contributed by bound-bound emissivity which is originated from the line radiation, bound-free emissivity which is originated from the recombination radiation and finally free-free emissivity which is originated from the bremsstrahlung radiation. It is found that the EUV emission is dominated by bound-bound transition. It is observed that at higher electron temperature the emission at shorter wavelength becomes higher especially at the wavelength of 13.5 nm for both stainless steel Fe predominant and copper plasma. This shows that as the input energy is increased gradually (to make sure the plasma is not overheated) to heat up the plasma, the plasma will achieve suitable temperature for EUV emission at the desired wavelength. It is evidenced that the Copper (Cu) plasma emits with higher intensity compared to iron (Fe) plasma at 13.5 nm.

It is obtained that the best EUV energy produced by the copper plasma (38 mJ) is higher than the stainless steel predominant plasma (32.8 mJ). Thus, in order to further enhance the EUV emission of our metallic capillary discharge with copper as anode, capacitors of higher capacitance with total capacitance of 1.2 μF is purchased to power the capillary system in order to provide higher input energy to the system for EUV production. Thus, the capillary system is now powered by capacitors of higher capacitance and is able to supply a maximum input energy of 38.4 J to the system. The highest EUV energy achieved by this higher-powered capillary system is 83.6 mJ.

However, the conversion efficiency of our capillary system that is now powered with capacitors with total capacitance of 1.2 μF is lower than it was previously powered with capacitors with total capacitance of 21.6 nF. The maximum conversion efficiency achieved by this new system is only 0.71% compared to 0.96% of the previous system. Thus, it is suggested that the EUV production should be enhanced by varying the anode material such as stannum which does not cause prominent effect the conversion efficiency as the input energy is maintained.

Time-resolved EUV spectroscopy is suggested as a future work in order to have better understanding on the EUV emission of the capillary plasma. The EUV spectrum that will be obtained with this diagnostic technique is able to provide information on the ionic species and different energy states of the plasma emission. Besides that, the EUV spectrum will also enable a better estimation of the plasma electron density.

REFERENCES

Andreić, Ž., Ellwi, S., Pleslić, S. and Kunze, H.-J. (2005). Performance of 13.5 nm PVC Capillary Discharge EUV Source. *Physics Letter A*, *335*: 430 – 434.

Ashkenazy, J., Kipper. R., and Caner, M. (1991). Spectroscopic measurements of electron density of capillary plasma based on Stark broadening of hydrogen lines. *Physical Review A*, *43*: 5568-5574.

Andreić, Ž., Ellwi, S., Pleslić, S. and Kunze, H.-J. (2003). In-band EUV radiation of ablative capillary discharge. *Vacuum Surface Engineering, surface instrumentation and vacuum Technolog, 71*: 229-232.

Avaria. G., Gauzman, F., Ruiz, M., Favre, M. Wyndham, E. Bhuyan, H. and Chuaqui, H. (2009). Hollow Cathode Effect in the Pre-breakdown Phase of a Pulsed Capillary Discharge. *Plasma Sources Science and Technology, 18*: 1–6.

Banine, V. and Moors, R. (2004). Plasma sources for EUV lithography exposure tools. *J. Phys. D: Applied Physics, 37*: 3207-3212

Borisov, V.M., Eltsov, A.V., Ivanov, A.S., Kiryukhin, Y.B., Khristoforov, O.B., Mishchenko, V.A., Prokofiev, A.V., Vinokhodovand, A.Y. and Vodchits, V.A. (2004) EUV Source Using Xe and Sn Discharge Plasma. *Journal Physics D: Applied Physics, 37*: 3254 – 3265.

Borisov, V.M., Borisova, G. N., Vinokhodov, A.Y., Zakharov, S.V., Ivanov, A.S. Kiryukhin, Y.B., Mishchenko, V.A., Prokofiev, A.V. and Khristoforov, O.B. (2010) High-power EUV (13.5 nm) light source. *Quantum Electronics*, *40* (8): 720-726.

Corallo, D. M., Creek, D. M. and Murray, G. M. (1980). The X-ray calibration of Silicon PIN diodes between 1.5 and 17.4 keV. *J. Phys. E: Sci Instrum, 13*: 623-626.

Chan, L.S., Tan, D., Saboohi, S., Yap, S. L. and Wong, C. S. (2014). Operation of an electron beam initiated metallic plasma capillary discharge. *Vacuum, 103*: 38-42.

Chan, L.S., Wong, C. S., Yap, S. L., Singh J. and Ahmad, Z. (2009). Time-resolved Imaging of Transient Plasma, *AIP Conference Proceedings*, *1150*: 456-459

Chung, H.-K., Chen, M. H., Morgan, W. L., Ralchenko, Y. and Lee, R. W. (2005). FLYCHK: Generalized population kinetics and spectral model for rapid spectroscopic analysis for all elements. *High Energy Density physics, 1*: 3-12

Choi, P., Chuaqui, H., Favre, M. and Colas, V. (1995). Breakdown Formation in a Transient Hollow Cathode Discharge - A statistical study. *IEEE Transactions on Plasma Science*, *23* (3): 221-228.

Dwyer, Operating Manual for GFC Mass Flow Controllers (2005).

Dussart, R., Hong, D., Götze, S., Rosenfeld, W.E.S, Pons, J., Viladrosa, R., Cachoncinlle, C., Fluerier, C., and Pouvesle, J.-M. (2000). Time-resolved Spatial Distribution of an Ablative Capillary Discharge Obtained with a Pinhole Camera. *J.Phys. D: Appl. Phys*, *33*: 1837-1842

Favre, M., Choi, P., Chuaqui, H., Kaufmann, Y., Moreno, J., Wyndham, E. and Zambra, M. (1995). Hollow cathode effects in Charge development process in transient hollow cathode discharges. *IEEE Transaction on Plasma Science, 23* (3): 212-220

Favre, M., Wyndham, E., Leňero, A. M., Suzuki, F., Valenzuela, J., Avaria, G., Ruiz, M., Bhuyan, H., Chuaqui, H. and Choi, P. (2008). Experimental observations in compact capillary discharges. *Plasma Sources Science and technology, 17* (024011): 1-7.

Girard, F., Lunney, J. G., Larour, J., and Dussart, R., (2002). “Interpretation of capillary Discharge EUV Pinhole Images Using a Ray-tracing Code,”Journal of Physics D: Applied Physics, 35, 1164-1170.

Gonzalez, J. J., Frati, M., Rocca, J. J., Shlyaptsev, V. N. and Osterheld, A. L. (2002). High-power-density capillary discharge plasma columns for shorter wavelength discharge-pumped soft-x-ray lasers. *Physical Review E, 65* (026404): 1-9.

Götze, S., Ellwi, S., Andreić, Ž., Dussart, R., Viladrosa J. Pons, R., Pouvesle,. J.-M. Fluerier, C., and Kunze, H.-J. (2002). Time-resolved diagnostics of plasmas in polyacetal ablative capillary discharges. *Physics Letters A, 299*: 571-576.

Jonkers, J. (2005). High Power Extreme Ultra-Violet (EUV) Light Sources for Future Lithography. *XXVII th ICPIG, Eindhoven, the Netherlands, 18-22 July*.

Janulewicz, K. A., Bortolotto, F., Lucianetti, A., Sandner, W., Nickles, P. V., Rocca, J. J., Bobrova, N. and Sasorov, P. V. (2003). Fast capillary discharge plasmas a preformed medium for longitudinally pumped collisional x-ray lasers. *Journal of Optics Soc. Am. B, 20* (1): 215-220.

Klosner, M. A. and Silfvast, W. T. (1998). Intense Xenon Capillary Discharge Extreme-ultraviolet Source in the 10-16 nm wavelength region. *Optics Letter, 23*: 1609-1611

Klosner, M. A. and Silfvast, W. T. (2000). High-temperature lithium metal-vapour capillary discharge Extreme-ultraviolet Source at 13.5 nm. *Applied Optics, 39* (21): 3678-3682.

Krisch, I., Choi, P., Larour, J., Rous, J., Dumitrescu, C., Chuvatin, A., Zakharov, S., Leblanc, C. and Favre, M. (2000). Characteristics of Plasma

Formation in a Hollow Cathode Triggered Fast Capillary Discharge. *IEEE* 30/1-30/5.

Krüken, T., Bergmann, K., Juschkin, L., and Lebert, R. (2004). "Fundamentals and Limits for the EUV Emission of Pinch Plasma Sources for EUV Lithography, Journal of Physics D: Applied Physics, 37, 3213-3224.

Klosner, M. A., Bender, H. A., and Silfvast, W. T. (1997). Intense plasma discharge source at 13.5 nm for extreme-ultraviolet lithography. *Optics Letters, 22* (1): 34-36.

Klosner, M. A. and Silfvast, W. T. (2001). Xenon Capillary Discharge Extreme-ultraviolet Source Emitting over a Large Angular Range. *Applied Optics, 40* (27): 4849-4851.

Marconi, M. C., Rocca, J. J., Schimerge, J. F., Villagran, M. and Lehmann, F. J. (1990). Effect of a strong axial magnetic field in the plasma recombination and extreme ultraviolet emission from a highly-ionized capillary discharge. *IEEE Journal of Quantum Electronics, 36* (10): 1809-1814

Matthews, D. L., Hagelstein, P. L., Rosen, M. D., Eckart, M. J., Ceglio, N. M., Hazi, A. U., Medeeki, H., MacGowan, B. J., Trebes, J. E., Whitten, B. L., Campbell, E. M., Hatcher, C. W., Hawryluk, A. M., Kauffman, R. L., Pleasance, L. D., Rambach, G., Scofield, J. H., Stone, G., and Weaver, T. A. (1985). Demonstration of a Soft X-Ray Amplifier. *Physical Review Letters, 54* (2): 110-113.

Moreno, C. H., Marconi, M. C., Shlyaptsev, V. N., Benware, B. R., Macchietto, C. D., Chilla, J. L. A., and Rocca, J. J. (1998). Two-dimensional Near-field and Far-field Imaging of a Ne-like Ar Capillary Discharge table-top Soft X-Ray Laser. *Physical Review A*, *58* (2): 1509-1514.

Marconi, M. C. and Rocca, J. J. (1989). Time-resolved extreme ultraviolet emission from a highly ionized lithium capillary discharge. *Applied Physics Letters, 54* (22): 2180-2182.

Marconi, M. C., Moreno, M. C., Rocca, J. J., Shlyaptsev, V. N., and Osterheld, A. L. (2000). Dense of a Microcapillary Discharge Plasma using a Soft X-Ray Laser Backlighter. *Physical Review E, 62*: 7209-7218.

Mohanty, S.R., Robert, E., Dussart, R., Validrosa, R., Pouvesle, J.-M., Fluerier, C. and Cachoncinlle, C. (2003). A novel fast capillary discharge system emitting intense EUV radiation. *Microelectronic Engineering, 65*, (1-2): 47-59.

Moreno, C. H., Marconi, M. C., Shlyaptsev, V. N., and Rocca, J. J., "Shadowgrams of a Dense Micro-Capillary Plasma Obtained with a Table-Top Soft X-ray Laser," IEEE transactions on Plasma Science, 27, 6-7, (1999).

National Institute of Standard and Technology, 2013 (physics.nist.gov/PhysRefData).

Nevrkla, M. (2009). Capillary Discharge XUV Radiation Source. *Acta polytechnic*, *49*, (2-3): 53-57.

Niimi, G., Hayashi, Y., Nakajima, M., Watanabe, M., Okino, A., Horloka, K., and Hotta, E. (2001). Observation of a multi-pulse soft X-ray lasing in a fast capillary discharge. *J. Phys. D: Appl Phys*, *34*: 2123-2126.

Oh, S. Y., Uhm, H. S., Kang, H., Lee, I. W. and Suk, H. (2010). Temporal evolution of electron density and temperature in capillary discharge plasmas. *Journal of Applied Physics, 107* (103309): 1-4.

Rahman, A., Hammarsten, E. C., Sakadzic, S., Rocca, J. J. and Wyart, J.-F. (2003). Identification of n = 4, ▲n = 0 Transitions in the Spectra of Nickel-like Cadmium Ions from a Capillary Discharge Plasma Column. *Physica Scripta, 67*: 414-419.

Rahman, A., Rocca, J. J., and Wyart, J.-F. Classification of the Nickel-Like Silver Spectrum (AgXX) from a Fast Capillary Discharge Plasma. (2004) *Physica Scripta 70*: 21-25.

Rocca, J. J., Cortázar, O. D., Szapiro, B., Floyd, K., and Tomasel, F.G., (1993). Fast-discharge Excitation of Hot Capillary Plasmas for Soft X-Ray Amplifiers. *Physical Review E, 47*: 1299-1304.

Rocca, J. J., Cortázar, O. D., Tomasel, F.G. and Szapiro, B. T. (1993). Efficient generation of highly ionized calcium and titanium plasma columns for collisionally excited soft-x-ray lasers in a fast capillary discharge. *Physical Review E, 48* (4): 2378-2381

Rocca, J. J., Shlyaptsev, V., Tomasel, F. G., Cortàzar, O. D., Hartshorn, D. and Chilla, J. L. A. (1994). Demonstration of a discharge pumped table-top soft X-ray laser. *Physical Review letters, 76* (16): 2192-2195

Rocca, J. J., Clark, D. P., Chilla, J. L. A. and Shlyaptsev, V.N. (1996). Energy extraction and achievement of the saturation limit in a discharge-pumped table-top soft X-ray amplifier. *Physical Review Letters, 77*(8): 1476-1479.

Song, I., Iwata, K., Homma, Y., Mohanty, S.R., Watanabe, M., Kawamura, T., Okino, A., Yasuoka, K., Horioka, K., and Hotta, E. (2006). A Comparative Study on the Performance of a Xenon Capillary Z-pinch EUV Lithography Light Source Using a Pinhole Camera. *Plasma Sources Science Technology, 15*: 322-327.

Suckewer, S., Skinner, C. H., Milchberg, H., Keane, C., and Vorhees, D. (1985). Amplification of Stimulated Soft X-ray Emission in a Confined Plasma Column. *Physical Review Letters, 55* (17): 1753-1756.

Shuker, M., Ben-kish, A., Fisher, A. and Ron, A. (2006) Titanium plasma source for capillary discharge extreme ultraviolet lasers. *Applied Physics Letters*, *88* (061501): 1-3

Spence, D.J. and Hooker, S.M. (2000). Investigation of a Hydrogen Plasma Waveguide. *Physical Review E*, *63* (015401): 1-4.

Spitzer. L., (1956). Physics of Fully Ionized Gases. *Interscience Publishers, Inc., New York*, (3).

Segers, M., Bougeard, M., Caprin, E., Ceccotti, T., Mormand, D., Schmidt, M. and Sublemontier, O. (2002). Development of a laser-produced plasma source at 13.5 nm for the french extreme ultraviolet lithography test bench. *Microelectronic Engineering, 61-62*:139-144.

Saboohi, S., Yap, S. L., Chan, L. S. and Wong, C. S. (2012). Effects of inter-electrode gap and discharge voltage on EUV emission from stainless steel vacuum spark plasma. *Sains Malaysiana, 41* (7): 879-884.

Tan, C. A. and Kwek, K. H. (2007). Influence of Current Prepulse on Capillary discharge Extreme-ultraviolet Laser. *Physical Review A*, *75*, (043808): 1-5.

Tanaka, H., Akinaga, K., Takahashi, A., and Okada, T. (2004). Development of a target for laser-produced plasma EUV Light source using Sn nano-particles. *Applied Physics A*, *79*: 1493-1495.

Tomasel, F.G., Rocca, J.J., and Shlyaptsev, V.N. (1996). Dynamics of the Plasma Column of a Capillary Discharge Soft X-Ray Laser. *IEEE Transactions on Plasma Science, 24*(1): 49-50.

Tomasel, F. G., Rocca, J. J., Cortȧzar, O. D., Szapiro, B. T. and Lee, R. W. (1993). Plasma-density evolution in compact polyacetal capillary dischrages. *Physical Review E, 47* (5): 3590-3597

Valenzuela, J. C., Wyndham, E. S. and Favre, M. (2015). Time-resolved study of the extreme-ultraviolet emission and plasma dynamics of a sub-joule, fast capillary discharge. *Physics of Plasma, 22* (083501): 1-9

Valdivia. M. P., Wyndham, E. S. and Favre, M. (2015). Hollow cathode electron beam formation and effects on X-ray emission in Capillary Discharges. *IEEE Transaction on Plasma Science, 43* (8): 2553-2557

Valenzuela, J. C., Wyndham, E. S., Chuaqui, H., Cortes, D. S., Favre, M., and Bhuyan, H. (2012). Implementation of moirė-schlieren deflectometry on a small scale fast capillary plasma discharge. *Journal of Applied Physics*, 111: (103301-1 - 103301-7)

Wu, B. and Kumar., A. (2014) Extreme ultraviolet and three dimensional integrated circuit- A review. *Applied Physics Review, 1* (011104): 1-15

Wong, C.S., Ong, C.X., Lee, S. and Choi, P. (1992). Observation of enhanced pre-breakdown electron beams in a vacuum spark with a hollow-cathode configuration. *IEEE Transaction on Plasma Science*, *20* (40): 405-409.

Wong, C.S., Ong, C.X., Moo, S.P. and Choi, P. (1995). Characteristics Of A Vacuum Spark Triggered By The Transient Hollow Cathode Discharge Electron Beam. *IEEE Transaction on Plasma Science,23* (3): 265-26

Villagran, M. and Rocca, J. J. (1990). Temporal evolution of plasma from a highly ionized helium capillary discharge. *IEEE Transactions on Plasma Science, 18* (5): 784-788.

Wyndham, E., Aliaga-Rossel. R., Chuaqui, H., Favre, M., Mitchell, I. H. and Choi, P. (2002). X-ray and dynamics of an intermediate size capillary discharge. *IEEE Transaction on Plasma Science, 30* (1): 401-407.

Wyndham, E., Favre, M. and Aliaga-Rossel. R. (2006). Influence of metallic plasmas in transient capillary discharges at high current. *Plasma Sources Sci. Technol, 15*: 538-545.

Wagenaars, E., Mader, A., Bergmann, K., Jonkers, J. and Neff, W. (2008). Extreme ultraviolet plasma source for future lithography. *IEEE Transactions on Plasma Science, 36* (4) : 1280-1281.

Wong, C. S. (1982). X-ray detection systems for diagnostics of pulsed plasma sources. *Bulletin Physics Malaysia, 3*: 129-135

Yap, L. M., Wong, C. S. and Ahmad, Z. (2006). Imaging and measurement of 13.5 nm EUV Radiation from a Pulsed Capillary Discharge. *Jurnal Fizik Malaysia, 27* (2): 63-66.

Zhang, C.H. Katsuki, S., Horta, H., Imamura, H., Kondo, Y., Namihira, T., and Akiyama, H. (2005). Xenon Discharge Produced Plasma Radiation Source for EUV Lithography. *Industry Applications Conference 2005, Fourtieth IAS Annual Meeting Conference Record of the 2005:* 2320-2323.

LIST OF PUBLICATIONS AND PAPERS PRESENTED

1. L.S. Chan, D. Tan, S. Saboohi, S.L. Yap, C.S. Wong (2014). Operation of an electron beam initiated metallic plasma capillary discharge. *Vacuum, 103*: 38-42.
2. L.S. Chan, D. Tan, S. Saboohi, S.L. Yap, C.S. Wong (2014). Enhancement of the EUV Emission of a Metallic Capillary Discharge Operated with Argon Ambient Gas. *AIP Conf. Proc. 1588*:167-170
3. L. S. Chan, S. L. Yap, and C. S. Wong (2011). EUV Emission of a Pulsed Capillary Discharge. *AIP Conf. Proc. 1328*: 158-160
4. L. S. Chan, C. S. Wong, S. L. Yap, J. Singh, and Z. Ahmad "Time-Resolved Imaging Of Transient Plasma" AIP Conf. Proc. 1150, Pg: 456 (2009)
5. S. Saboohi, S.L. Yap, L.S. Chan, C.S. Wong (2012). Investigation of the Temporal Evolution of X-Ray Emission From a Copper Vacuum Spark Plasma. *IEEE Transactions on Plasma Science, 40*(12): 3390-9994
6. S. Saboohi, S.L. Yap, L.S. Chan, C.S. Wong (2012). Effects of Inter-electrode Gap and Discharge Voltage on EUV Emission from Stainless Steel Vacuum Spark Plasma. *Sains Malaysiana 41*(7): 879–884
7. S. Saboohi, S.L. Yap, M. Ghomeishi, L.S. Chan, C.S. Wong (2011). Effect of Interelectrode Gap on the Emission of EUV and X-Ray Radiation from Vacuum Spark Discharges. *AIP Conf. Proc. 1328*:148-151
8. L. S. Chan, M. Ghomeishi, S. L. Yap, and C. S. Wong (2010). X-ray and EUV Emission Studies of Copper Vacuum Spark Plasma. *AIP Conf. Proc. 1250*: 452-455